Scholar Commons
USF University of South Florida

University of South Florida
Scholar Commons

Graduate Theses and Dissertations | Graduate School

10-27-2010

Carbon Nanotube Enhanced MALDI MS: Increasing Sensitivity Through Sample Concentration

Joshua Schumacher
University of South Florida

Follow this and additional works at: http://scholarcommons.usf.edu/etd

 Part of the American Studies Commons

Scholar Commons Citation
Schumacher, Joshua, "Carbon Nanotube Enhanced MALDI MS: Increasing Sensitivity Through Sample Concentration" (2010). *Graduate Theses and Dissertations.*
http://scholarcommons.usf.edu/etd/3595

This Dissertation is brought to you for free and open access by the Graduate School at Scholar Commons. It has been accepted for inclusion in Graduate Theses and Dissertations by an authorized administrator of Scholar Commons. For more information, please contact scholarcommons@usf.edu.

www.manaraa.com

Carbon Nanotube Enhanced MALDI MS:

Increasing Sensitivity Through Sample Concentration

by

Joshua Schumacher

A dissertation submitted in partial fulfillment
of the requirements for the degree of
Doctor of Philosophy
Department of Electrical Engineering
College of Engineering
University of South Florida

Major Professor: Rudy Schlaf, Ph.D.
John Koomen, Ph.D.
Mark McLaughlin, Ph.D.
Salvatore Morgera, Ph.D.
Jing Wang, Ph.D.
Yusuf Emirov, Ph.D.

Date of Approval:
October 27, 2010

Keywords: Mass Spectrometry, Carbon Nanotube, Peptide Detection

© Copyright 2010, Joshua Schumacher

www.manaraa.com

Dedication

This dissertation is dedicated to my family and friends who were there for me when I needed them the most.

www.manaraa.com

Acknowledgments

This work was supported by Dr. Melvyn Tockman and Dr. Thomas Sellers from the H. Lee Moffitt Cancer Center & Research Institute. Additional support from the IGERT program at USF through the National Science Foundation Grant DGE-0221681.

The following persons were instrumental in this work through assistance or advice and deserve to be acknowledged as a token of my gratitude:

My dissertation committee, especially Dr. Rudy Schlaf and Dr. John Koomen

Dr. Yusuf Emirov and the Nanomaterials and Nanomanufacturing Research Center staff

Dr. Eric Thomas and the Proteomics Core Facility staff at the Moffitt Center

Dr. Ted Gauthier and the Mass Spectrometry and Peptide Synthesis Core Facility at USF

Dr. Martin Beerbom and the Surface Science Laboratory at USF

Mr. Mark Lloyd and the Analytic Microscopy Core Facility staff at the Moffitt Center

Mr. Bernard Batson, IGERT Program Coordinator at USF

www.manaraa.com

Table of Contents

www.manaraa.com

www.manaraa.com

List of Tables

www.manaraa.com

List of Figures

www.manaraa.com

www.manaraa.com

www.manaraa.com

www.manaraa.com

www.manaraa.com

www.manaraa.com

www.manaraa.com

www.manaraa.com

www.manaraa.com

Abstract

Matrix-assisted laser desorption/ionization (MALDI) is a technique used in mass spectrometry for the ionization of biomolecules. A matrix solution is mixed with the analyte molecules to be investigated, and then spotted onto a specialized MALDI plate. The solvents evaporate leaving only the re-crystallized matrix with analyte dispersed throughout the crystals. Sample ionization is accomplished with a laser in the MALDI instrument. The spot diameter of the target is usually several orders of magnitude larger than the diameter of the laser, making it necessary to perform multiple laser investigations to accurately evaluate the analyte in the target spot.

Experiments were performed to utilize patterned areas of carbon nanotubes to provide sites for preferential crystallization of the liquid matrix/analyte solution, which led to lateral concentration for non-aqueous based matrices and produced a final dried matrix/analyte spot that was approximately the diameter of the laser spot at the point of investigation. This work shows the results of using aligned carbon nanotubes as the substrate for the matrix/analyte deposition and demonstrates an increase in signal to noise ratio and an improved detection capability of low analyte concentrations compared to the standard MALDI preparation technique.

www.manaraa.com

Chapter 1: Introduction

Proteomics is the study of the structure and functions of proteins and peptides from a cell or tissue. Proteins and peptides are made up of combinations of amino acid chains. The sequence of the amino acids can influence how the protein functions; therefore identification of the structure is important to determine functional roles in a cell or the human body.

Proteomics has important applications in cancer research such as tumor analysis [1, 2], biomarker discovery and identification [3], chemotherapy and drug resistance [4], and general research for some of the most serious types of cancers including leukemia [5], ovarian [6], cervical [7], and prostate [8].

To identify proteins and peptides of interest, there are multiple tools and techniques used in proteomics including gel electrophoresis, chromatography, mass spectrometry, and antibody-tagged fluorescence microscopy. Mass spectrometry (MS) is a sensitive tool that can be used to measure the masses of particles and chemical compounds. Using this tool to identify biomolecules (proteins, peptides, DNA) requires specialized techniques to enable desorption and ionization of the molecules while keeping them intact. Matrix-assisted laser desorption/ionization mass spectrometry (MALDI-MS) is a popular and powerful technique used in proteomics for identifying biomolecules and determining the distribution of those present in a sample.

www.manaraa.com

In the MALDI process, a matrix is used to protect and assist in ionization by donating charge to the analyte biomolecules when excited by the laser. The matrix consists of crystallized molecules specific to the type of analyte to be investigated. In most sample preparation procedures, the matrix is first dissolved in the appropriate solvent (de-ionized water, various organic solvents, etc.), then mixed with solution containing the analyte molecules. The resultant solution is deposited onto a MALDI plate (a specialized stainless steel plate with a grid of inscribed circles), where the matrix re-crystallizes with the analyte as the solvents evaporate and forms a spot. This is referred to as co-crystallization.

For analysis, the plate is loaded into the MALDI instrument and subjected to a vacuum environment. The energy from the laser is absorbed by the matrix, which transfers charge to the analyte. In the process, plumes of both matrix and analyte molecules are desorbed from the plate surface. The ionized analyte molecules are detected by a time-of-flight (TOF) mass spectrometer and the data is plotted in a graph of intensity vs. mass-to-charge ratio.

Current sample preparation techniques produce a target spot diameter much larger than the diameter of the laser spot. Multiple laser investigations are performed at different locations on the same spot and the data is averaged in order to obtain an analyte signal from the target. However, the dried mixture of matrix and analyte has been shown to be non-homogenous, most likely a result of separation of the two substances during

www.manaraa.com

crystallization. This increases the number of investigations required to get an accurate average of the analyte signal.

It has been shown that the spot size of the dried matrix/analyte mixture can be reduced by use of patterned hydrophobic and hydrophilic surfaces. Since carbon nanotubes have a hydrophobic nature, they were selected for experimentation to influence the crystallization of the liquid matrix/analyte solution. Carbon nanotubes have been used in MALDI sample preparation, however the CNT's were created from coal using an arc discharge process and were distributed across the sample surface in a non-aligned, random fashion.

Experiments were performed to test the effect of deposition on a substrate that was enhanced by the growth of multi-wall carbon nanotubes in patterned areas using a Plasma-Enhanced Chemical Vapor Deposition reactor. Multiple comparisons between the standard MALDI plate and the CNT-enhanced substrate were carried out to analyze performance with respect to signal quality, detection limit, and desorption threshold.

Additionally, data was presented to further the understanding of the crystallization process and document the drying behavior that was observed via optical microscopy. Factors that have an effect on sample morphology, such as matrix concentration in solution, overall deposition volume, and possible molecular interactions, were investigated parametrically through experimentation.

www.manaraa.com

Investigation of analytes at low concentrations was performed to determine the capability of detection for the carbon nanotube-enhanced substrates. The advancement of detecting low levels of peptides in a biological sample could have a direct impact on the early detection of cancer for increased treatment and survivability.

Finally, an experiment to ascertain the effectiveness of the MALDI process at investigating the volume of matrix crystals was performed through a process of interrogating a sample past the point of signal exhaustion, followed by dissolving any remaining crystals, and subsequent re-deposition of material after solvent evaporation. This data was compared to published results regarding laser penetration depth in matrix crystallites.

www.manaraa.com

Chapter 2: Background

2.1 Carbon Nanotubes

2.1.1. Carbon Nanotube Properties

A carbon nanotube is one of the many different occurring forms (or allotropes) of the element carbon. Other familiar allotropes include diamond and graphite. Carbon nanotubes (CNTs) are tubular structures composed entirely of carbon atoms that are joined with 120° bond angles that resemble rolled up sheets of graphene (Figure 1). CNT's can be either a single tube (single-walled) or multiple tubes inside each other (multi-walled), according to the type of growth process. Each wall can be classified as "armchair", "zigzag" or "chiral" depending on the orientation of the carbon bond angles with respect to the diameter of the tube (illustrated in Figure 2). Each type has characteristic properties such as minimum diameter and electron conductivity.

The chiral vector (shown as arrows in Figure 1) is used to describe the CNT shell. It defines the distance between two lattice points in a defined direction and is based on unit vectors a1 and a2 ($C=na1+ma2$). If a carbon nanotube has an a1 component of 0, then it is armchair and will take the form shown in Figure 2(a). If it has an a2 component of 0, then it is zigzag and will take the form shown in Figure 2(b). Any other combinations of a1 and a2 components will form a chiral carbon nanotube (Figure 2c), and the diameter of the CNT will be dependent on the length of the vector.

www.manaraa.com

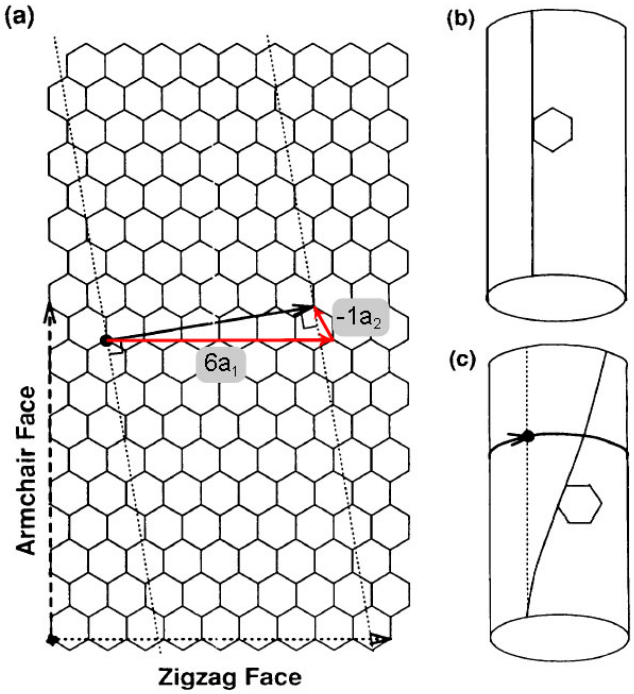

Figure 1. Chiral vector illustrating CNT orientation and determination of structure [9]. Copyright 1992 with permission from the American Physical Society.

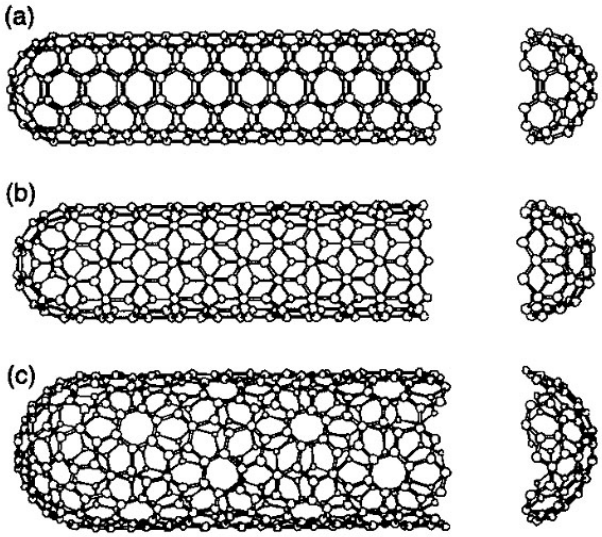

Figure 2. Three types of CNT shells: Armchair (a), Zigzag (b), and Chiral (c) named for the description of the termination at the endcap [10]. Copyright 1995 with permission from Elsevier.

www.manaraa.com

The conductivity of the carbon nanotube is also determined by the chiral vector as illustrated in Figure 3. Depending on the lattice unit cell, CNTs can behave as a metal or semiconductor. CNTs with armchair structure behave as a metal, while zigzag and chiral CNTs can behave as either a metal or semiconductor depending on the vector. In Figure 3, the lattice points that are surrounded by a circle are metallic while those without are semiconducting.

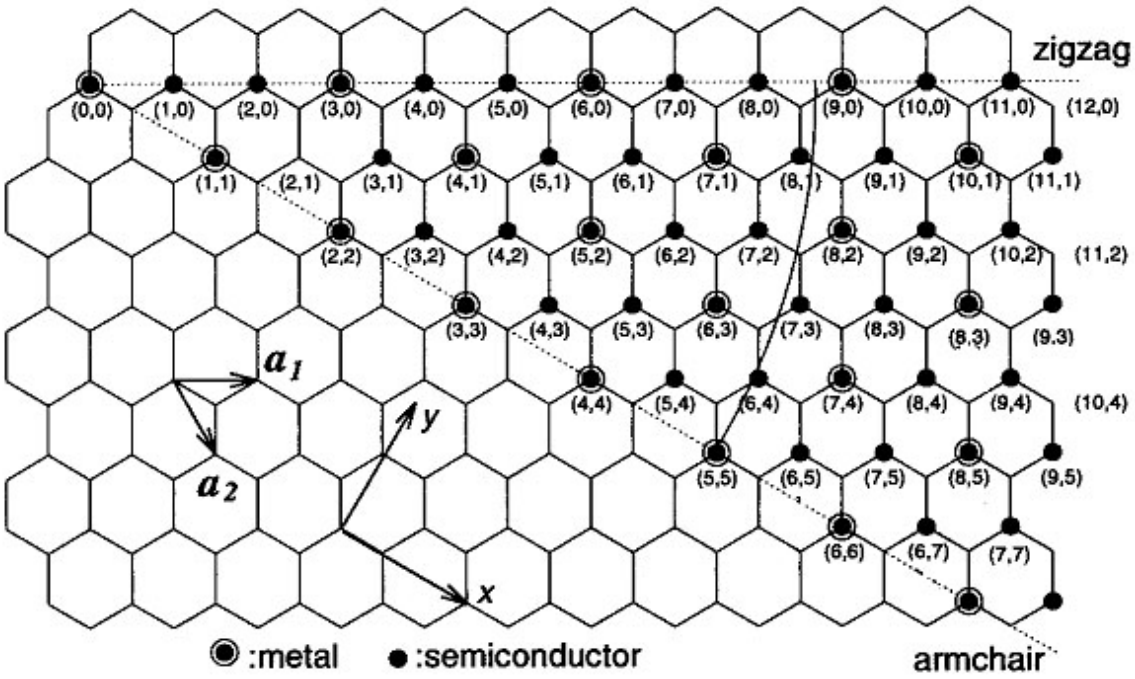

Figure 3. Illustration of conductivity as a function of chiral vector [11]. The vectors that end at a circled point demonstrate metallic conduction characteristics. Copyright 1992 with permission from American Institute of Physics.

It has been theorized that each lattice point in Figure 3 should produce a CNT with unique electronic properties. Charlier et al. [12] calculated the density of states for single walled CNTs with different chiral vectors and plotted a comparison in Figure 4. The

www.manaraa.com

simulations for both the 10,10 (armchair) and 14,5 (chiral) carbon nanotubes displayed metallic properties, but with slight differences. The 16,2 CNT should behave similar to a semiconductor according to the diagram in Figure 3 and the lack of available states at 0eV in the simulation (Figure 4) indicates a band gap and semiconducting properties which coincides with the theory. For carbon nanotubes that consist of multiple walls, each wall can have its own chiral vector and electronic properties. However in practice, multi-walled CNTs usually display metallic properties due to the probability that one shell has a chiral vector consistent with metallic properties, hence dominating conduction when the entire nanotube is measured.

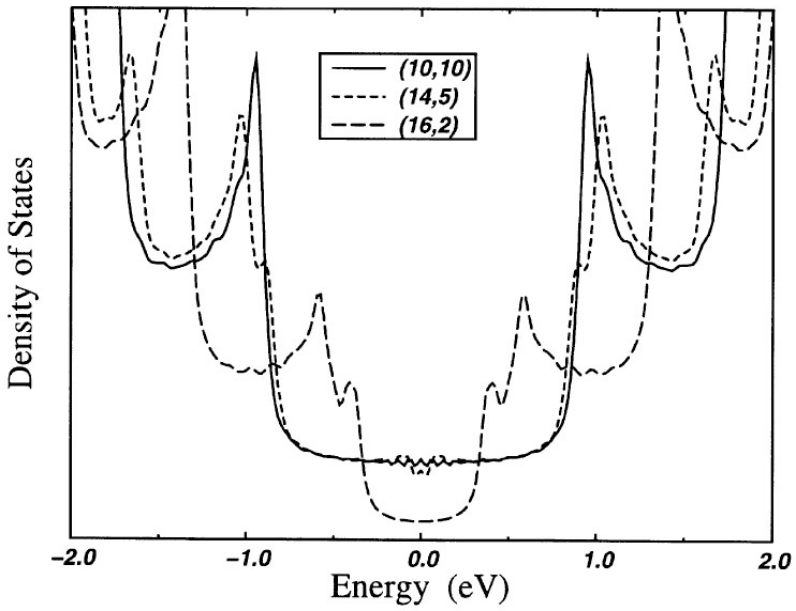

Figure 4. Density of states diagram for CNTs with different chiral vectors [12].

Copyright 1998 with permission from Springer Science + Business Media.

www.manaraa.com

2.1.2. Carbon Nanotube Growth by Plasma Enhanced Chemical Vapor Deposition

Carbon nanotubes can be grown using various techniques, however most growth processes rely on the presence of a catalyst (typically iron, cobalt, or nickel), and are said to be catalyst dependent. The early techniques were carbon arc discharge [13] and laser vaporization [14]. Subsequently, chemical vapor deposition (CVD) was applied as a CNT growth technique [15]. A variation of this technique, plasma-enhanced chemical vapor deposition (PE-CVD) [16-18] was used for the presented research since it allows control over location and the alignment of the grown CNT relative to the substrate surface.

Chemical vapor deposition is a process commonly used in industry to deposit thin films of materials on a substrate through a chemical reaction of precursor gases that are introduced into a controlled environment (such as a vacuum chamber). Typically the substrate is heated to a high temperature (650-1050°C, depending on the process) and the molecules from the precursor gasses decompose on the substrate surface forming the desired deposit. This technique can be used in the semiconductor manufacturing field to produce films of polysilicon, silicon dioxide, silicon nitride, various metals, and carbon nanotubes.

For the PE-CVD process, the precursor gases are exposed to a source of energy, such as radio frequency (RF) or a high direct current (DC) voltage across electrodes, sufficient to ionize the gas molecules causing ignition of a plasma. The process is assisted by the application of heat to the substrate. Usually, the amount of heat required in PE-CVD is

www.manaraa.com

significantly less than in the CVD process, as a result of the energy provided by the plasma. This technique can be used to deposit both conductive and insulating films, as well as grow carbon nanotubes.

A simplified schematic of a PE-CVD reactor for CNT growth is shown in Figure 5. The system consists of a stainless steel chamber, vacuum pump, substrate heater, high-voltage DC power supply with electrode, and a network of mass flow controllers and valves for mixing and administering the precursor gasses into the chamber.

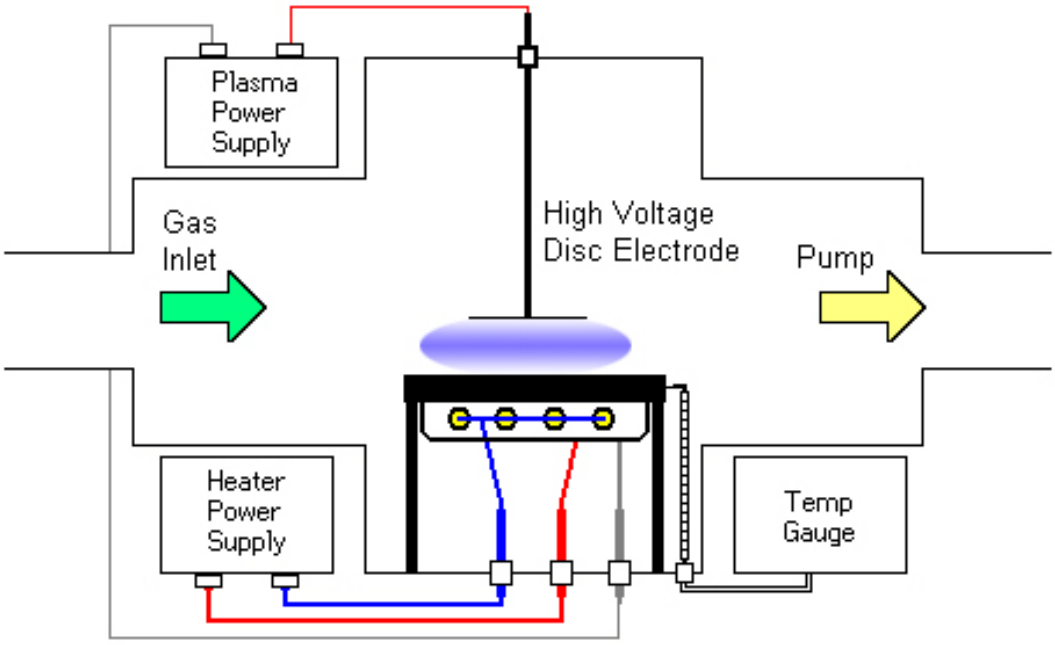

Figure 5. Diagram of PE-CVD reactor showing major components.

The metals iron, nickel and cobalt have displayed characteristics that make them effective catalysts for carbon nanotube growth due to their ability to decompose non-

www.manaraa.com

graphitic carbon compounds [19], form metastable carbides [20], and their display of high diffusion rates for carbon atoms [19, 21].

When the carbon containing precursor gases are introduced to the chamber, the addition of energy in the form of heat or electricity aids the catalyst driven fractionating of the precursor molecules into their components. During this process, the carbon atoms migrate into the catalyst and along a concentration gradient (Figure 6) [22]. When local supersaturation is reached, carbon begins to precipitate around the bisecting diameter [23] and at the surface of the catalyst [19], to form a carbon nanotube.

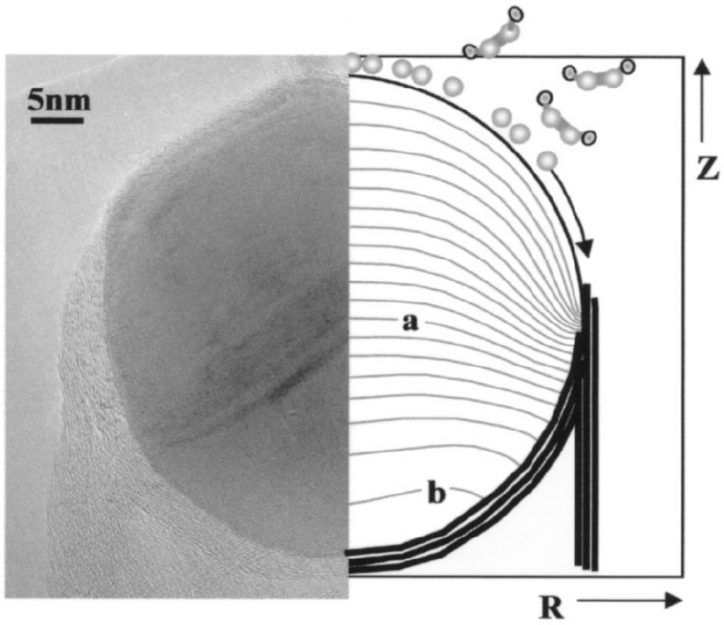

Figure 6. TEM image of CNT tip showing Ni catalyst particle and surrounding carbon atoms on the left and simulation results for carbon distribution gradients in Ni catalyst on the right [22]. Copyright 2004 with permission from American Institute of Physics.

www.manaraa.com

The concentration gradient, tube walls, and internal structure (such as bamboo intersects) is partially determined by the shape and size of the catalyst particle [22]. Substrate temperature [24], deposition thickness [25], and exposure to any etching precursor gasses (NH_3) can have an effect on the size and shape of catalyst particles formed from a deposited catalyst film.

Qin et al. [26] concluded that the amount of carbon that can be contained in a catalyst particle is temperature dependent and highly localized. He theorized that for thermal CVD, the bottom of the catalyst particle is held at a relatively constant temperature as a result of contact with the sample surface. The act of decomposition of the carbon containing precursor gas removes heat from the surface of the catalyst, which becomes locally supersaturated [26]. The result is the precipitation of carbon in the form of a nanotube from the upper surface of the catalyst, which accounts for the apparent bottom-up growth of the nanotube. This is also known as root growth and is illustrated in Figure 7.

www.manaraa.com

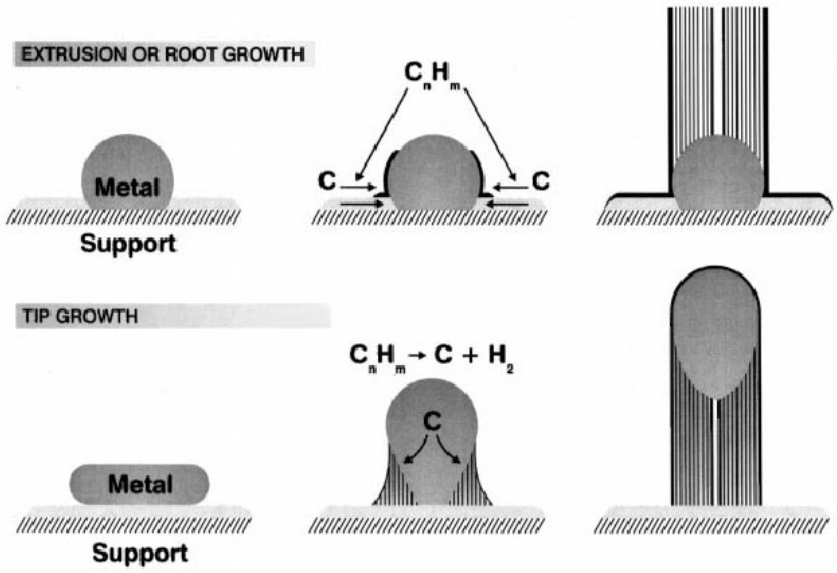

Figure 7. Illustration and comparison of growth mechanism for root growth (top) and tip growth (bottom) [23]. Copyright 1999 with permission from Elsevier.

For plasma enhanced chemical vapor deposition, the substrate temperature required for CNT growth is typically 50 to 100°C less than that for thermal CVD, thought to be a result of the plasma energy contributing to the decomposition process. The carbon atoms enter the top of the catalyst and precipitate out of the bottom, pushing the catalyst particle upwards as the carbon nanotube forms [23] (see Figure 7, bottom), producing a CNT with a catalyst particle at the tip. This is known as tip growth and was demonstrated by Delzeit et al. [27].

After the growth process is completed and the sample is allowed to cool, the carbon remaining in the catalyst particle can form a stable carbide. For a nickel catalyst, Ni_3C is formed at temperatures below 340°C [28] and the evidence of which can be seen in Figure 8. Typical growth temperatures in CVD and PECVD are above the carbide

www.manaraa.com

decomposition temperature [29] so the carbide should not be present or effect the growth process [30].

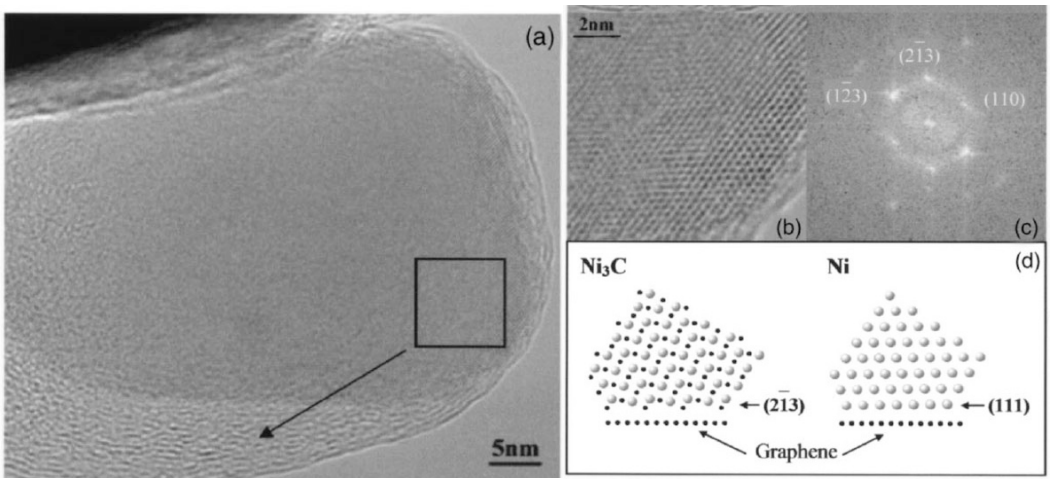

Figure 8. High resolution TEM image of nickel particle at the tip of a CNT grown by PECVD. The diffraction pattern is shown in (c) and corresponds to the structure of Ni_3C rather than pure Ni [22]. Copyright 2004 with permission from American Institute of Physics.

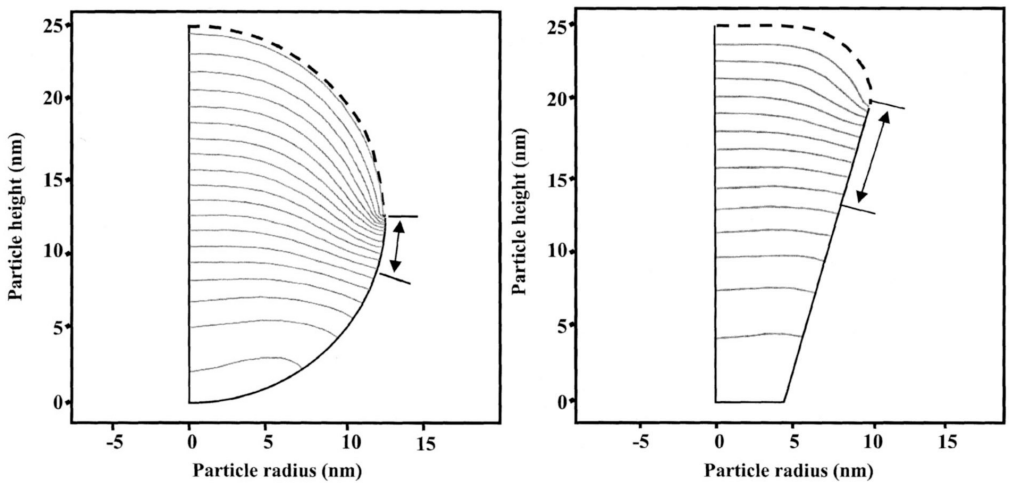

Figure 9. Carbon concentration gradients calculated for round and conical catalyst particles. The area denoted by arrows represents the statistical convergence zone [22]. Copyright 2004 with permission from American Institute of Physics.

www.manaraa.com

The alignment mechanism of carbon nanotubes was originally thought to be caused by the interaction of Van der Waals forces between closely grown nanotubes. Bower et al. [16] demonstrated that CNTs will regrow randomly in the absence of an electric field, after being grown previously aligned. If Van der Waals forces were the primary force responsible for alignment, the nanotubes should have remained aligned after the removal of the electric field.

Merkulov et al. [31] proposed an alignment mechanism for PECVD growth based on electrostatic forces along electric field lines. As illustrated in Figure 10, an electrostatic force (F) acting along the applied electric field induces tensile stress at the carbon precipitation points on the catalyst particle during growth in both the tip and root growth mechanisms. Any deviation or fluctuation during the process could cause misalignment. In that case, the electrostatic force (F) would induce a compressive stress due to the interaction of the CNT and the electric field. The compressive stress would be a restoration force to cause re-alignment in the tip growth, but not for the root growth due to the opposite distribution of the stress.

www.manaraa.com

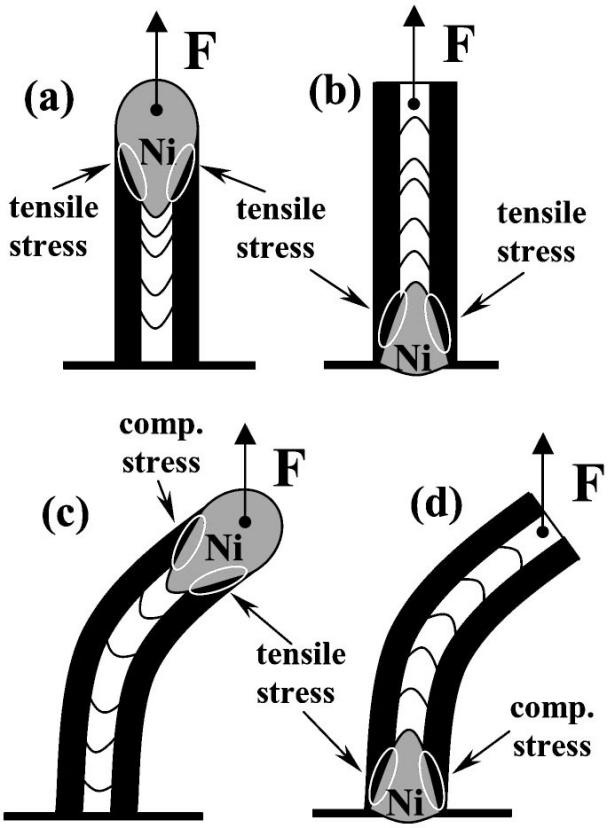

Figure 10. Alignment mechanism for tip growth (a) and root growth (b). Misalignment during growth causes a restoration force in the case of tip growth (c) but not for root growth (d) [31]. Copyright 2001 with permission from American Institute of Physics.

2.2 Thin Film Deposition

Deposition of thin metallic films can be performed through chemical or physical means. Chemical deposition techniques, such as plating, chemical solution and chemical vapor deposition (CVD) [32], involve a process that is dependent on a chemical change at the surface of the sample (the substrate). The material to be deposited (known as a precursor) is introduced into the system in the form of a liquid or gas. The reaction at the

www.manaraa.com

solid interface of the substrate extracts the metallic component of the precursor from solution or gas phase and causes thin film growth on the substrate surface. Energy in the form of heat or electricity can be added to the system to enhance the deposition process. Heat energy is used in the thermal CVD process and electricity is used for electroplating and plasma-enhanced CVD (as described in section 2.1.2).

An advantage of chemical deposition, the deposited film is typically conformal to the sample surface, meaning a nearly uniform film thickness regardless of surface features (Figure 11, left). This is a result of solution interaction with the entire sample surface. Thickness variations in the deposited film are possible due to fluid flow and energy distribution around the substrate.

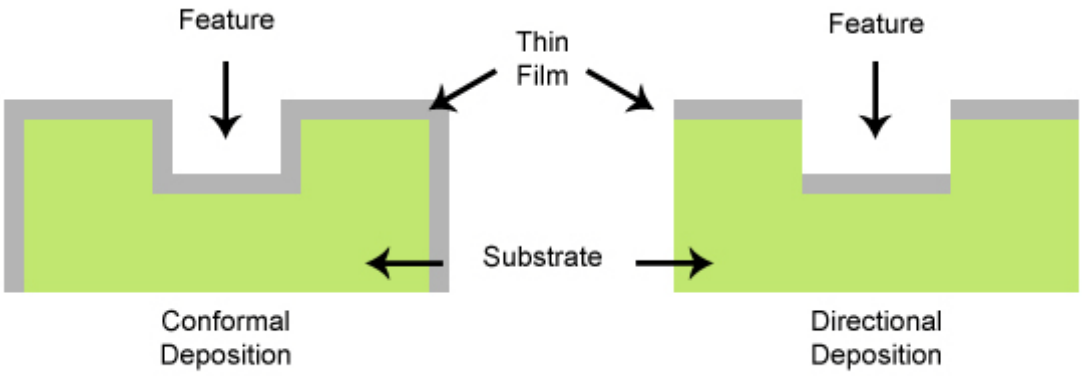

Figure 11. Illustration of differences in sidewall coverage between conformal and directional deposition methods.

Sputtering and evaporation are two techniques used for physical deposition of metallic films. These techniques utilize the vaporization of a metal target either through heating or electricity and are typically performed in a chamber under medium vacuum conditions

www.manaraa.com

(10^{-5} to 10^{-2} Torr). The sputtering process involves ignition of a gas discharge in an inert gas (such as argon) that has been introduced into a vacuum chamber. Plasma is created and the ions impinge on the target with sufficient momentum to remove metal atoms from the target surface [32]. The metal atoms are deposited onto the substrate and create a film. Sputtering can also be used to make films of alloys (Ti-Al, Ni-Fe, etc.) and insulating materials (TiN, SiO_2).

In the evaporation process, a metal target is heated to the point of vaporization either directly by resistive elements (thermal evaporation) or by an electron beam (e-beam deposition). The metal vapor expands radially from the molten source and the atoms are deposited on the substrate in a directional manner as a result of reduced particle collisions [33] in the vacuum chamber. The property of directional deposition can be used with masks to create patterned deposits on the sample surface (Figure 11, right).

The catalyst patterns used in this work for the controlled growth of carbon nanotubes were prepared using electron beam evaporation. In this process, electrons are emitted from a tungsten filament that is heated to incandescence in a vacuum. The electrons are accelerated by a charged anode and focused into a beam. A magnetic field generated by a combination of permanent and electromagnets is used to bend the beam through a 270º arc toward the target material in the crucible. The beam heats the target in a small spot and evaporation occurs (Figure 12). The resulting vapor is deposited on the surface of the substrate and forms a thin film.

www.manaraa.com

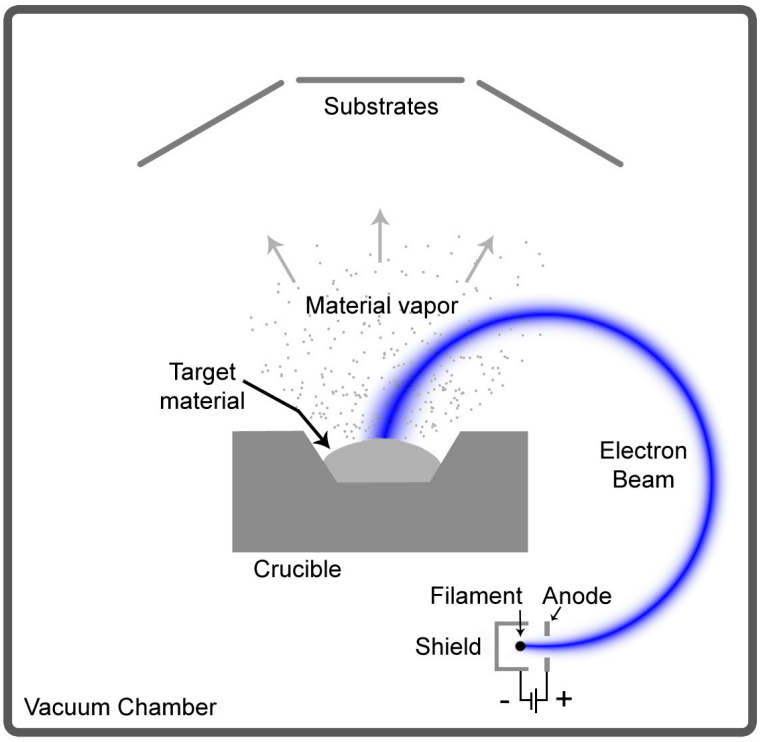

Figure 12. Schematic of electron beam physical vapor deposition process, illustrating e-beam generation, re-direction, and resultant deposition onto the substrate.

A simple design of an electron beam evaporator places an electron emitter above the crucible for direct heating. However, the filament can become coated with the evaporated target material, decreasing electron emission. Incorporation of the 270º deflection design solves this problem and introduces additional capabilities such as beam focusing and beam shifting/scanning through the use of electromagnetic deflection coils.

An advantage of the electron beam deposition process is the wide range of the deposition rate from nanometers to micrometers per minute. The deposition rate is

www.manaraa.com

dependent on the target material temperature, which is controlled by the beam energy. Steady control of the filament emission current produces stable evaporation rates.

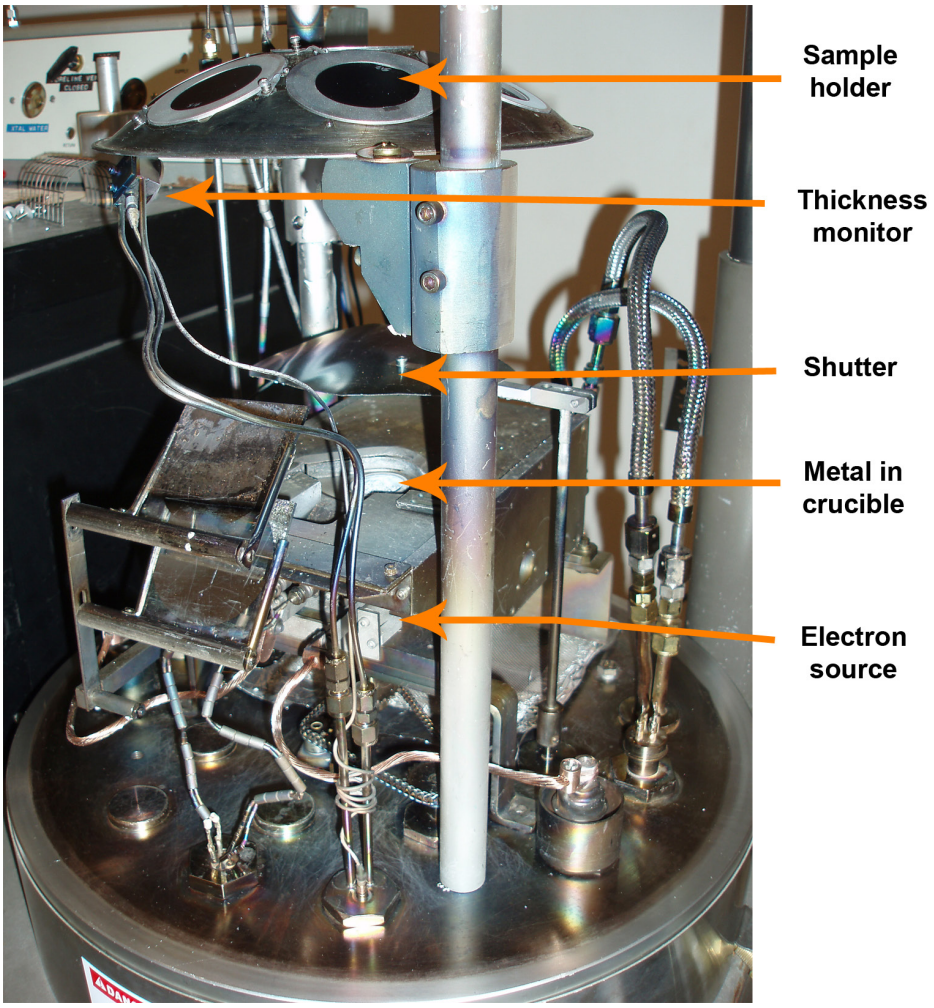

Figure 13. Internal structure of an electron beam evaporator.

The rate of deposition is typically monitored in-situ by a quartz crystal monitor near the substrate position (Figure 13). This type of monitor uses an exposed quartz crystal driven at a resonant frequency to sense the mass of the deposited film. The frequency shift due to the increasing mass during deposition is converted to a film thickness by entering the target material density into the electronic monitoring unit. The change in film

www.manaraa.com

thickness over time defines the deposition rate. The accuracy of the deposition monitor can be determined by evaporation on a test sample and subsequent measurement of the film thickness with a profilometer.

The shutter enables isolation of the substrate from the deposition source by blocking the direct line between them. This allows the user to heat the target material to molten temperatures, stabilize deposition rates, and remove any oxidized material or surface contamination before exposing the substrate to deposition. These actions increase the deposition uniformity both in composition and morphology.

2.3 Matrix Assisted Laser Desorption Ionization

2.3.1 MALDI Measurement Process

Matrix-assisted laser desorption/ionization mass spectrometry (MALDI-MS) is used for quantitative mass spectrometry of macro-molecular materials, such as proteins and peptides. This technique was developed in 1985 by Hillenkamp and Karas [34] when it was discovered that the ionization of the amino acid alanine was enhanced when it was mixed with the amino acid tryptophan, which acted like a matrix absorbing laser energy and ionizing the alanine when exposed to a pulsed 266 nm laser. Further developments by Tanaka [35] allowed the use of a more economical nitrogen laser at 337 nm paired with a cobalt based matrix. The most common matrices used today are based on benzoic or cinnamic acids and absorb light with wavelengths below 350 nm.

www.manaraa.com

Typical sample preparation is accomplished by droplet deposition of the matrix/analyte solution on a sample plate ("MALDI plate"). The process is detailed in section 2.3.2. After the sample-spot dries, the MALDI plate is loaded into the instrument, which consists of a vacuum chamber with a laser beam line, and a time of flight mass spectrometer (Figure 14). It should be noted that atmospheric pressure MALDI is also possible, but has limitations in sensitivity and mass range. A pulsed UV (or IR in some implementations of the technique) laser irradiates the sample spot and the combination of matrix and analyte molecules are desorbed from the surface of the deposit. Ideally, the matrix should desorb from the sample surface without destructively heating the analyte. Ionization is assumed to occur at the sample surface and in the initial stages of the resulting plume of molecules.

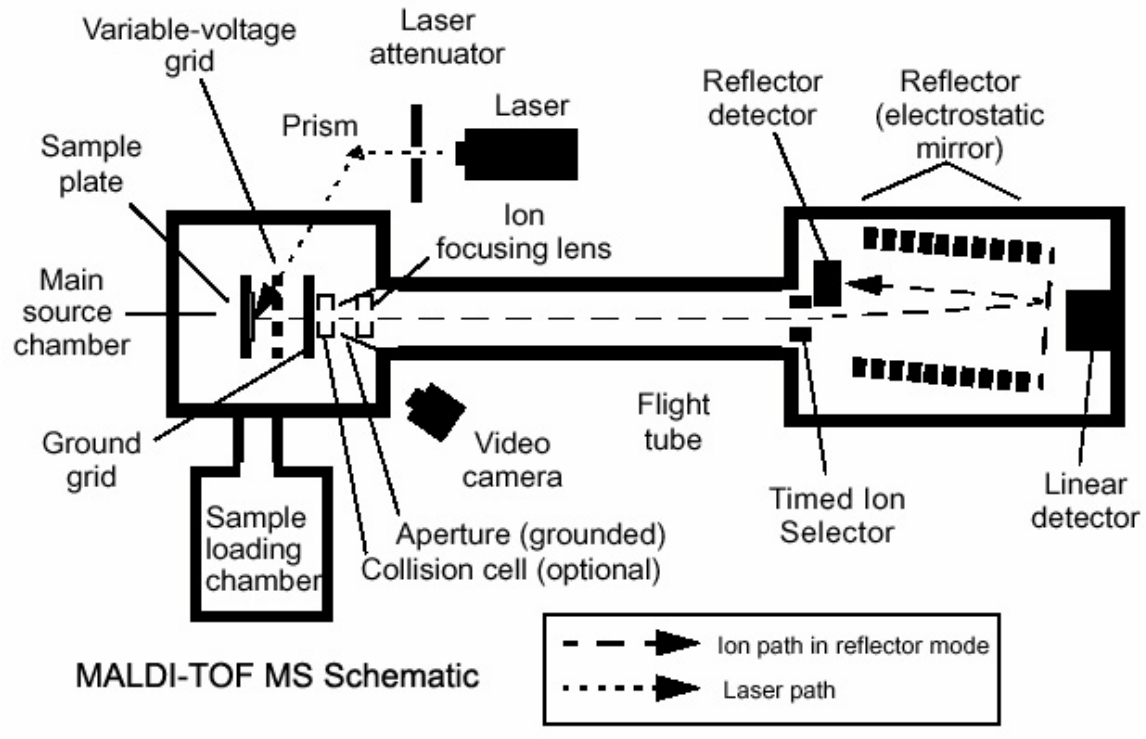

Figure 14. Schematic of MALDI-MS instrument with labeled components [36].

www.manaraa.com

2.3.1.1 Desorption Process

Using laser induced fluorescence, Puretzky et al. [37] was able to capture images of the desorbed plume during the MALDI process (Figure 15), in an attempt to illustrate vapor plume formation and propagation over time. For this experiment, 3-hydroxy picolinic acid (or HPA, with molecular weight of 139 Daltons) was used as the matrix, with the protein Deoxyribonuclease I (29,062 Da) tagged with three tetramethylrhodamine (TMR) dye molecules (444 Da each) serving as the analyte. A KrF laser (248 nm wavelength) was used for primary excitation of the matrix crystals and subsequent plume generation.

Using two different lasers for fluorescence imaging in a narrow sheet configuration, Puretzky was able to image a cross section of the matrix and analyte plume components separately. Figure 15a shows a schematic of the setup. The matrix 3-HPA displays a strong absorption band near 300 nm, so a XeCl laser (308 nm) with pulsed output was used for excitation, yielding luminescence from the 3-HPA at 430 nm. The TMR dye tagged protein absorption band is centered at 555 nm, so a Nd:YAG (532 nm) laser was used in a second harmonic mode to excite the dye, which fluoresced at 580 nm. As seen in the time lapse images in Figure 15b, the lasers used to induce fluorescence were pulsed at microsecond intervals after the initial sample excitation (primary KrF laser) pulse. The fluorescence images were captured using a gated, intensified charge coupled device array.

www.manaraa.com

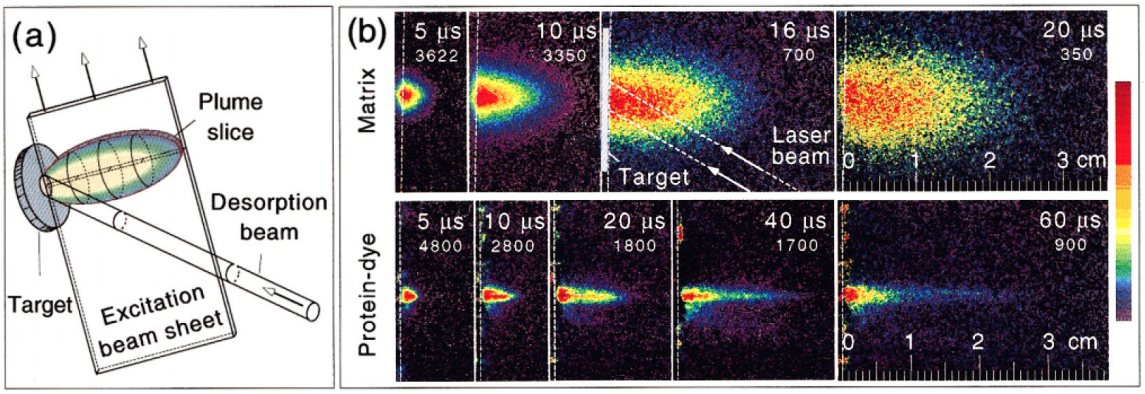

Figure 15. Laser-induced fluorescence imaging of the plume produced in the MALDI process [37]. A schematic of the setup is shown in (a). Imaging of both the lightweight matrix molecule (b, top) and heavier biomolecules vapor expansion (b, bottom), illustrates the differences in the flight path after leaving the sample surface. Copyright 1999 with permission from American Physical Society.

The results show the difference in dynamics of propagation in the plume of the matrix and analyte molecules. The matrix molecules expand rapidly after leaving the sample surface forming an elliptical shaped plume. The heavier analyte molecules display an axial propagation with minimal radial expansion, and a slower velocity than the matrix molecules as noted when comparing the two images taken at 20 µs after the initial excitation beam.

The mechanism for this behavior is thought to be a combination of pressure gradients, collisions, and molecular weight. Puretzky et al. [37] developed a set of differential equations based on gas dynamics and initial conditions to construct a model of plume expansion. He theorized that the lightweight matrix behavior is a result of surface pressure immediately after desorption from the sample and minimal collisions in both the

www.manaraa.com

radial and axial directions. For the heavier protein, the surface pressure is less than that of the matrix due to the smaller initial concentration in the original sample. The initial velocity of the molecules is provided by the desorption process itself, and in the lack of pressure gradients, radial expansion is attributed to collisions with the lighter weight matrix molecules. Additionally, the expansion of the matrix plume might be influenced by charges that the molecules carry as a result of being excited by the primary laser.

As explained later in this section, the energy and diameter of the laser used for plume generation can be factors in instrument resolution as a result of differing plume dynamics. Puretzky [37] showed that axial velocities can differ based upon the laser wavelength, with averages of 600 m per second for 248 nm wavelength to 800 m per second for 193 nm wavelength. Also, the laser spot diameter in his experiment was approximately 3 mm. Therefore, the plume dynamics may differ when using a more common 337 nm nitrogen laser with a spot diameter of approximately 100 μm.

A quantitative model of matrix ionization in the MALDI process using a UV laser was presented by Knochenmuss [38]. The quantum mechanical model details an ion generation process through exciton pooling [39] that was built from previous work on a two-pulse effect [40], where it was demonstrated that the potential for matrix ionization was higher than the available combined energy of two photons from typical lasers used in the MALDI process [41-43]. In this model, 2,5-dihydroxybenzoic acid (DHB) was used as the matrix, and a laser wavelength of 355 nm was used for the energy computations. Previous work by Ehring and Karbach calculated the ionization potential for 2,5-DHB at

www.manaraa.com

8.05 eV for free molecules [39] and 7.82 eV for large clusters [42]. The photonic energy delivered by a laser with a wavelength of 355 nm corresponds to an energy of 3.466 eV. This is illustrated in the energy diagram in Figure 16.

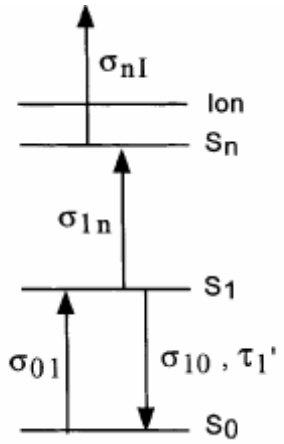

Figure 16. Energy diagram of 2,5-DHB showing laser energy states S_1 and S_n with ground state S_0 and energy required for ionization [38]. Copyright 2002 with permission from John Wiley and Sons.

In this energy diagram, the upward pointing arrows represent the energy added to the system by the photons from the laser. The ground state (S_0) corresponds to the unexcited state of the matrix molecules. The next two states (S_1 at 3.466 eV and S_n at 6.93 eV [42, 43]), represent potentials of the molecule when excited by one photon and two photons, respectively. The top level marked "Ion" represents the energy state (7.82 eV) of the matrix molecule when ionized occurs. The downward pointing arrow from S_1 to S_0 corresponds to spontaneous fluorescence from the excited state to the ground state.

www.manaraa.com

According to the model, two S_1 excitations can pool to form a S_n excitation and a ground state (Figure 17c). The combination of an S_1 and Sn excitation can produce an ion and a ground state (Figure 17d).

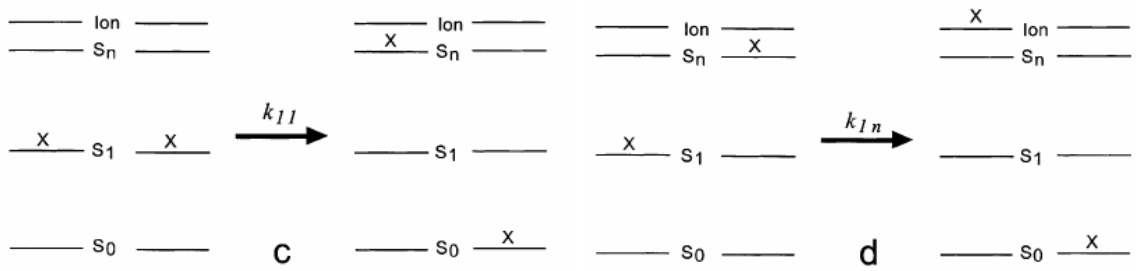

Figure 17. Excitation combinations in the Knochenmuss model [38]. Copyright 2002 with permission from John Wiley and Sons.

Additionally, there is a simultaneous process of non-radiative heating in which electronic S_1 excitations are converted to heat and do not contribute to the ionization process. When the matrix molecules reach the desorption temperature (525-550 Kelvin calculated [38], 440-520 Kelvin measured [44, 45] depending on the matrix) they are liberated from the sample surface at velocities above 600 m per second [46, 47]. Because the desorption is primarily dependent on the S_1 population and occurs within the S_1 time scale, increasing the laser fluence considerably above the plume generation threshold can lead to excessive matrix desorption and increased noise in a sample spectra, which can be verified experimentally.

To demonstrate the exciton pooling of the S_1 state, a fluorescent dye 4-(dicyanomethylene)-2-methyl-6-(p-dimethylaminostyryl)-4H-pyran (DCM) was mixed and deposited with matrix 2,5-DHB [48] and with CHCA [49]. The function of the dye

www.manaraa.com

was to act as a trap, because the primary excited state of the dye is slightly lower than the S_1 matrix state. Since materials seek to maintain minimum potential energy, the excited charges naturally migrate to the area of lowest potential. The energy transferred from the surrounding matrix molecules to the trap (known as "hopping") was released as light (Figure 18), making it unavailable for desorption heating or for ionization.

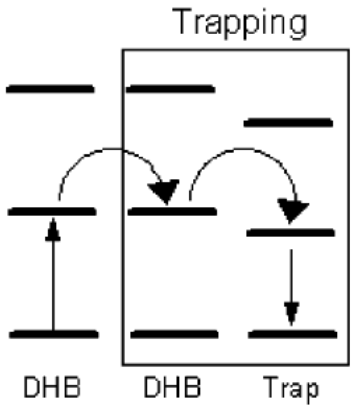

Figure 18. Energy diagram illustrating hopping (exciton transfer) and trapping with fluorescence [48]. Copyright 2005 with permission from American Chemical Society.

The effect on the MALDI process can be seen as a decrease in signal from the matrix and analyte ions. The trap to exciton ratio was the primary parameter for documenting the effect and determining the exciton mobility. The fluorescent emission for matrix DHB is centered at 420 nm, while the dye DCM emits at 640 nm with a concentration dependent intensity. Collecting spectroscopic data over a range of trap concentrations, Setz et.al [48] was able to calculate the average probable exciton hopping distance to be seventeen molecular diameters. To determine the time required for an exciton hop, a grating monochromator coupled with a photomultiplier tube was used to conduct time-resolved

www.manaraa.com

measurements of the fluorescent emissions after single pulses of a 355 nm laser. An average delay of 2 ns between the fluorescence of the matrix and of the dye was observed, which corresponded to an average hop time of $7x10^{-12}$ s for DCM in DHB matrix [48].

2.3.1.2 MALDI Measurement Process

In the MALDI process after the analyte ionization has occurred, the ionized molecules enter the mass spectrometer through an electric field. In a time-of-flight mass spectrometer, the electric field acts to equalize the kinetic energies of the ions so that the velocity of the individual molecule is dependent on the mass. Other components allow mass filtering to increase resolution in the desired mass range, blocking signals with undesired mass to charge ratio (m/z, where z is the elementary charge on the ion) such as the matrix signal. The data from the detector is displayed in a spectrum of signal intensity versus m/z, with peaks corresponding to the biomolecules that were investigated (Figure 19). In order to standardize the measurement for comparison to other spectra, the raw signal intensity is commonly divided by the measurement noise to produce a signal to noise ratio value for each peak. This helps to remove factors that might cause variability from sample to sample.

www.manaraa.com

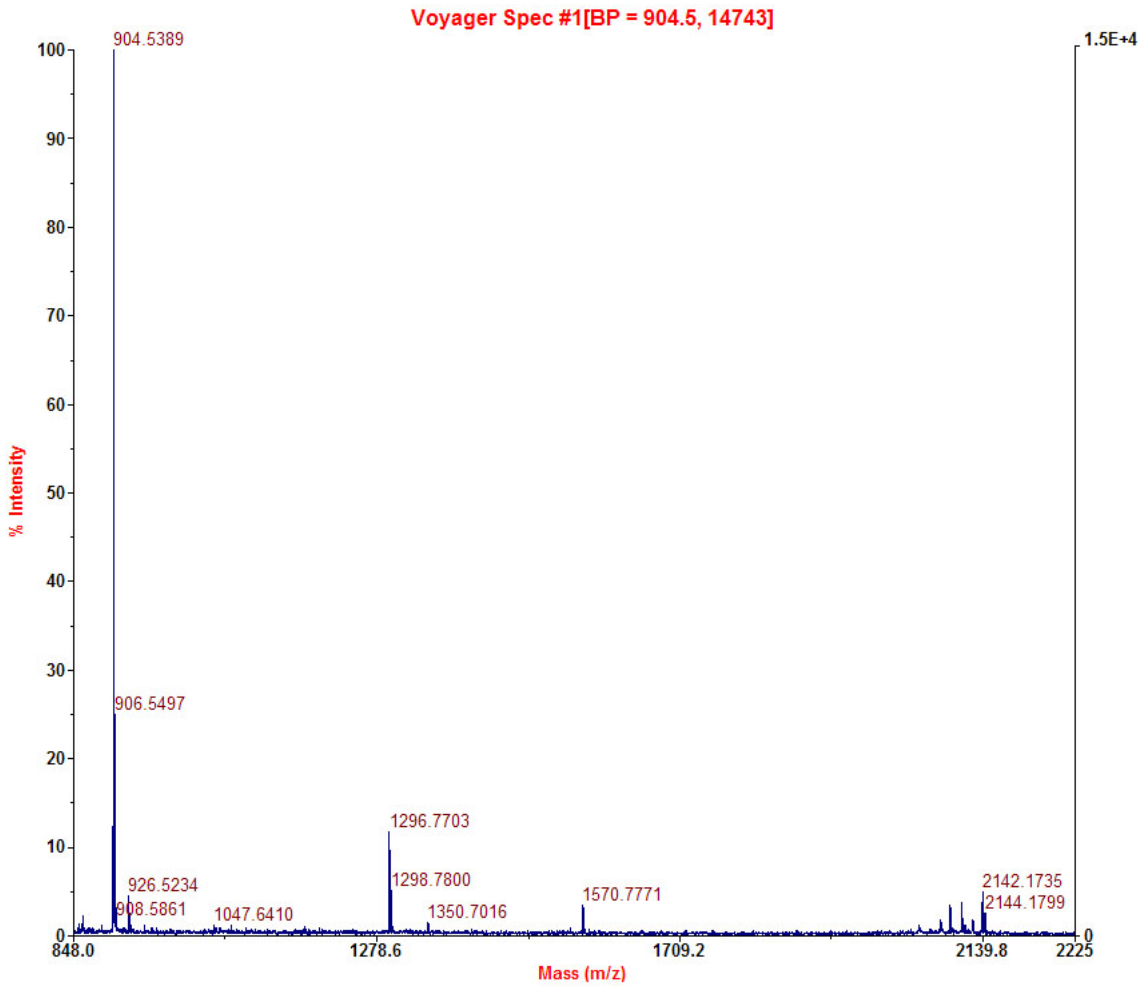

Figure 19. A typical sample spectrum of multiple peptide signals from a Voyager MALDI-MS instrument.

Mass resolution can be calculated from a collected spectrum by dividing the m/z of the peak by the peak width at half maximum, to provide the average resolving power [50] of the instrument and configuration. The mass resolution of a MALDI-MS instrument can be influenced by a number of factors, which can be grouped into two categories: physical instrument configuration, and sample specific factors.

www.manaraa.com

MALDI instrument factors for mass resolution include ion extraction and acceleration fields, laser irradiance on the sample, focal diameter of the laser, and use of ion reflectors in the flight path [51]. Increasing the strength of the ion extraction field can lead to increased fragmentation of analyte ions due to cleavage, resulting in additional peaks at lower m/z values than the primary analyte peak. High ion acceleration potentials can increase the spreading of the initial energy distribution and generation time in the ion generation process, both of which reduce resolution by increasing the peak width.

Commonly in MALDI measurements, laser irradiance is kept within a small range just above the threshold required to produce measurable analyte signals. Ingendoh et al. [51] showed that the peak width increases with increasing irradiance (Figure 20), thought to be caused by the increasing number of S_1 excitations in the matrix crystals, increasing the rate of desorption and the amount of material ablated from the sample surface, leading to increased collisions in the ion acceleration region and widening the energy distribution around the analyte peak.

www.manaraa.com

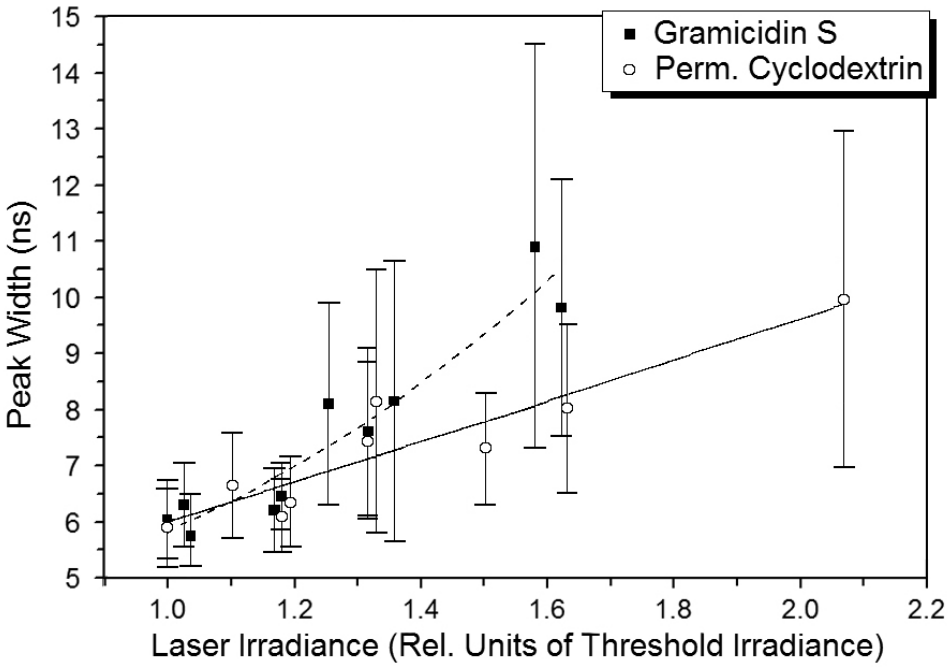

Figure 20. Sample peak width increases with increasing laser irradiance [51]. The enlargement of the error bars indicates increased measurement fluctuation at high laser irradiance. Copyright 1994 with permission from Elsevier.

The laser irradiance axis in Figure 20 is given in relative units of threshold irradiance, which is a ratio of applied irradiance for that measurement divided by the minimum threshold irradiance of the sample spot.

The diameter of the laser in a MALDI instrument that irradiates the sample spot is another factor in determining mass resolution. The standard instrument uses a fixed focal length lens to reduce the diameter of the laser to approximately 70-100 μm. Ingendoh et al. [51] were able to change the focal diameter by using a variable telescope in the beam line to vary the focused diameter between 10 and 280 μm. The laser intensity was adjusted to keep irradiance just above threshold. Figure 21 displays a plot of the data for

www.manaraa.com

required threshold irradiance as a function of focal diameter. The sharp increase below 70 μm diameter is thought to be the combined result of reduced irradiance area and the radial Gaussian energy distribution of the laser beam profile. The use of brilliant green organic dye deposited directly on the metal substrate (without the use of a matrix for ionization) served as a control, and displayed a similar behavior as the matrix-ionized analytes. This behavior supports the theory as to the mechanism behind the relationship between laser diameter and threshold irradiance.

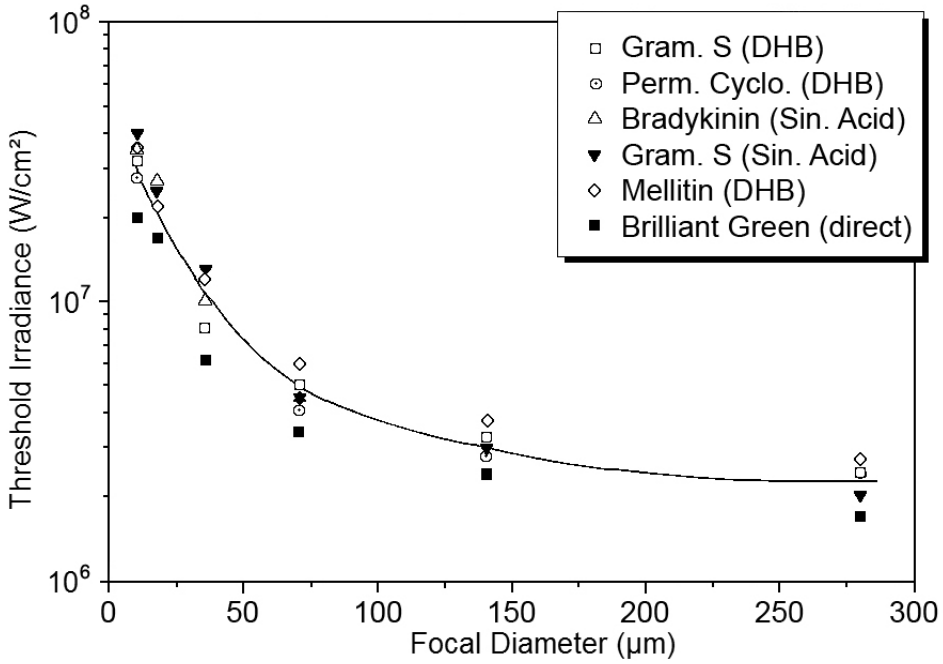

Figure 21. Small diameter laser spot requires higher irradiance to reach signal detection threshold [51]. Copyright 1994 with permission from Elsevier.

As discussed previously, the peak width of the analyte signal can be dependent on laser irradiance. An increase in signal peak width was observed at small laser diameters as a result of the increase in required threshold irradiance (Figure 22). The different analytes

www.manaraa.com

reacted differently to changes in focal diameter, with the exception of the green dye that displayed an unchanged response. The behavior of the green dye (control) affirms the conclusion of the author that the mechanism responsible for increase in peak width occurs in the ionization zone of the plume of desorbed molecules.

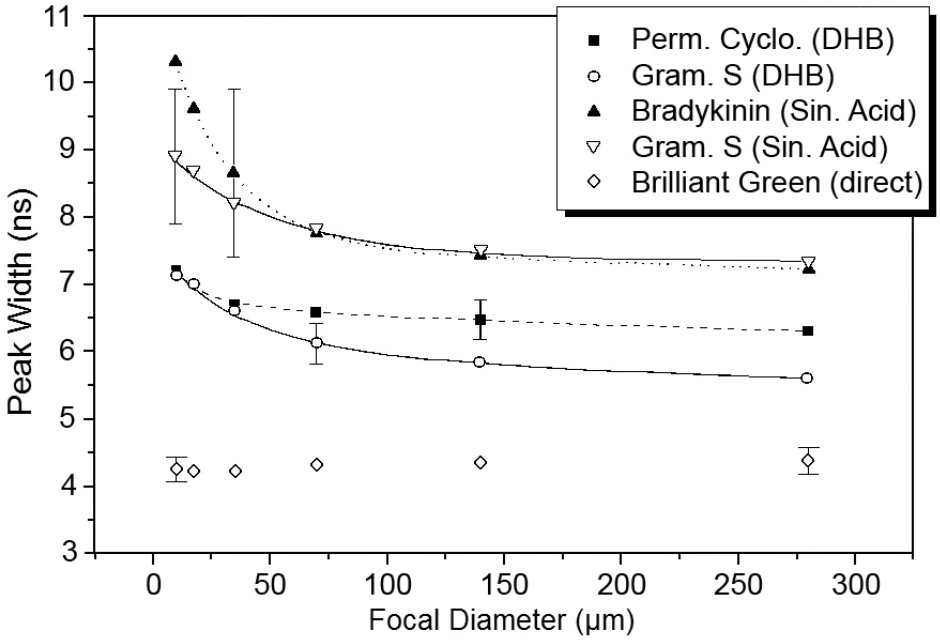

Figure 22. Peak width of analyte signal showing an increase with decreasing laser diameter [51]. Copyright 1994 with permission from Elsevier.

There are several sample related factors that can influence the resolution of the MALDI measurement. The natural isotope distribution of hydrocarbon (C^{12}/C^{13}) molecules can limit peak width, but is only of a real concern for analytes in the middle mass range between 1000 and 4500 Daltons [51]. The use of an ion reflector in the instrument can compensate for the isotopic distribution and increase the apparent mass resolution. Additionally, the formation of adducts between the analyte and matrix molecules and the cationization of those adducts can affect the mass resolution by adding

www.manaraa.com

additional peaks to a spectrum. This can be prevented by the careful choice of matrix for a particular analyte.

2.3.2 MALDI Matrix Materials and Sample Preparation

There are five main types of matrix, and their use is determined by the type of molecule to be investigated. For investigating proteins, sinapinic [52] and ferulic acids are typically used. Sinapinic acid can also be used for peptides, as well as α-cyano-hydroxycinnamic acid (CHCA) [53] and dihydroxy benzoic acid (DHB) [54]. For investigating oligonucleotides and DNA probes, DHB and hydroxy picolinic acid (HPA) can be used. The chemical structures of these matrices can be seen in Figure 23.

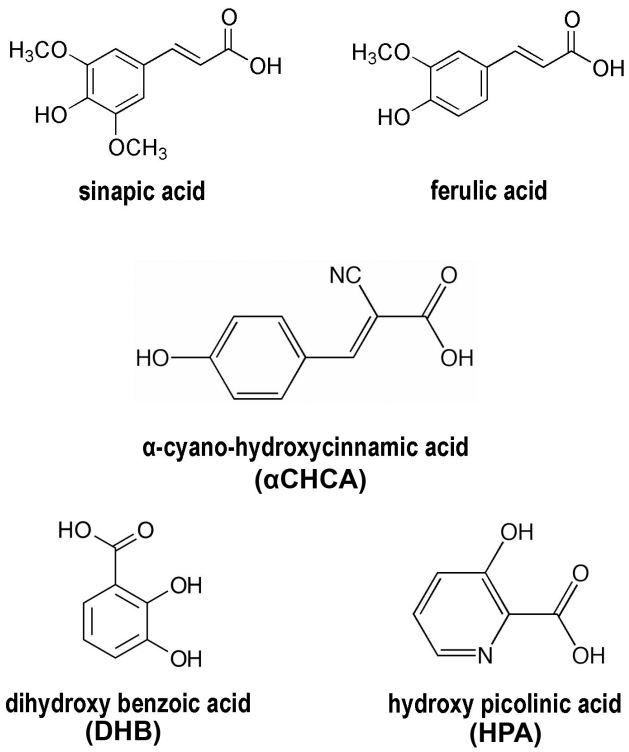

Figure 23. Chemical structures of commonly used matrix molecules.

www.manaraa.com

The natural state of the matrix molecules is a crystalline form. The matrix selected for use is dissolved in an appropriate solvent (typically highly purified water and an organic solvent such as acetonitrile).

There are two main types of sample preparation, sequential deposition in which the matrix solution is deposited on the MALDI plate and allowed to crystallize before the analyte solution is deposited on top [55], and concurrent deposition where the matrix and analyte solutions are mixed before deposition. In the latter technique, the analyte is distributed throughout the matrix and is said to be co-crystallized. The sequential deposition technique has the advantage of increased analyte concentration on the surface of the matrix crystals, if the matrix is not entirely re-dissolved upon analyte application. However, sample homogeneity is affected due to the lack of analyte in the bulk of the matrix crystals, leading to signal degradation over time with increased laser investigation of the same sample spot. The co-crystallization technique produces matrix crystals with a more uniform concentration of embedded analyte, which produces more consistent ion signals over time.

Evaporation speed is also a factor in sample preparation. It has been observed that fast evaporation produces high density fields of smaller crystals [56]. This can lead to an increase in surface area available for laser absorption and analyte desorption compared to the larger matrix crystals that are obtained through slow evaporation. Crystal density on the sample spot can have an effect on the MALDI spectra. An increased number of

www.manaraa.com

crystals in contact can increase the energy pooling efficiency resulting in increased analyte ionization at the crystal surface.

2.3.3 Methods to Improve Sample Homogeneity to Enhance MALDI-MS Sensitivity

2.3.3.1 Fast Evaporation Thin Film

A modification of the sequential sample preparation method, the fast evaporation thin film method involves coating the sample surface with a thin layer of matrix crystals [57]. This is accomplished by using a highly volatile solvent in the matrix solution to provide a rapid rate of solvent evaporation, resulting in a dense film of small, flat matrix crystals.

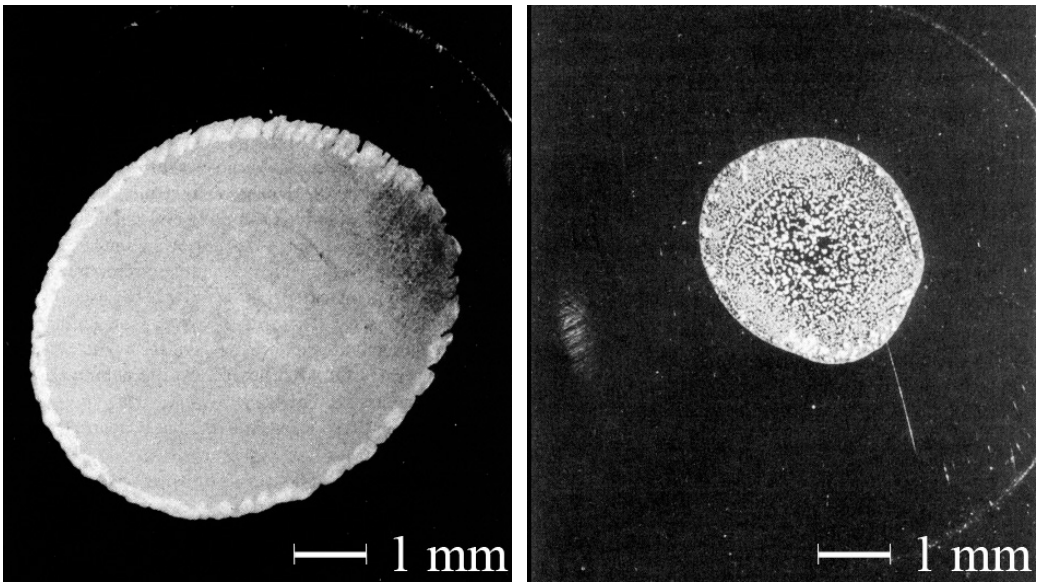

Figure 24. Images of matrix surfaces prepared by fast evaporation (left) and standard two step (right) [57]. Both spots were produced using 0.5 µL of αCHCA matrix solution. Images were contrast enhanced from the published originals. Copyright 1994 with permission from American Chemical Society.

www.manaraa.com

Acetone or methanol is typically used in the CHCA matrix solution to provide the fast evaporation property. The solution is deposited onto a stainless steel sample plate via pipette with deposition volumes between 0.2 µL and 1 µL, so deposition must be performed quickly to prevent solvent loss. The solution spreads across the plate surface and dries in approximately two seconds at room temperature. A matrix crystal film prepared using this technique is shown in Figure 24 (left) next to a film prepared using the standard two step technique (right). The sample prepared using acetone displays more uniform crystal distribution over the increased sample spot area due to the fast spreading and evaporation.

Spot size also varies with deposition volume, with diameters ranging from approximately 3 to 10 mm. Atomic force microscopy of the fast evaporated matrix crystals indicated the average size of the micro-crystals to be approximately 1 µm.

The solution containing the analyte was deposited via pipette onto the center of the matrix crystal film (avoiding the thicker rim) and allowed to evaporate slowly. Ideally with this technique, the analyte solution would re-dissolve only the outer surface of the matrix crystals and not the entire film, therefore proper analyte solvent selection is important. Basic solutions or organic solvents can re-dissolve the matrix crystals leading to non-uniform distributions upon drying. The addition of trifluoroacetic acid (TFA) to the analyte solution can prevent this problem. As the solvent evaporates, the analyte molecules are incorporated into the crystal surface during re-crystallization.

www.manaraa.com

This technique has demonstrated an improvement in data acquisition speed as a result of the homogeneity of the sample and reduced the need to search for a good signal. The irradiance threshold is similar to the traditionally prepared samples, however the intensity of spectra generated at a particular spot decreases rapidly as the matrix is exhausted easily due to the thinness of the micro-crystals. Investigating a different spot on the sample would yield fresh spectra. Multiple spots on the same sample yielded similar spectra at a constant laser intensity setting, demonstrating decreased variability across the surface compared to the standard sample preparation technique.

Additionally, Vorm et al. [57] reported an increase in sensitivity of approximately two orders of magnitude over the conventional samples investigated when using proteins up to 14kDa in mass. However the working range limit for low concentration analytes is in the high attomole range due to contamination and impurities causing dominating peaks that could mask the analyte signal.

2.3.3.2 Electrospray

Electrospray is a technique that uses an electrically-charged, small diameter needle or capillary as an emitter for producing a fine aerosol of charged liquid droplets (Figure 25). The electric force from the applied high voltage is responsible for pulling the ions inside the liquid out of the capillary and forming a Taylor cone [58], supplying sufficient force to overcome the surface tension of the liquid (Figure 26). The resulting jet of charged droplets expands radially to form a plume due to Coulombic repulsion as was theorized by Lord Rayleigh in 1882 [59] and further investigated by Zeleny [60, 61].

www.manaraa.com

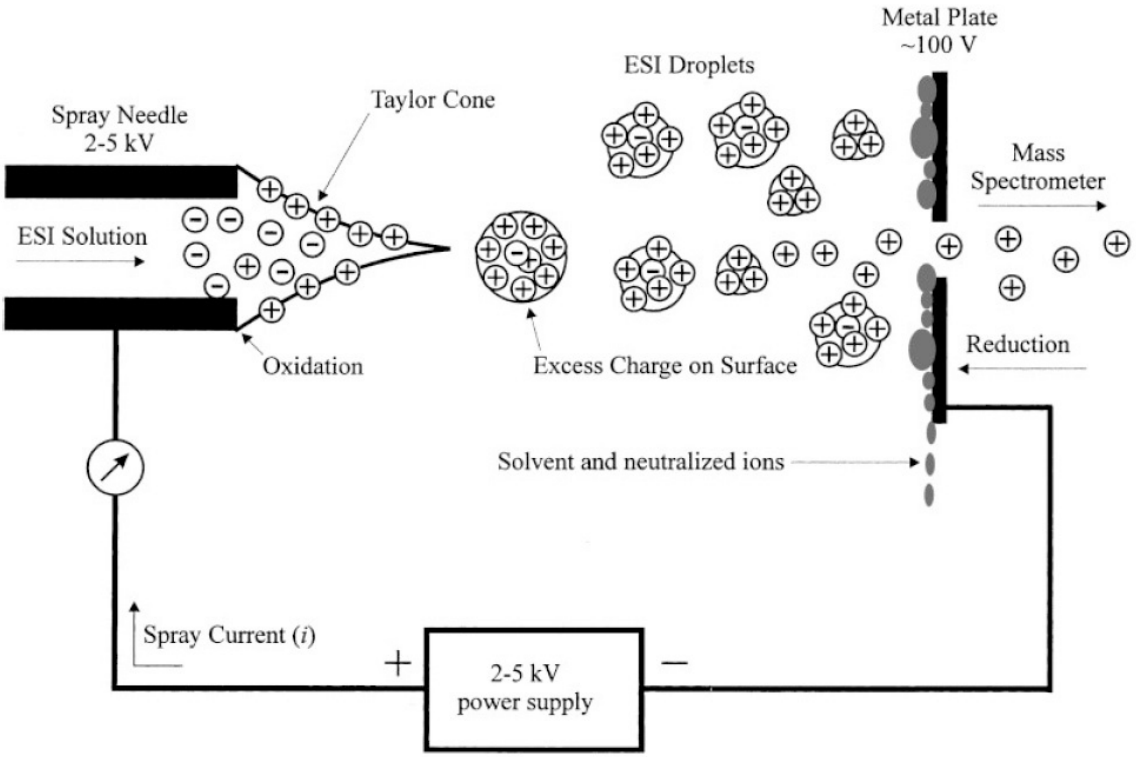

Figure 25. Schematic view of electrospray process [62]. A high voltage is applied between the spray needle and the metal plate. The solvent is evaporated or is deposited on the plate, and a stream of ions is produced for deposition onto a sample or investigation via mass spectrometry. Copyright 2001 with permission from John Wiley and Sons.

www.manaraa.com

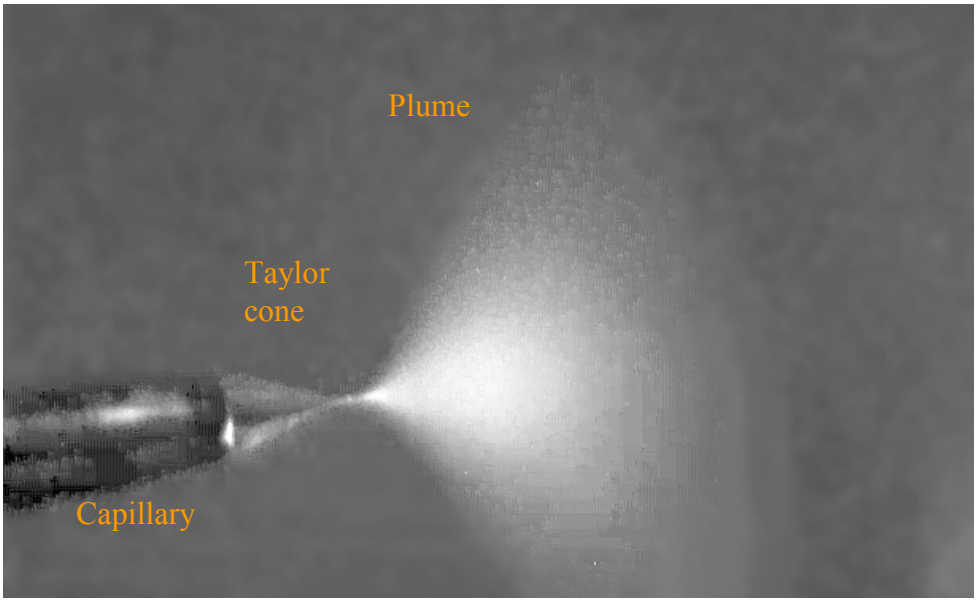

Figure 26. Photograph of electrospray showing Taylor cone and plume at an applied voltage of -2.6kV [63]. Image used with permission from author.

Electrospray has a number of industrial applications for depositing materials onto surfaces. However, since electrospray is a "soft ionization" technique, meaning that the ionized molecules are not fractured during the process, it has been used frequently for biomolecular applications, such as chemical analysis, deposition in vacuum, and interface investigations using photoemission spectroscopy [64-68]. Electrospray is also used for producing ions from solutions containing biomolecular analytes that are introduced directly into a mass spectrometer for analysis, a technique known as ESI-MS [69].

The preparation of samples for MALDI analysis using electrospray was shown by Axelsson et al. [70] to improve sample shot-to-shot reproducibility. The improvement was thought to be the result of increased homogeneity in both crystal composition and size when compared to standard sample preparation techniques. The electrospray

www.manaraa.com

deposition setup can be seen in Figure 27. The voltage on the needle was 8 kV and the needle to sample distance was optimized to provide sufficient time for solvent evaporation from the droplet before deposition.

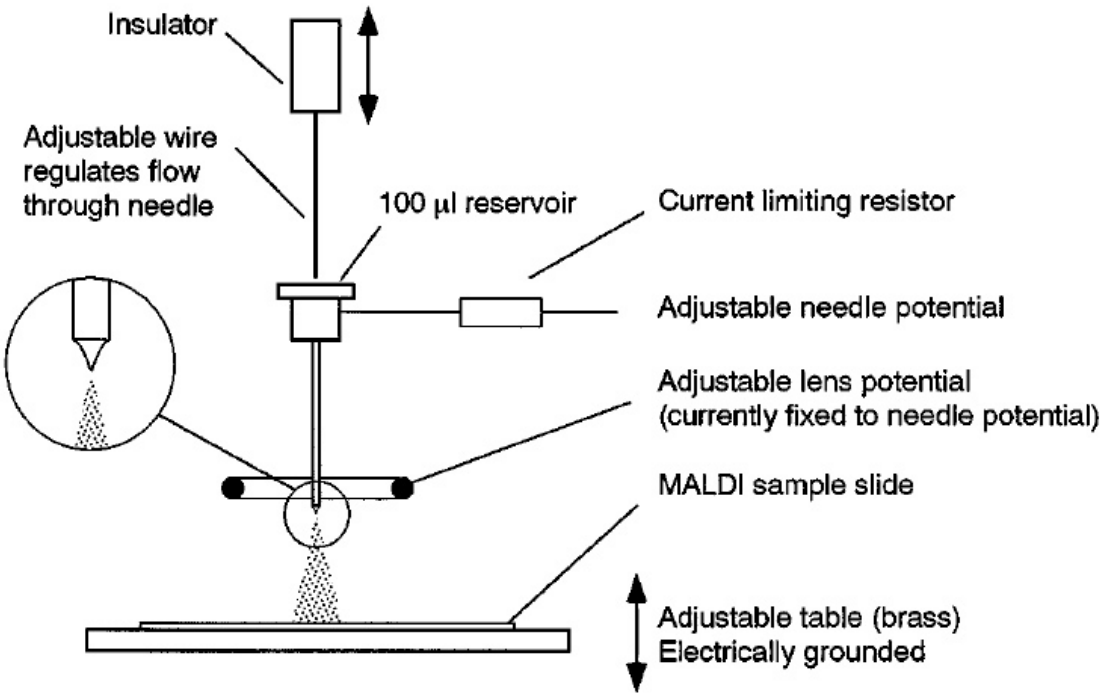

Figure 27. Electrospray setup for MALDI sample preparation [70]. Copyright 1997 with permission from John Wiley and Sons.

The experiment compared different types of sample preparation techniques including one and two step droplet, and one and two step electrospray. The results indicated that the one step electrospray (where the matrix and analyte were mixed and deposited simultaneously) produced the tightest distribution of spectral intensity with the majority of spectra producing 75% of the maximum intensity compared to the one step droplet technique that had a wide distribution and the majority of spectra producing less than 45% of the maximum intensity.

www.manaraa.com

Experiments were performed by Hanton et al. [71] to investigate surface morphology and compare the results of electrospray and standard droplet sample preparation techniques. Scanning electron (see section 2.4), atomic force, and confocal microscopies were all used to investigate the deposited samples. A significant difference in surface morphology between the two deposition techniques is illustrated in the SEM images in Figure 28. Both samples were coated in a thin film (approximately 10 nm thick) of gold to prevent accumulation of charge from the electron beam during imaging. The sample prepared using electrospray deposition showed better surface coverage and increased crystal uniformity over the deposition area.

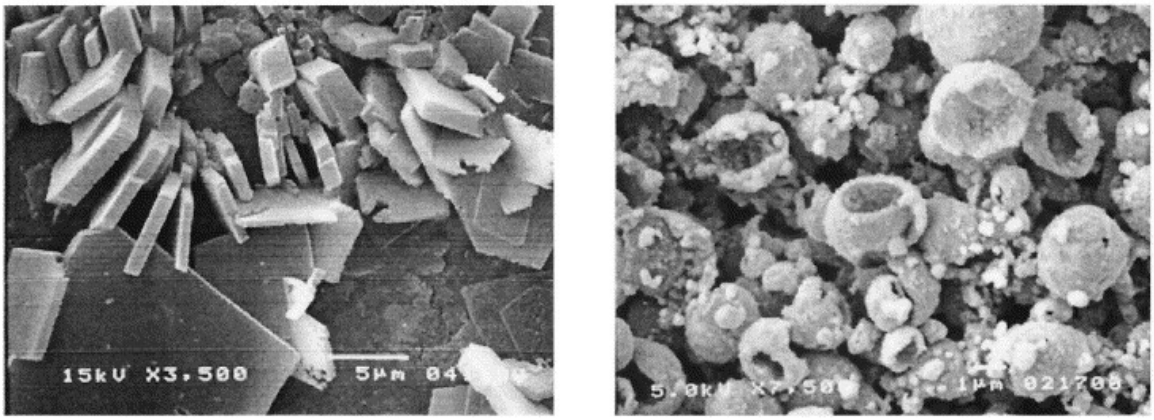

Figure 28. Scanning electron microscope images of MALDI samples prepared by standard droplet deposition (left) and electrospray (right) [71]. Copyright 2004 with permission from Elsevier.

www.manaraa.com

2.3.4 Sample Concentration Methods

2.3.4.1 Pre-structured Sample Supports

One of the techniques designed to decrease sample spot size is the use of patterned areas using hydrophobic and hydrophilic materials. Schuerenberg [72] and his team from Bruker Daltonik have published results using a substrate composed of a hydrophobic Teflon® field with an array of hydrophilic gold spots to act as sample anchors. The 200 µm diameter gold spots are considerably smaller than the diameter of the samples prepared using the traditional dried droplet technique (approaching 1 mm diameter, depending on solution composition, concentrations, and deposition volume). Since the typical laser used in MALDI-MS instruments has a diameter typically between 100-200 µm, the objective of the technique is lateral concentration of the sample onto the anchor spot.

The sample supports used in the experiment consisted of a stainless steel sample plate coated with polytetrafluoroethylene (PTFE, or commonly known as Teflon®) to a thickness between 30-40 µm. Using a photolithographic masking technique, the gold spots were deposited via sputtering to a thickness of 30 nm, with spot diameters ranging from 100-300 µm [72]. Solutions containing matrices 2,5-dihydroxybenzoic acid (DHB) or 3-hydroxypicolinic acid (3-HPA) were deposited via pipette onto the patterned 200 µm gold spots. The time lapse drying images can be seen in Figure 29.

www.manaraa.com

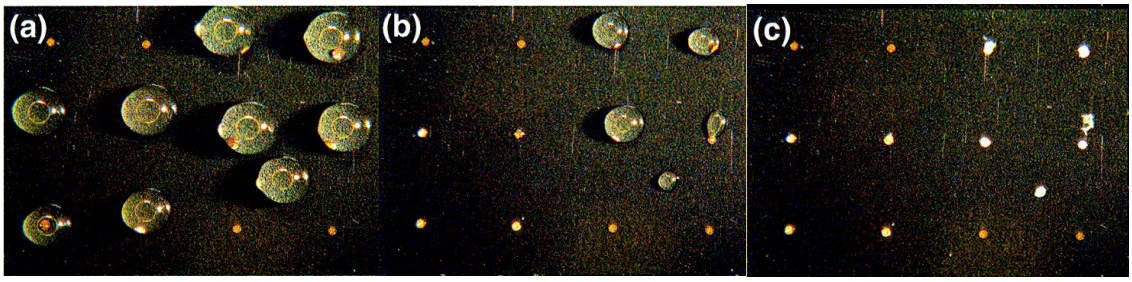

Figure 29. Optical micrographs of droplet drying on the patterned gold structures [72]. Copyright 2000 with permission from American Chemical Society.

The four droplets in the left side of Figure 29a are DHB solutions while the remaining droplets are 3-HPA solutions. All droplets had an initial volume of 1 μL. The images in Figure 29b and c correspond to a time of 5 minutes and 8 minutes after initial deposition, respectively. The samples that were deposited in contact with the gold spots displayed lateral concentration while drying and the final crystalline spot diameter was approximately 200 μm. Interestingly, the one droplet of 3-HPA that was purposefully deposited in between the grid of gold spots (the bottom-most droplet in Figure 29b), also displayed lateral concentration and a similar final dried droplet diameter. The droplets that were not centered on a gold spot during the initial deposition did display preferential anchoring behavior and crystallized on the gold spot, except for one, which the author states was due to surface contamination. While not documented in this paper, the author also states that droplet deposition on traditional metal substrates resulted in non-homogeneous dried droplets with a majority of the matrix crystals forming a ring around the edge and a central area that was either blank or contained microcrystals, which is consistent with the results found in this work when using this technique.

www.manaraa.com

The experiments performed with the 100 µm and 300 µm diameter gold spots revealed further information concerning the importance of matrix composition and concentration regarding successful lateral concentration during drying. For the 100 µm spots, the DHB solution dried spot size was that of the gold anchor. However the 3-HPA samples exceeded the gold spot diameter, thought to be a result of excess matrix material in solution. The author also reported in several instances the shrinking sample droplet would leave the gold spot and crystallize on the surrounding Teflon surface. Investigations with the 300 µm diameter gold spots revealed that the drying crystals resulted in structures that resembled those on plain metal, with a thicker crystalline rim and a blank center area. This was thought to be a result of insufficient matrix concentration in solution, as this phenomenon was avoided by increasing the matrix concentration previous to droplet deposition [72].

2.3.4.2 Automated Nano-liter Pipette Deposition

A precision method for ultra low volume sample preparation was presented by Little et al. [50]. His system utilized a glass capillary with a 70 µm inner diameter coupled with a piezoelectric element and driver to deposit droplets of approximately 300 pico-liters onto a substrate consisting of a grid of chemically etched wells. The grid spacing (1 mm pitch) and well size (800 µm square, 100 µm deep), was consistent across the substrate surface and a computer controlled robotic xyz stage was used for automated deposition. Preparation time for a 100 sample array was under four minutes.

www.manaraa.com

The matrix used in the experiment was 3-HPA (0.3 M concentration in H_2O and acetonitrile), and deposited first with 15-20 droplets (4.5-6nL) per well. Evaporation occurred in less than 10 seconds after deposition. After all wells were deposited, the process was repeated for the analyte, depositing 6nL of aqueous oligonucleotide solution on top of each matrix spot. Evaporation and re-crystallization occurred within 20 seconds. The resulting sample spots were approximately 100 μm in diameter and composed of microcrystals in the 5-25 μm range (see Figure 30).

Data collection for MALDI-MS analysis of the samples was performed in a semi-automated scanning mode, collecting 20 laser shots per spectra and averaging 18 samples per minute. Since the sample spot diameter was similar to the diameter of the laser, it was not necessary to manually hunt for a good signal.

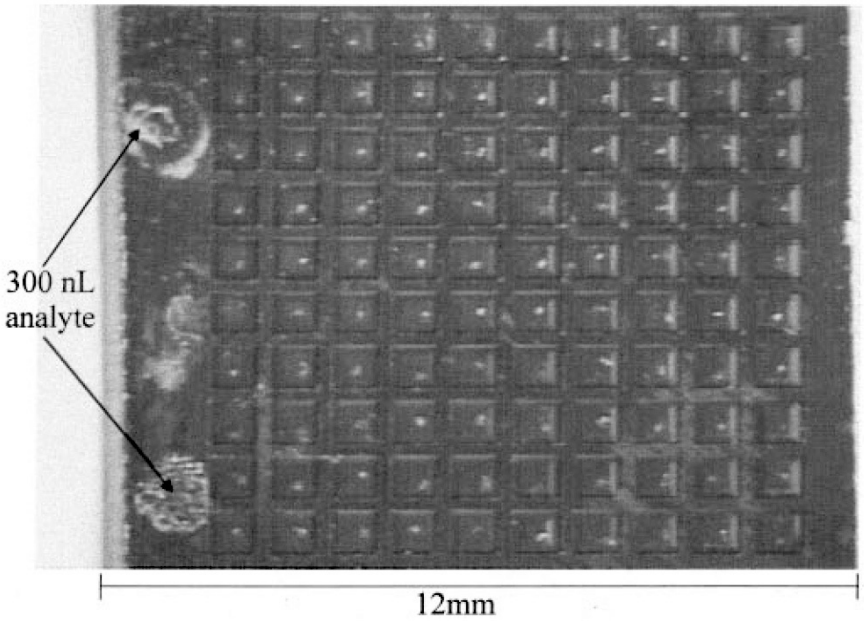

Figure 30. Array of MALDI samples prepared by piezoelectric pipette deposition [50]. Copyright 1997 with permission from American Chemical Society.

www.manaraa.com

The sample spectra collected from the array displayed a high degree of reproducibility in signal intensity and peak width. The author also reported a discernible signal at analyte concentrations of 45 nM, which represented an order of magnitude increase in sensitivity for oligonucleotides in the 30-50-mer range than what was reported by others at that time [73-75].

The sensitivity of this technique is not constant for all analytes and decreases with increasing size of the oligonucleotide. The author states that the signal intensity for the 36-mer analyte is approximately 20% of the intensity of the 15-mer, with another decrease for the 60-mer oligonucleotide samples.

2.4 Scanning Electron Microscopy

A scanning electron microscope is an instrument that creates and directs a focused beam of electrons onto the surface of a sample for the purpose of capturing an image of sample features at greater magnification than is possible using a conventional optical microscope. The apparatus consists of an electron column, sample manipulator stage, and electron detector connected to a vacuum chamber (Figure 31). The process typically occurs in vacuum (1x10-9 torr for the electron column to 1x10-4 torr for the sample chamber) to reduce the spreading of the electron beam due to atmospheric molecular interactions, however low vacuum SEM is possible in specialized instruments. The high vacuum in the electron column provides an insulating effect to prevent arcing across high voltage components.

www.manaraa.com

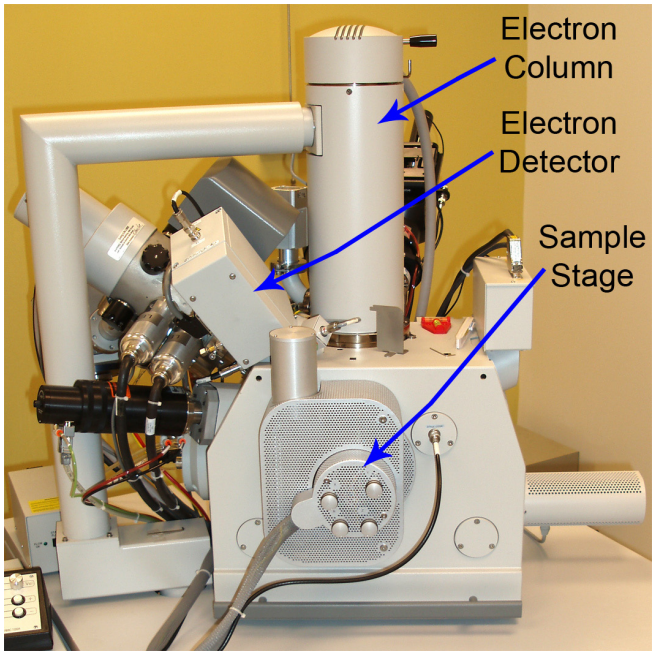

Figure 31. External view of a Quanta 3D (FEI company) with labeled SEM components.

The electrons are typically produced by an electron gun that is at the top of the electron column. Figure 32 shows a schematic of a Field Emission Gun (FEG) [76] that uses high voltage to extract electrons from a cathode filament. The electrons are then accelerated by an additional high voltage field applied at a second anode.

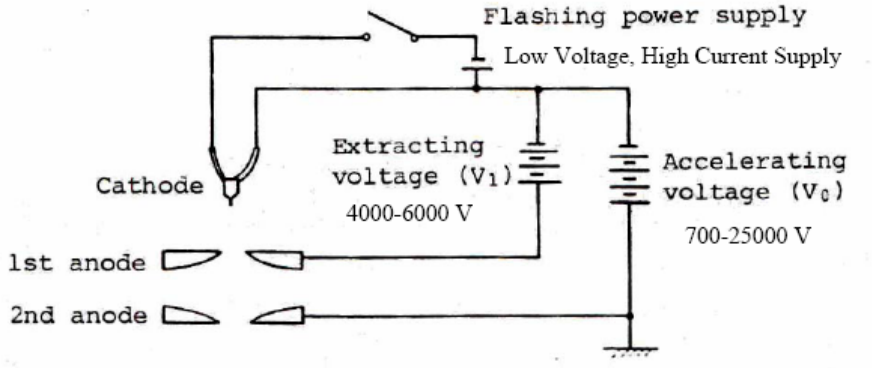

Figure 32. Diagram of field emission electron source [77]. Image used with permission from author.

www.manaraa.com

The electrons that leave the source travel through a series of electromagnetic lenses that focus the electrons into a beam (Figure 33). Thin metal strips with small circular holes called apertures can be placed in the beam line to change beam width and reduce the electron beam intensity. Additional electromagnetic coils along the beam are responsible for deflecting the beam in the X and Y directions to produce a raster scanning pattern on the sample surface [78].

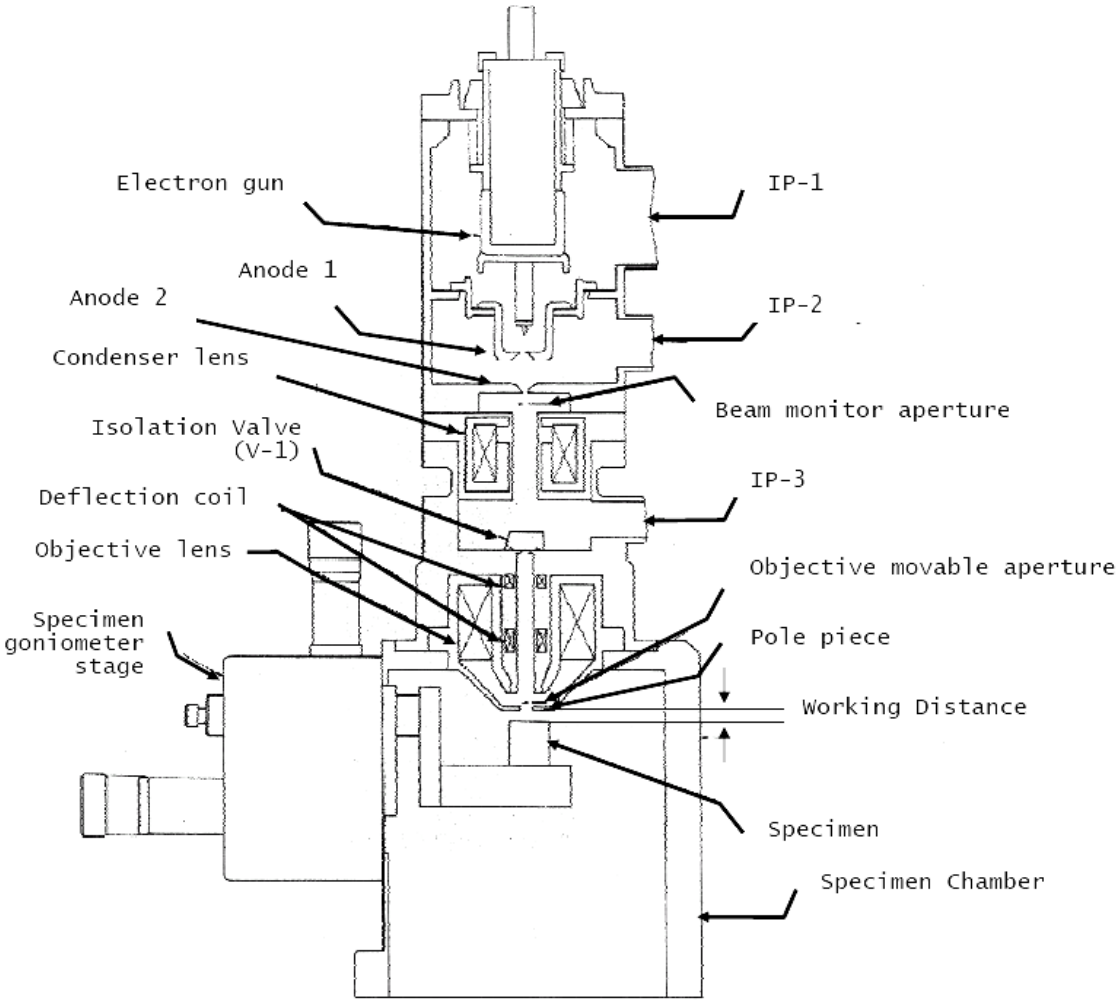

Figure 33. Schematic of Scanning Electron Microscope internals and electron column [77]. Image used with permission from author.

www.manaraa.com

A number of interactions occur between the electron beam and the sample slightly below the surface (Figure 34). Auger electrons [79] are ejected out of the sample by the primary electron beam. Backscattered electrons [80] are electrons from the primary beam that are deflected by the interaction with atomic nuclei and leave the sample surface. Electrons that are absorbed by the material cause atomic excitation and result in the spontaneous release of secondary electrons, X-rays, or mechanical vibration (heat) as the material returns to the previous state [80].

The depth at which these effects occur varies with the type of material and the beam energy (determined by the accelerating voltage at the electron source). The energy level for each type of generated electron determines the maximum depth from which the electron can escape the material. Low energy Auger electrons can only be detected from a depth of less than 5 nm from the sample surface. Secondary electrons (SE) are detectable from depths between 5 and 50 nm into the material. Backscattered electrons (BSE) are considerably more energetic as a result of initial kinetic energy and can be detected from a depth of 1 μm and generated X-rays detectable up to 3 μm from the sample surface (depending on material and other factors).

www.manaraa.com

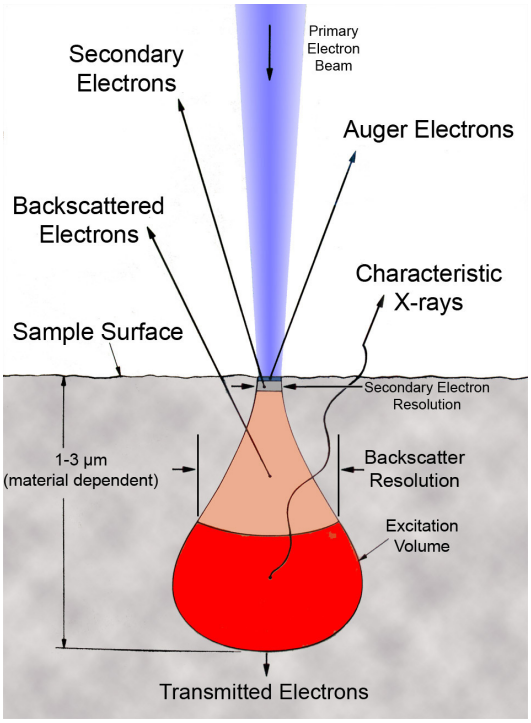

Figure 34. Illustration of electron beam interaction with solid sample.

The electron detector collects electrons and generates a digitized signal that is sent to a display or computer. The signal is collected in real time as the electron beam is scanned over the sample to generate a two dimensional map of the sample surface. Changes in signal intensity are caused by variations in electron emission at different points on the sample due to sample topography and inhomogeneous elemental composition and generate contrast in the collected image [81]. Contrast from sample topography is a result of edge effect, shadowing, and inclination (Figure 35). The edge effect is caused by increased electron emission from the sides of a surface structure and appears as a bright outline of the feature in the image. Shadowing occurs when an object or feature is between the electron beam and the underlying surface or between the surface and the electron detector. Inclination is the result of non-perpendicular beam interaction with the

www.manaraa.com

sample. The interaction volume may be distorted by the structure of the bulk material and lattice orientation, which can lead to non-symmetrical electron emission.

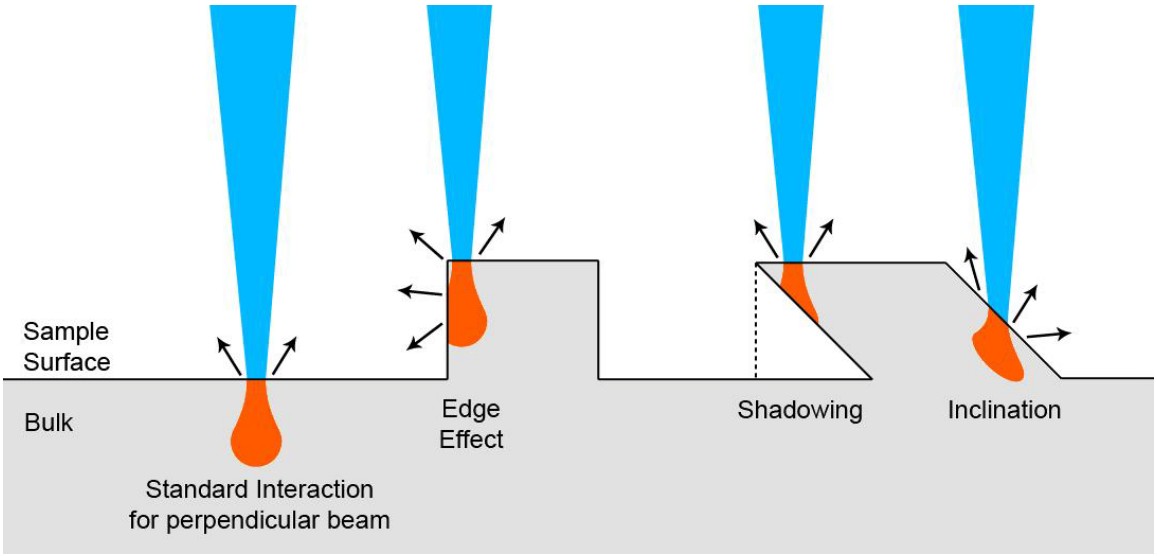

Figure 35. Illustration of sample topography effects on electron beam interaction in scanning electron microscopy.

Contrast due to elemental composition is evident when detecting backscattered electrons. The electron signal intensity typically increases with atomic number (Z) as a result of increasing backscattering yield [81]. Differences in crystal orientation of the material is also detectable using a BSE detector, as the propagation of backscattered electrons is dependent on the electron beam angle of incidence in relation to the lattice planes [82]. Due to the larger interaction volume in the sample material, a BSE image typically displays lower resolution than a comparable SE image.

The Everhart-Thornley detector [83] shown in Figure 36 is able to detect both secondary and backscattered electrons depending on the polarity charge placed on the

www.manaraa.com

collector screen. Both signals are collected when the collector screen is held at a positive potential (+250V). When a negative potential (-100V) is applied to the screen, the low energy secondary electrons are repelled and only the higher energy backscattered electrons are collected.

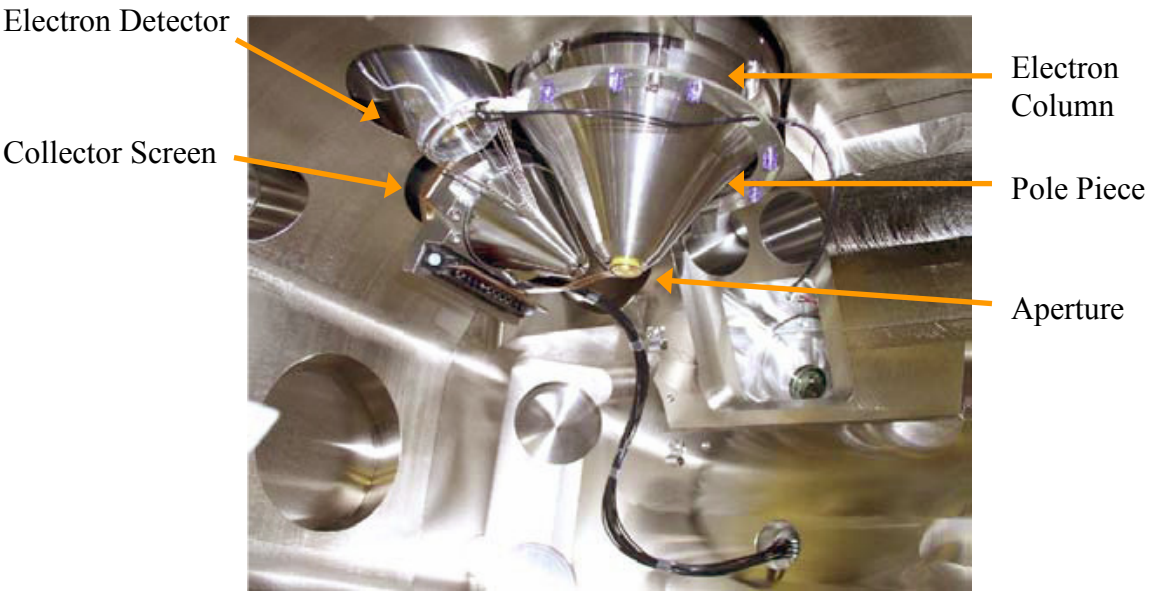

Figure 36. Internal view of Quanta 3D with labeled SEM components.

Electrical conductivity can influence the interaction of the incident electron beam with the sample. For a conductive sample, a simple connection to the grounded stage is needed to provide a path for dissipating electrical charge. A non-conductive sample has insulating properties and can accumulate negative charges from the electron beam and deflect the incoming electrons away from the region of interest on the sample (known as drifting).

www.manaraa.com

Chapter 3: Methods and Materials

3.1 Preparation of Carbon Nanotubes

3.1.1 Catalyst Thin Film Deposition

The Plasma-Enhanced Chemical Vapor Deposition (PECVD) growth method as described in section 2.1.2 was used here because, as a catalyst dependent process, patterning the catalyst (using industry standard techniques) permits strict control of growth location and creation of well defined areas of carbon nanotubes.

Electron beam evaporation (outlined in section 2.2) was used to deposit the catalyst onto the substrate to create samples for carbon nanotube growth. The catalyst used was nickel as a result of previous successful CNT growth [84]. Nickel pellets of 99.9% purity were purchased from Alfa Aesar (Ward Hill, MA) and placed in a new crucible liner from MDC Vacuum Products (Hayward, CA). A Varian Semiconductor (Gloucester, MA) model 980-2462 electron beam evaporator was used to deposit the nickel onto an n-type (111) silicon wafer that was cleaned using a standard sequential rinse of acetone, isopropyl alcohol, and methanol and dried with nitrogen. The wafer was placed in the evaporator's vacuum chamber which was then pumped down to high vacuum ($1x10^{-6}$ Torr) using a combination of roughing, turbo-molecular, and cryogenic pumps [85]. The pressure was measured using a Varian Semiconductor model 845 ion gauge/controller. A high voltage of 10.5 kV was applied to the electron emitter and the emission current was continuously adjusted to provide a stable 1.5 Å (Angstroms) per second deposition rate as

www.manaraa.com

measured by a Sigma Instruments (Fort Collins, CO) SQM-160 quartz crystal thickness monitor placed in vacuum near the silicon wafer. A combination of three physical masks with rectangular grids of 1 mm diameter holes (with 3.3 mm grid spacing) were overlapped to form an opening that was approximately 200 µm tall by 150 µm wide (Figure 37). This was placed in contact with the front of the silicon wafer (in the direction of the evaporation source) and used to pattern the nickel.

The final deposition thickness was approximately 20 nm as measured on a witness sample (deposited simultaneously) using a Dektak 3030ST surface profilometer (Veeco Instruments Inc., Plainview, NY) with settings appropriate for high resolution measurements such as low scan speed and small measurement range. The result was a silicon wafer with nickel deposits approximately 20 nm in height surrounded by clean silicon (Figure 38). These samples were used in the PECVD chamber to create small patches of carbon nanotubes for MALDI sample concentration experiments.

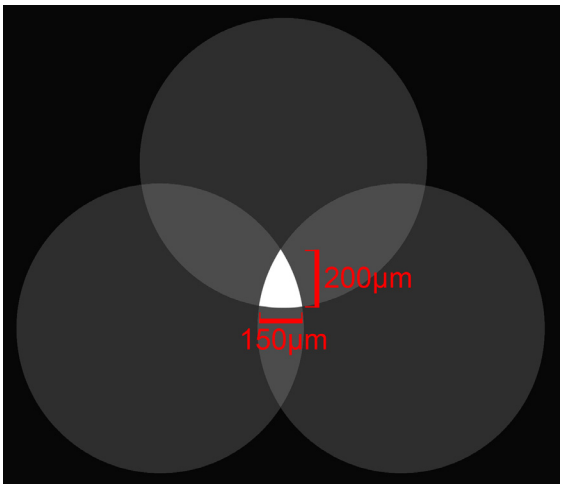

Figure 37. Triple mask overlap forming a window with dimensions 200 x 150 µm.

www.manaraa.com

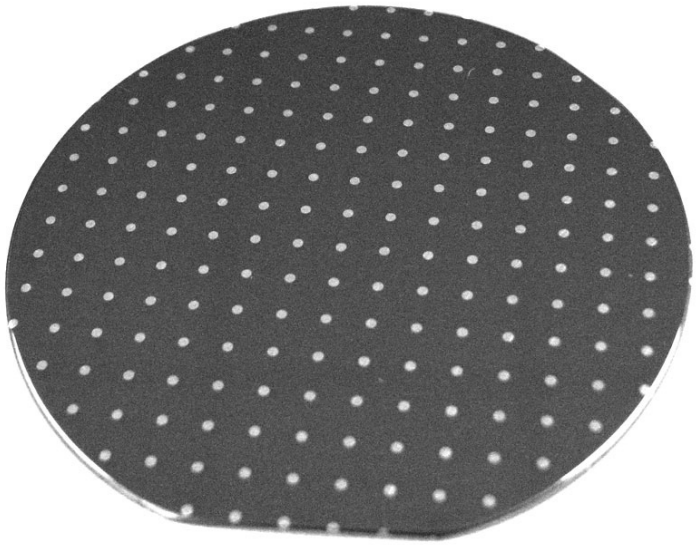

Figure 38. Silicon wafer with 1 mm patterned nickel deposits (lighter spots). Image only for reference as the smaller nickel deposits were difficult to photograph.

3.1.2 Carbon Nanotube Growth

Carbon nanotube growth was accomplished with a prototype PECVD reactor (Figure 39) built in-house using ultra high vacuum components sourced from Kurt J. Lesker Company (Clairton, PA) and MDC Vacuum Products (Hayward, CA).

www.manaraa.com

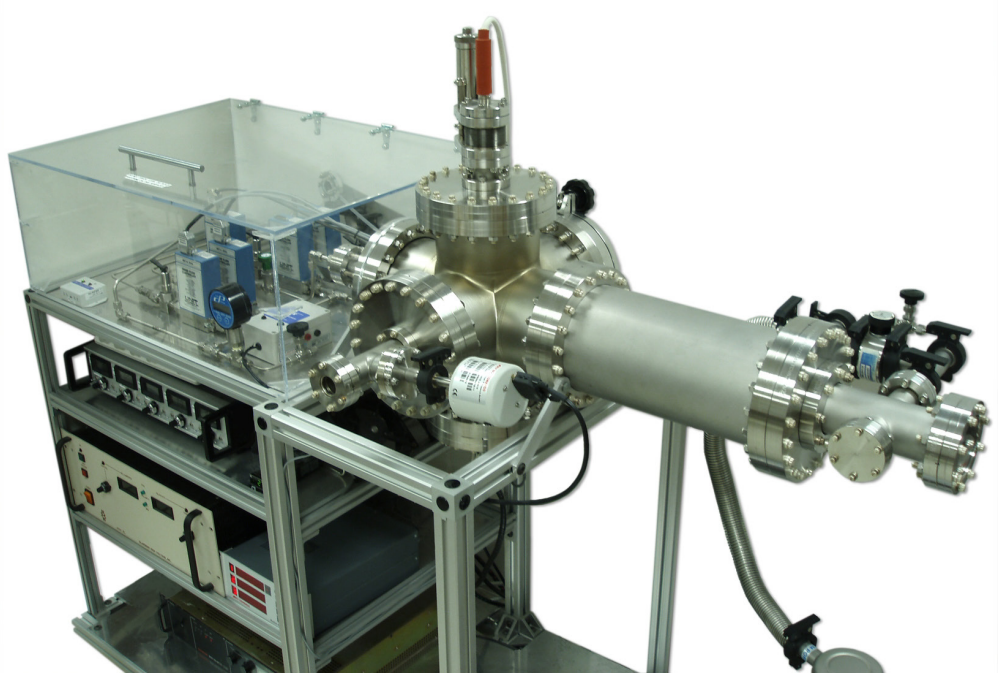

Figure 39. Prototype PECVD reactor for carbon nanotube growth.

The wafer with patterned nickel was manually diced into pieces approximately 1 cm^2 using a diamond-tipped scribe (Ted Pella Inc., Redding, CA). A single layer of these silicon pieces was placed onto a machined copper substrate heater in the center of the reactor (see Figure 40), which was then pumped down to a low base pressure of approximately 1 milli-Torr (1x10-3 Torr) to evacuate atmospheric gasses with an Edwards (Tewksbury, MA) model 30 two-stage roughing pump. Vacuum was measured with an Edwards Barocel 600 series capacitance manometer rather than traditional filament-based gauges because of the corrosive environment (e.g. hot gaseous ammonia) inside the reactor during operation.

www.manaraa.com

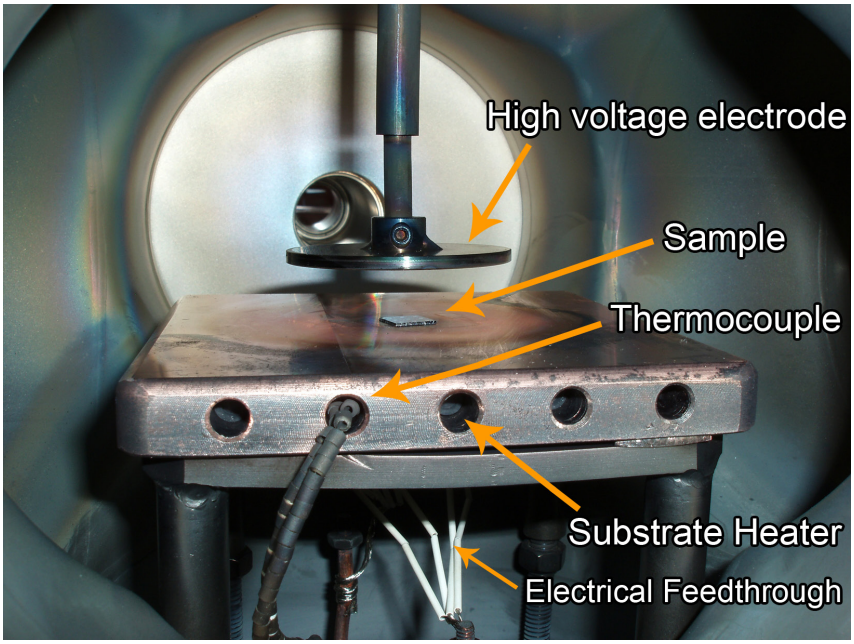

Figure 40. Interior of PECVD reactor with labeled components.

Simultaneously, the substrate was heated to approximately 600 ºC using Omega Engineering (Stamford, CT) CSH series stainless steel cartridge heaters powered by a Sorensen (division of Ametek Programmable Power Inc., San Diego, CA) model DCS 150-20 direct current power supply. Temperature was measured using a JK type thermocouple attached to the side of the substrate heating stage and connected to an Omega CNi series programmable temperature controller. The measured temperature was previously calibrated to the sample temperature to ensure correct measurement since direct measurement is not possible during CNT growth due to interference from the upper high-voltage electrode and resulting plasma.

Once the sample temperature reached the target and stabilized, gaseous ammonia (NH_3, Anhydrous grade 4) and acetylene (C_2H_2, Atomic Absorption grade) (both supplied by Airgas, Radnor, PA) were introduced into the reactor from storage tanks

www.manaraa.com

through a system of mass flow controllers (MFC) sourced from Unit Instruments Inc. (Yorba Linda, CA) model UFC-1660 connected to a model URS-100-5 MFC controller (Figure 41).

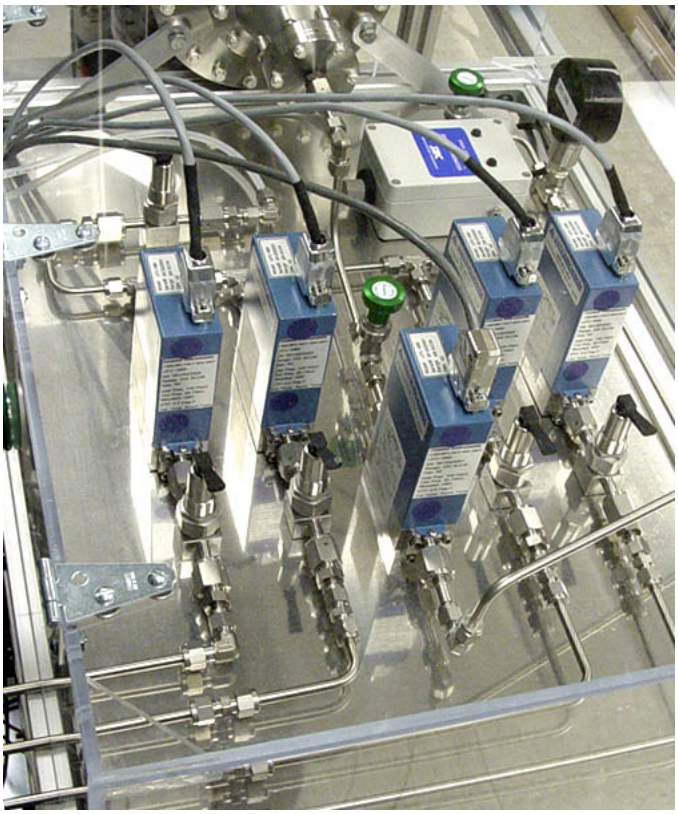

Figure 41. MFC manifold for gas flow and ratio control.

The MFCs are connected by ¼" diameter 316 stainless steel tubing from Grainger Industrial Supply (Lake Forest, IL) with appropriate size valves and fittings from Swagelok (Solon, OH). The entire manifold is encased in a box made from ¼" thick acrylic sheet and is equipped for leak detection with a combustible gas monitor and ammonia monitor from Sierra Monitor Corp. (Milpitas, CA), models 2001 and 2050 respectively. Additionally, the enclosure is connected to a scrubber system that produces a continuous suction to evacuate any fumes in the event of a leak.

www.manaraa.com

The ammonia to acetylene ratio for successful CNT growth in this reactor was previously found [84] to be 4:1 with a combined flow of 500 standard cubic centimeters per minute (SCCM) as controlled by the MFCs. Chamber pressure during the growth phase is held constant at a value between two to three Torr by the use of a throttling valve on the line between the chamber and the roughing pump. Once the target pressure is achieved, a DC high voltage is applied to the upper plate electrode (see Figure 40) using a Glassman (High Bridge, NJ) power supply model KL5R600. The substrate heater is grounded and acts as the opposite parallel electrode. The voltage causes an ionization of the gases, resulting in plasma formation. The power supply is set in a current limiting mode and the voltage is allowed to change as necessary, higher voltage for initial plasma striking and lower for operation. The constant current also limits the destructive capacity for arcing discharges between the electrode and other parts of the chamber. The combination of energy from the heated substrate (thermal energy) and from the high-voltage plasma (electrical energy) act to decompose the gas mixture into its component atoms, which contribute to carbon nanotube growth. The mechanisms are discussed in section 2.1.2. Growth time was thirty minutes, at which point gas flow was stopped, all power supplies were turned off, and the samples were allowed to cool to room temperature in vacuum to avoid potential rapid oxidation if exposed to atmosphere while at growth temperature.

Post-growth morphology analysis of the CNTs was performed using a Hitachi (Hitachi High Technologies America, Pleasanton, CA) model S-800 Scanning Electron Microscope. Image capture was accomplished with a Phoenix digitizing system from

www.manaraa.com

EDAX (a division of AMETEK Inc, Mahwah, NJ) running proprietary Genesis image capture software. A typical sample of carbon nanotubes grown for this work can be seen in Figure 42. Adobe Photoshop CS3 Extended (Adobe Systems Inc., San Jose, CA) software was used for contrast enhancement of images.

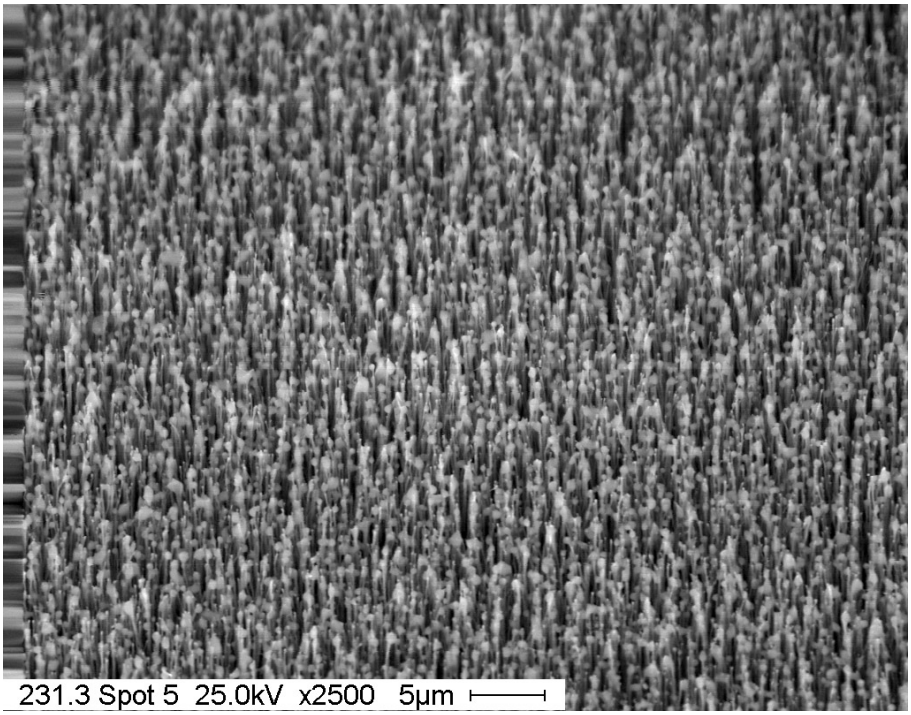

Figure 42. SEM image of carbon nanotubes grown from 20 nm thick nickel catalyst.

Using the measurement tools in the Genesis software, CNT dimensions were quantified. Average CNT length was 2.5 µm with an average width of 110 nm. Carbon nanotube growth was uniform across the catalyst deposited area and maintained overall dimensions similar to the initial patterned catalyst dimensions.

www.manaraa.com

3.2 Chemicals and Materials

Matrix α-cyano-4-hydroxycinnamic acid (αCHCA) was purchased from Sigma-Aldrich (St. Louis, MO) and high-purity acetonitrile was purchased from Burdick and Jackson (Morristown, NJ). Peptide standard Mariner CALMIX 4700 (consisting of des-Arginine^{1}-Bradykinin (m/z 904), Angiotensin I (m/z 1297), Glu^{1}-Fibrinopeptide B (m/z 1569), and Adrenocorticotropic Hormone (ACTH) (1-17 clip) (m/z 2092)) was purchased from Applied Biosystems (Foster City, CA), and will hereby be referred to as Peptide Mixture 1. For further technical information regarding the function of the individual peptides, see Appendix A. The water used was obtained from a Milli-Q water purification system (Millipore, Milford, MA) with a resistivity of 1.8×10^{8} ohm per centimeter (Meg Ω-cm) indicating highly purified water. Cleaning solvents such as acetone, isopropyl alcohol, and methanol were purchased from J.T. Baker (a division of Mallinckrodt Chemicals, Phillipsburg, NJ).

www.manaraa.com

Table 1. Amino acid sequences for each respective peptide contained in Peptide Mixture 1. The amino acids in red indicate the presence of a carbon ring.

Analyte Component	Sequence
des-Arginine[1]-Bradykinin	H - Pro - Pro - Gly - Phe - Ser - Pro - Phe - Arg – OH
Angiotensin I	H - Asp - Arg - Val - Tyr - Ile - His - Pro - Phe - His - Leu – OH
Glu[1]-Fibrinopeptide B	H - Glu - Gly - Val - Asn - Asp - Asn - Glu - Glu - Gly - Phe - Phe - Ser - Ala - Arg – OH
Adrenocorticotropic hormone (ACTH)	H - Ser - Tyr - Ser - Met - Glu - His - Phe - Arg - Trp - Gly - Lys - Pro - Val - Gly - Lys - Lys - Arg – OH

3.3 MALDI Sample Preparation

For initial experiments, a solution of 1:1 volumetric ratio of acetonitrile to de-ionized water was prepared as a matrix solvent. Dry crystalline matrix αCHCA was weighed out with a Sartorius Research (Goettingen, Germany) model R200D digital precision balance and combined in a 1.5 mL Eppendorf® Safe-Lock Microcentrifuge tube (Westbury, NY) with sufficient quantity of solution to achieve a final concentration of 3 mg/mL and mixed for two minutes with a Vortex-Genie mixer (Scientific Industries, Bohemia, NY). The analyte peptide mixture 1 was measured and combined in a new 1.5 mL Eppendorf® tube with de-ionized water according to the instructions from Applied Biosystems to achieve a final concentration of 250 fmol/μL and mixed for two minutes. In a separate 0.5 mL Eppendorf® tube, 0.2 mL of each of the analyte and matrix solutions were added and

www.manaraa.com

mixed for two minutes to ensure complete homogenization. The mixing of matrix and analyte solutions before deposition is referred to as concurrent deposition and is detailed in section 2.3.2.

A standard 100-well, stainless steel MALDI plate (Applied Biosystems, part number V700666) was cleaned with methanol and de-ionized water before use and dried with a stream of nitrogen. Carbon nanotube samples were not cleaned after growth or SEM investigation, but were stored in closed Gel-Pak® boxes (Hayward, CA) at all times to prevent contamination or physical damage to the nanotubes. The combined matrix/analyte solution was deposited onto the MALDI plate and carbon nanotube spots using an Eppendorf® Research® model precision pipette (0.1 µL-2.5 µL range) with a volume of 0.2 µL. Deposition was performed under an Olympus SZ61 Stereoscope (Melville, NY) with DP70 digital camera to capture time-lapse images of the drying process. Sample lighting provided by a Dolan-Jenner MI-150 fiber optic illuminator (Edmund Optics, Barrington, NJ) set for fifty percent of maximum intensity (light source is a 150 watt quartz halogen bulb with 3200K color temperature). The samples were dried by exposure to room air at an ambient temperature of 23 ºC. MALDI investigation of the samples was performed immediately after preparation to minimize any potential effects due to age, temperature, atmospheric moisture, oxidation, light, and environmental contaminants.

Sample preparation for later experiments followed similar protocol with the exception of additional dilution stages required to achieve the desired concentrations. Matrix and

www.manaraa.com

analyte solutions were diluted separately to ensure proper distribution and only combined immediately before use. Every effort was made to deposit all of the samples in a particular experiment in a uniform fashion with identical conditions and on the same day and time. Only pipette tips were changed between samples to prevent contamination of the samples and results. Solutions used for sample preparation were prepared fresh the day of the experiment.

3.4 MALDI Investigation

The mass spectrometric experiments were performed using an Applied Biosystems Voyager DE STR MALDI-TOF in positive-ion reflector mode with a 200 nano-second delayed extraction and 25 kV accelerating voltage. Ionization was achieved using a 355 nm wavelength laser with 20 Hz firing frequency. Laser intensity was adjusted to slightly above the threshold level for each sample to maintain mass resolution and minimize noise. Data was collected for 250 consecutive laser shots per spectrum.

Applied Biosystems Data Explorer (version 4) software was used for spectrum analysis. In order to calculate the signal to noise ratios, the signal value from each independent peak was divided by the root mean square (RMS) noise from the individual spectra that was calculated using the Data Explorer software. This provided a means of normalization for the spectra and allowed easier comparison and manipulation of the data. No data smoothing routines were applied. Microsoft Excel and Wavemetrics Igor Pro 4.0 software was used for statistical calculation and graphing.

www.manaraa.com

Chapter 4: Results and Discussion

4.1 Sample Concentration and Morphology

4.1.1 Standard and CNT-Enhanced Substrates

In order to compare of drying behavior of αCHCA matrix on the standard stainless steel MALDI plate and on a carbon nanotube-enhanced substrate (as described in section 3.1.2), samples were prepared by depositing 0.2 µL of a matrix/analyte solution using the technique outlined in section 3.3. The concentration of matrix in solution was 0.25 mg/mL. Time-lapse optical microscopy images (Olympus SZ61 stereo microscope) of the drying process for the samples can be seen in Figure 43 and Figure 48.

www.manaraa.com

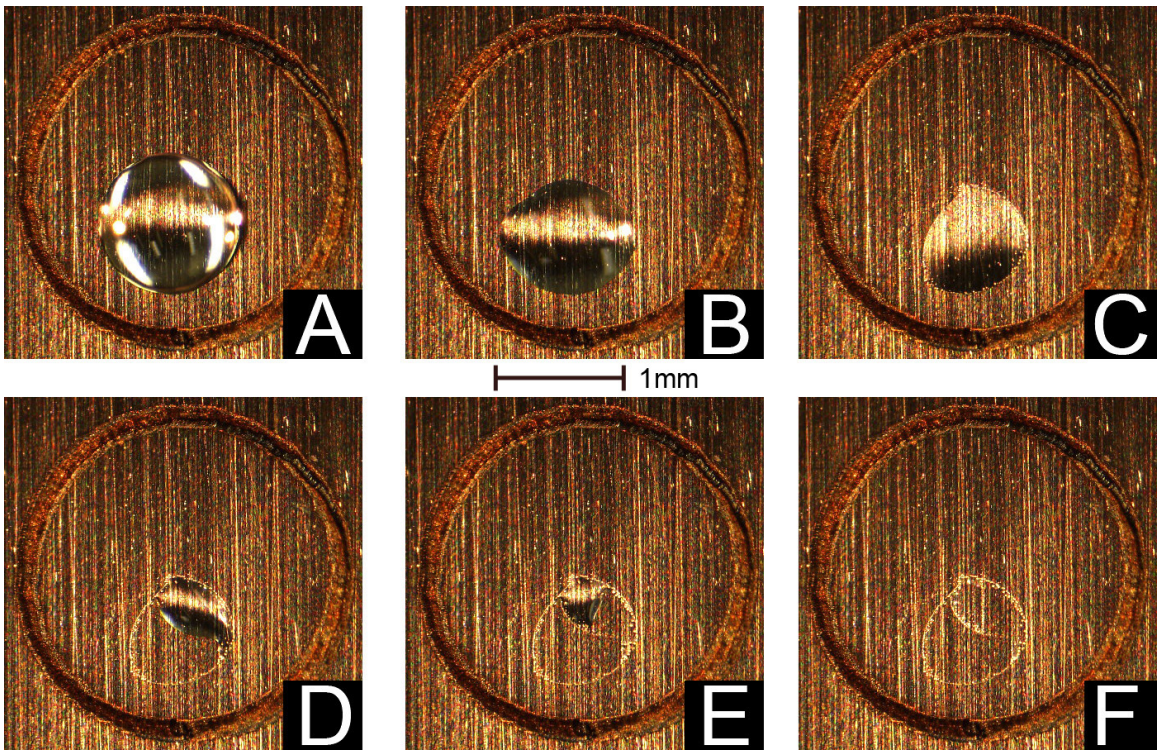

Figure 43. Time lapse images of 0.2 µL matrix/analyte solution deposited on a stainless steel MALDI plate. The large circles in the plate are laser etched from the manufacturer and are used for location and numbering purposes. Drying time was approximately three minutes at room temperature conditions.

Images A through C in Figure 43 illustrate little change in the droplet diameter during evaporation. The droplet flattened as the contact angle at the liquid/solid interface changed (Figure 44), which indicated a hydrophilic state (contact angle less than 90 degrees). Crystallization occurred at the edge of the droplet as a result of increased concentration gradients around the perimeter of the droplet (referred to as the "contact line"). The cause of this is thought to be the result of maximum evaporation flux at the edge of the droplet [86] creating a Marangoni loop [87] (see Figure 45) which transported solute from the droplet interior to the contact line. The increase in concentration led to the

www.manaraa.com

formation of matrix/analyte crystals at the contact line. The crystals formed micro-menisci [88] at the droplet contact line effectively "pinning" the line [89], which prevented the normal receding mechanism (illustrated in Figure 46). As the droplet volume continued to decrease, surface tension was sufficient to overcome capillary forces (known as "de-pinning" [87]), at which point the liquid retreated sequentially in images D and E, and deposited additional crystals at the previous edges of the liquid due to the same mechanism. The final image F displays the results of the drying process with off-center concentric rings of crystal deposits where the majority of the crystals in the solution have been deposited, leaving very few crystals in the field area between the rings.

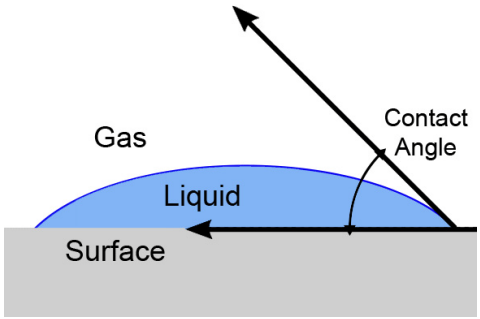

Figure 44. Illustration of contact angle measured between the vectors parallel to the solid surface and tangent to the liquid surface at the point of contact.

www.manaraa.com

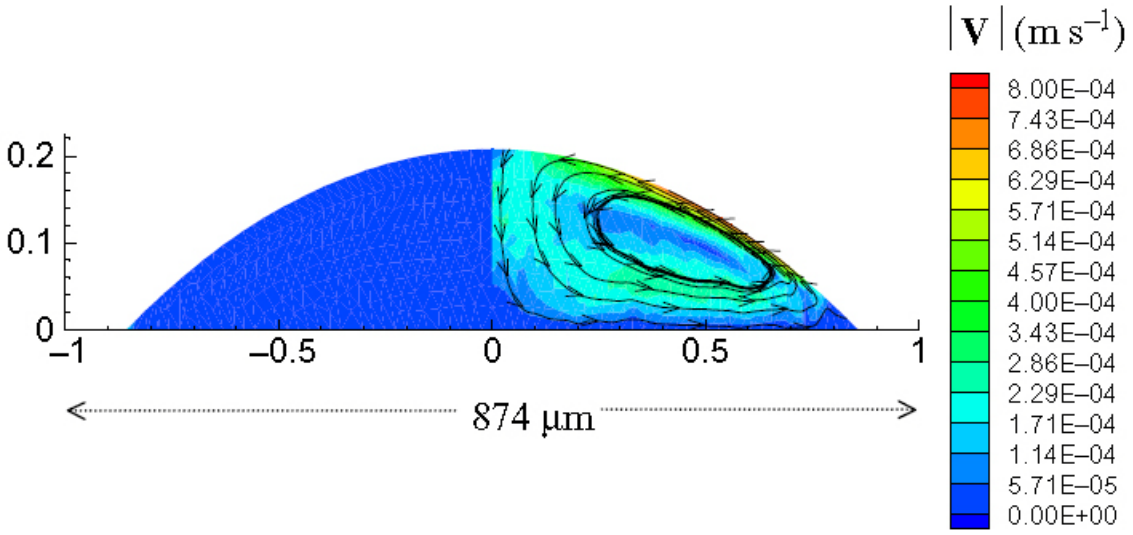

Figure 45. Simulation of Marangoni convection showing streamlines and color-coded velocity amplitude [87]. Copyright 2009 with permission from Institute of Physics.

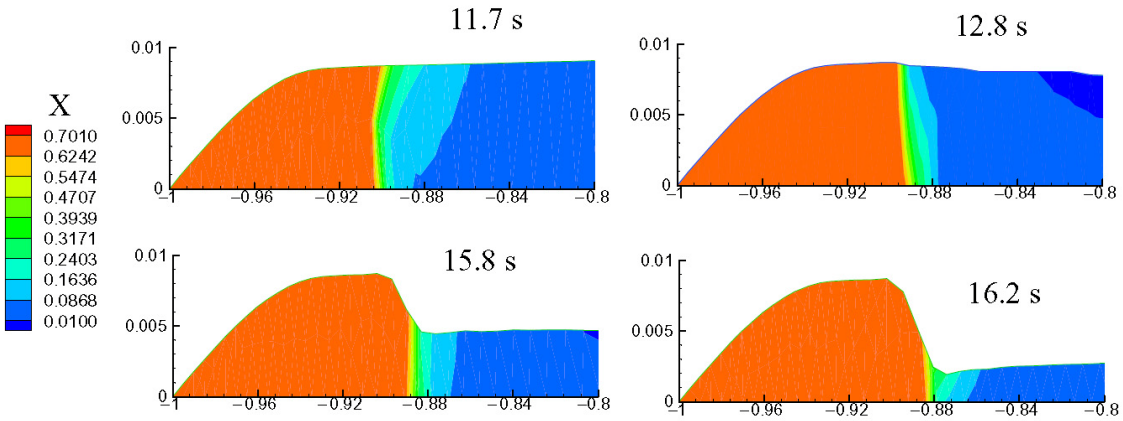

Figure 46. Simulation of ring formation at the droplet edge due to increased concentration (color-coded) and the de-pinning process over time (seconds) [87]. Copyright 2009 with permission from Institute of Physics.

www.manaraa.com

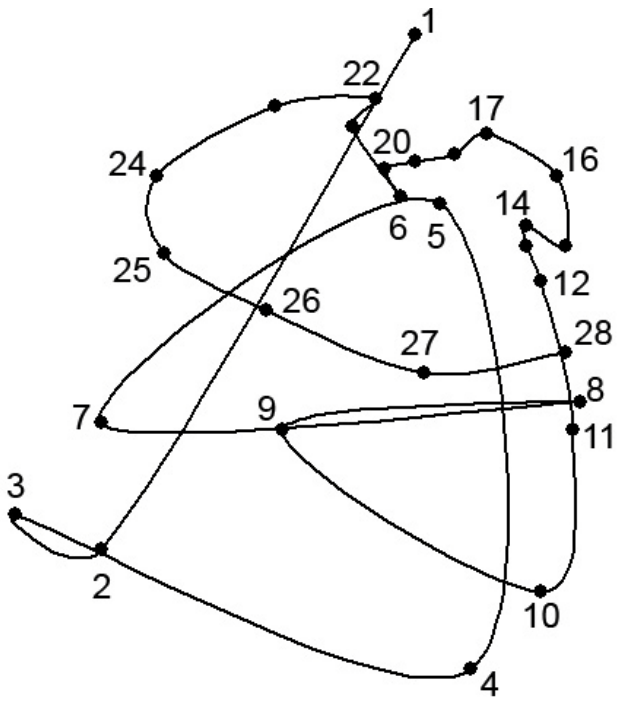

Figure 47. Path of a single matrix crystallite imaged in twenty-eight sequential frames during the droplet drying process. Particle tracking was performed with ImageJ software.

The Marangoni effect was verified during the evaporation process as small particles, assumed to be crystallites in the deposited droplet, were observed moving in a radial type pattern at high speed through the interior of the droplet. This behavior can be observed when viewing the time-lapse images of the drying process in rapid succession (video link: Marangoni convection.wmv). The path of a single particle is shown in Figure 47. The movement corresponds to the motion described by Bhardwaj et al. [87], who captured images of a fluorescent particle in solution for the purpose of position tracking during an evaporation experiment to verify simulation parameters.

www.manaraa.com

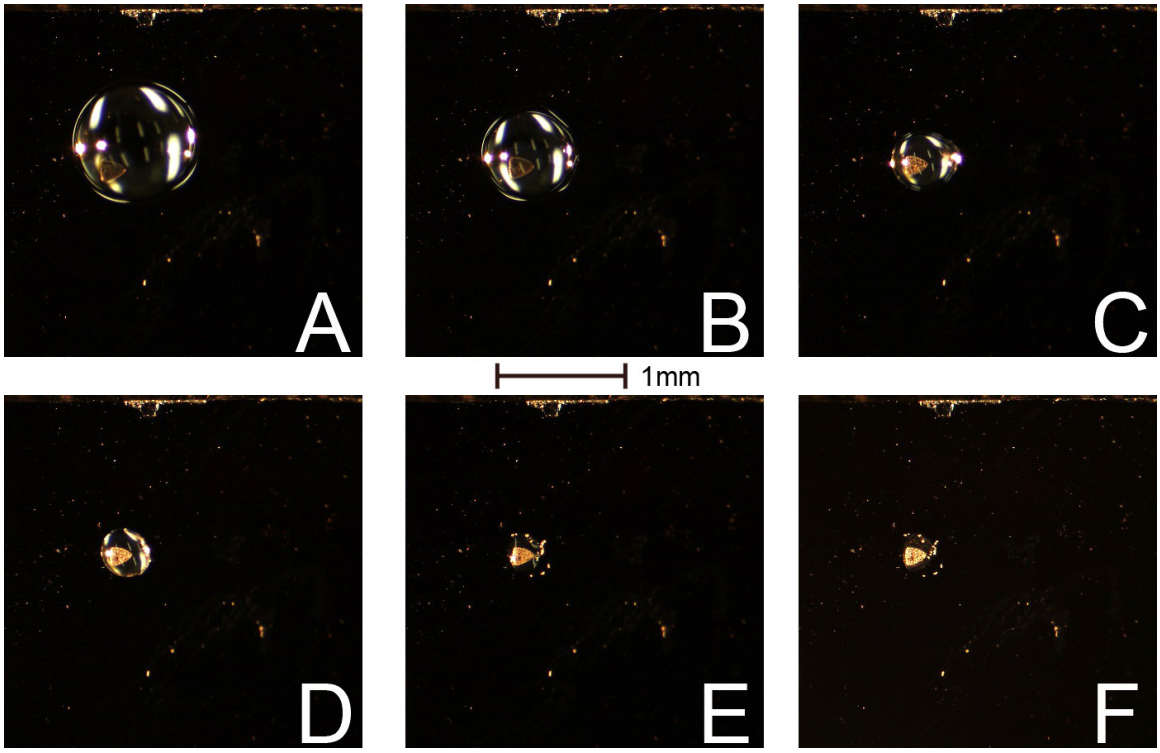

Figure 48. Time lapse images of 0.2 µL αCHCA matrix/analyte solution deposited on a silicon wafer with a patterned area of carbon nanotubes grown by PECVD. Drying time and temperature was unchanged from the deposition on the MALDI plate.

The images of the drying process on the CNT-enhanced substrate in Figure 48 show a reduction in droplet diameter during the evaporation process which corresponded to the decrease in droplet volume. (video link: Initial CNT Deposition.wmv) The droplet appeared to maintain a rounded shape and did not flatten onto the silicon surface, which indicated a hydrophobic condition (contact angle greater than 90 degrees). The initial deposition was not centered on the area occupied by the carbon nanotubes (the light gray triangle in Figure 48A). However, during evaporation, the center of the droplet shifted toward the CNT area. Additionally, crystallization did not occur in rings around the

www.manaraa.com

contact perimeter as on the MALDI plate, but rather on the carbon nanotubes first as evidenced by the color change of the CNT patch in Figure 48C from light gray to a golden color reflected by the matrix crystals. As seen in Figure 48E and F, the small volume of liquid that was present during the final stages of the deposition process preferentially resided on the carbon nanotubes until the solvent evaporated completely.

The bright areas on the liquid droplets (Figure 43 and Figure 48) are reflections from the illumination source and the fluorescent lights in the ceiling. The reflections provide a means to visually gauge the height and curvature of the droplet during evaporation and observe change in contact angle. Additionally, the droplet functioned as a lens and focused light internally onto the surface of the substrate. As a result, some areas were illuminated more strongly than others and produced the light and dark regions of the sample as seen in Figure 43A-E. The striated vertical lines on the substrate are micro-scratches on the surface of the MALDI plate from the manufacturing process. These scratches resulted in the diffuse reflection of light from the illuminator into the microscope collection lens. The silicon wafer substrate used for the carbon nanotube enhanced samples was manufactured from a single crystal of silicon and was polished to a high degree (nearly atomically flat). As a result, the silicon wafer reflected light in a more ideal manner (the law of reflection states that the reflection angle equals the incident angle measured from the "normal" or perpendicular to the wafer surface), and less light reached the collection lens of the microscope and the image of the substrate appeared dark.

www.manaraa.com

Adobe Photoshop CS3 Extended software was used to perform an image segmentation technique [90] using a color difference filter to separate the matrix crystals from the background to enhance contrast (Figure 49). Image J software (National Institute of Health) was used to measure the area of crystallization for the two samples (Figure 49).The standard sample covers an area of 0.651 mm^2 (1.104 mm diameter) while the CNT-enhanced sample is only 0.021 mm^2, with a diameter of 206 micrometers, which is on the same order as the diameter of the MALDI laser at the point of investigation.

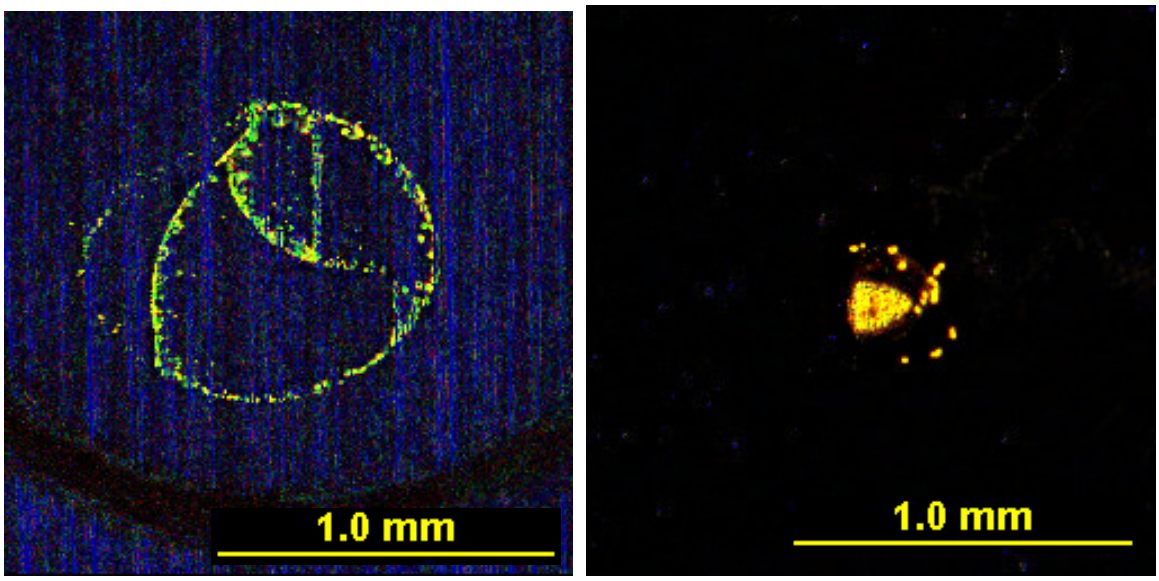

Figure 49. High magnification optical microscopy images of dried αCHCA matrix crystals on a standard MALDI plate (left) and CNT spot (right). Both images have been contrast enhanced to highlight the matrix crystals.

Scanning electron microscopy images (Hitachi S-800) of the sample deposited on the CNT-enhanced substrate can be seen in Figure 50. The standard MALDI plate was too large to fit into the loading door of the SEM, so no images were taken of that sample. The carbon nanotube enhanced sample was imaged after the initial deposition, before being

www.manaraa.com

exposed to vacuum conditions or laser irradiation in the MALDI instrument. The crystals (cubic structures) that formed on the carbon nanotubes (long, thin structures) display a high degree of homogeneity both in size and dispersion. The surrounding area in the image is the silicon substrate.

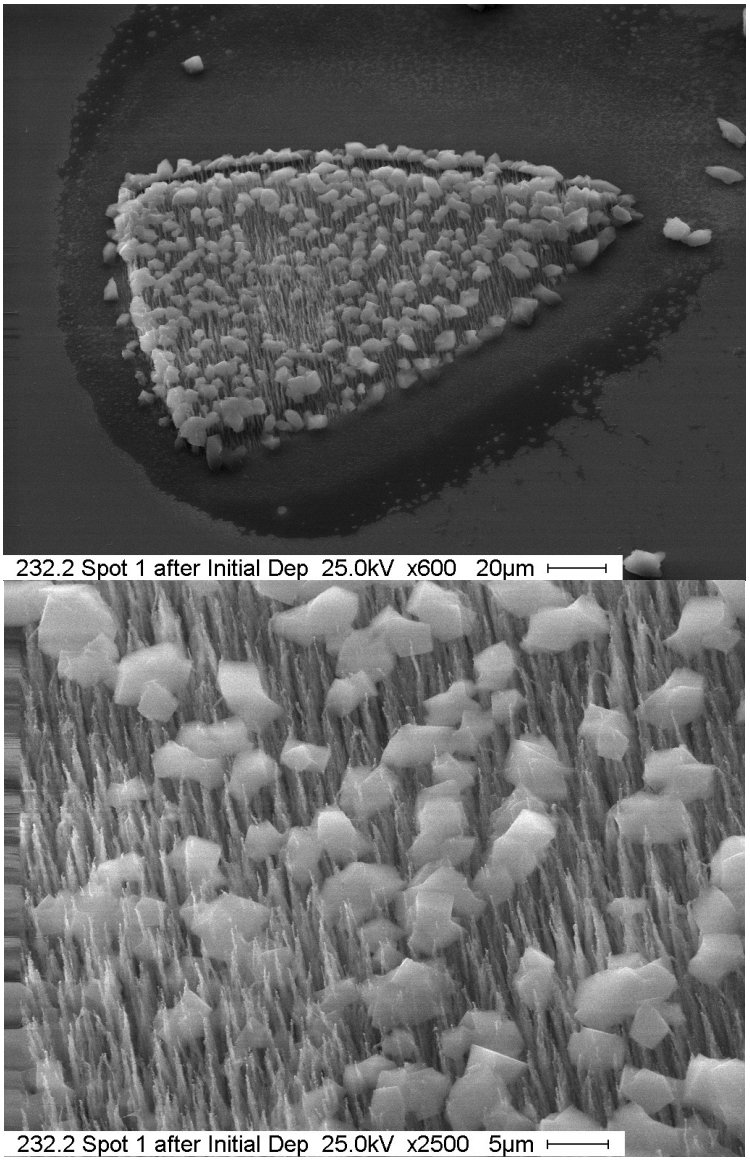

Figure 50. Scanning electron microscope (SEM) images of the αCHCA matrix crystals deposited on the carbon nanotubes. The image on the bottom is a magnified view.

www.manaraa.com

An available technology for producing concentrated samples is the AnchorChip™ plate, produced commercially through Bruker Daltonics. It uses a patterned area of hydrophilic spots as anchors for dried droplet depositions on a surrounding hydrophobic surface. The operating principle is attraction and anchoring of the deposited droplet of matrix/analyte solution on the hydrophilic surface during the evaporation and crystallization process. A schematic illustrating the evaporation process on an hydrophilic anchor and CNT-enhanced anchor is shown in Figure 51. For a conventional hydrophilic type of anchor plate, the droplet of matrix containing solution is deposited on the anchor spot (A1). As the solvents evaporate from the solution, the concentration of the solute increases (A2). Continued evaporation causes super-saturation of the solution, which triggers nucleation at the contact edge of the droplet (A3), as was illustrated with Figure 43 and Figure 46. The result is a crystal field with a large diameter relative to the MALDI laser diameter at the sample surface, in which only a few crystals are investigated concurrently (A4).

Droplet deposition of the identical matrix solution onto the carbon nanotube enhanced substrate (B1) is the same as a standard MALDI plate (B1). During initial solvent evaporation, the solute concentration remains stable as the matrix initiates crystallization on the carbon nanotubes (B2). The matrix crystals precipitate and remove solute from the evaporating droplet, preventing crystal formation on the surrounding area (B3). In the resulting deposit, the majority of the crystals are grown on the carbon nanotubes. The MALDI laser (B4) is able to simultaneously interrogate a greater percentage of the

www.manaraa.com

deposited matrix/analyte crystals, which can produce an increase in collected signal strength.

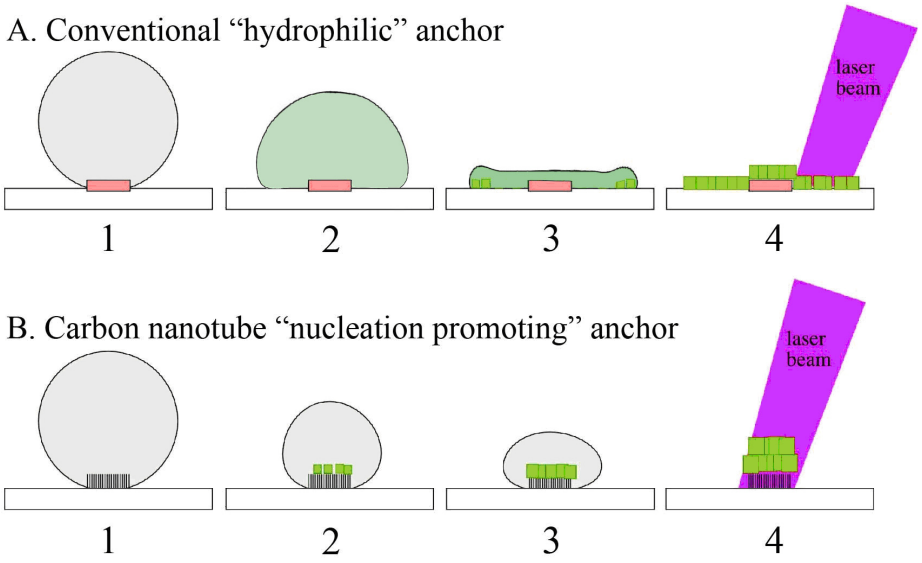

Figure 51. An illustration depicting the crystallization behavior of matrix solution during sample preparation on the two types of substrates.

While hydrophilic anchors come in a variety of sizes, the manufacturer recommends that matrix αCHCA (non-aqueous) be used with the 600 µm diameter anchor spots [91]. Anchor spots with diameters as low as 200 µm are available for aqueous-based matricies, however the product literature states that size anchor is not able to reliably attract droplets of micro-liter volume. The carbon nanotube enhanced anchor demonstrated the ability to concentrate solutions of matrix αCHCA to final dried droplet diameters below 200 µm, as seen in Figure 48.

Another technology for producing small diameter dried droplets for MALDI is deposition by piezoelectric pipette. The dried droplets produced by this method were

www.manaraa.com

approximately 100 µm in diameter and the entire droplet could be simultaneously interrogated by the MALDI laser [50]. This is comparable to deposition on patterned carbon nanotubes. However, that experiment used an aqueous matrix rather than non-aqueous αCHCA, preventing direct comparison of MALDI performance. The technique appears promising due to the ability to precisely control deposition location and volume, with the additional benefit of fast evaporation time (less than 20 seconds per spot). Possible difficulties not discussed in the publication include contamination prevention when changing deposition solutions, which is preventable during manual deposition with traditional disposable-tip pipettes. Additionally the minimum sample volume required by the system may be prohibitive for preparing solutions with expensive or limited analyte.

The cause of early nucleation of matrix crystals on the carbon nanotubes can be hypothesized to be the result of interaction between the hexagonal carbon ring in the matrix molecule αCHCA and the carbon atoms on the surface of the nanotube, also in a hexagonal arrangement (Figure 52). The results of π-bond stacking between aromatic compounds and carbon nanotubes has been published by research groups studying interactions between pyrenyl groups and CNT [92], benzyl groups and CNT [93], DNA and CNT [94],and aromatic peptides and CNT [95-99] (Figure 53).

www.manaraa.com

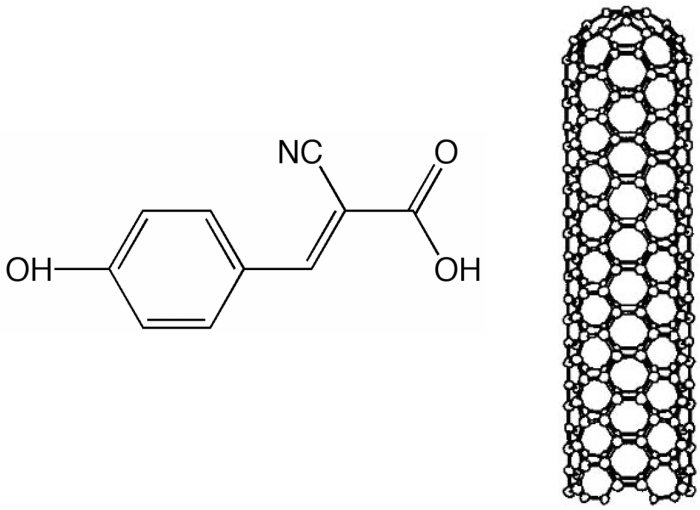

Figure 52. Schematic of αCHCA molecule and a carbon nanotube to illustrate hexagonal carbon structure.

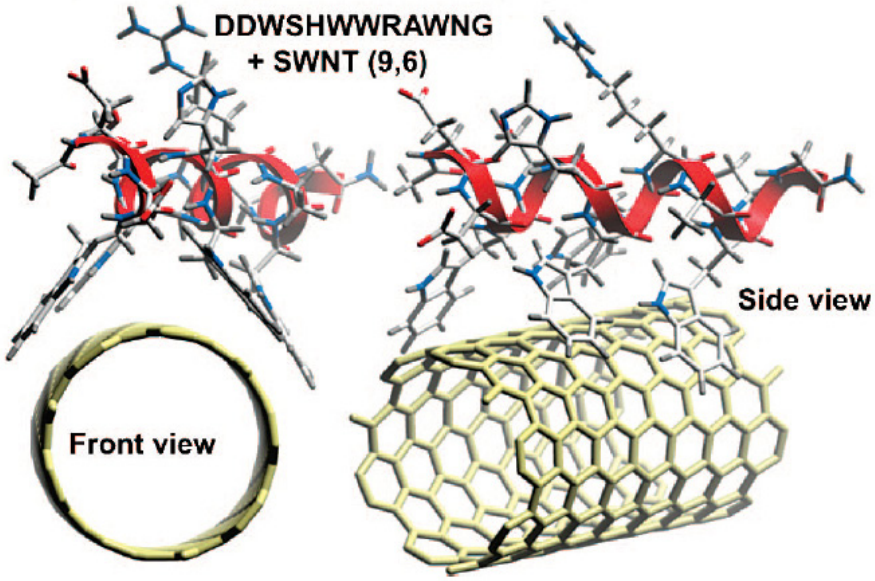

Figure 53. Schematic of CNT-peptide interaction [99] showing docking of aromatic amino acid tryptophan onto the carbon nanotube. Copyright 2009 with permission from American Chemical Society.

www.manaraa.com

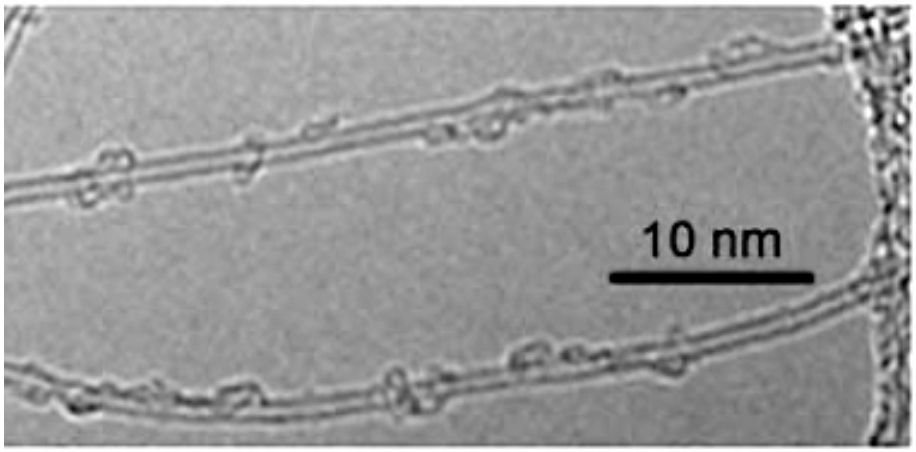

Figure 54. Transmission electron microscope image of protein coated single wall CNT [100]. Copyright 2009 with permission from John Wiley and Sons.

The π-bond is thought to be a contributing force in aromatic compound adsorption on carbon nanotubes. Hydrogen and covalent bonds may also be present between molecular components (OH groups) and CNT surfaces [96]. The adsorption of αCHCA onto the nanotube surface could initiate the crystallization of matrix out of solution and account for the phenomena observed during the droplet drying process and the inter-nanotube crystal formation in Figure 50. The rapid rate of crystallization on the carbon nanotubes could be the result of Marangoni convection which would supply additional matrix molecules to the localized area around the CNT's as the crystallization process removes matrix from the solution. In addition, the carbon nanotubes large surface area provides substantial capacity for adsorption and crystallization.

Further experiments were performed to document and validate the mechanism for interaction between the matrix molecules and the carbon nanotubes. The first experiment was designed to verify that the CNT's were responsible for the lateral concentration and

www.manaraa.com

early nucleation by deposition of the αCHCA matrix solution on both a bare silicon wafer and a wafer that had a patterned area of nickel (catalyst for CNT growth via PECVD) that was created by e-beam deposition through the same mask as described in section 3.1.1.

The deposited droplet consisted of the same solution and volume as those used to prepare the samples shown in Figure 43 and Figure 48. The drying process on the bare silicon substrate was similar to that observed on the MALDI plate in that matrix crystals formed on the surface primarily at the contact edge between the substrate and the droplet (Figure 55, video link: Si wafer.wmv). Pinning was observed during evaporation and ring patterns were formed as the contact line retreated. During the final stages of evaporation, the droplet did not display any distinguishable preference or adherence to any particle or crystallite. The final deposit was larger than the equivalent on the MALDI plate with an area of 0.759 mm^2 and a maximum diameter of 1.057 mm.

The deposition on the substrate with a patterned nickel area (visible as a triangular gray patch in Figure 56) demonstrated similar drying patterns to both the bare silicon substrate and the MALDI plate (video link: Nickel dots.wmv). Crystallization occurred in rings during evaporation (Figure 56D). The observed evaporation was in the direction of the nickel pattern, however unlike the carbon nanotube-enhanced substrate, no crystallization occurred directly on the nickel. The final dried droplet was slightly smaller than that on the MALDI plate. The area was 0.626 mm^2 with a 0.855 mm diameter.

www.manaraa.com

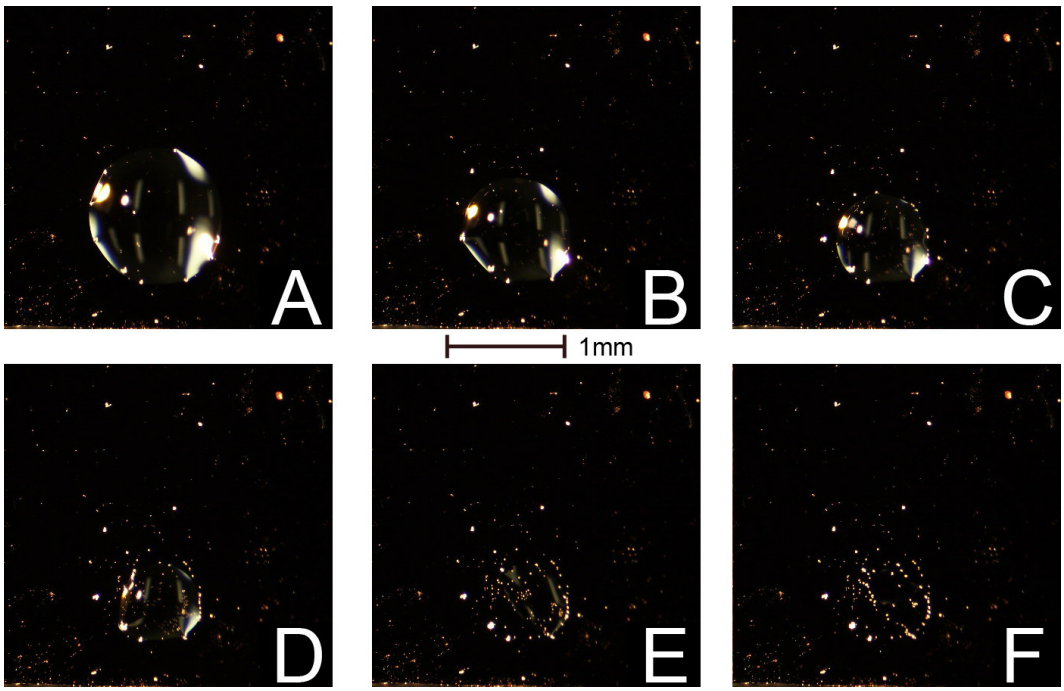

Figure 55. Time lapse images of 0.2 µL αCHCA matrix solution deposited on a bare silicon wafer without nickel catalyst or CNT. Crystal ring formation and subsequent pinning visible in frames C and D.

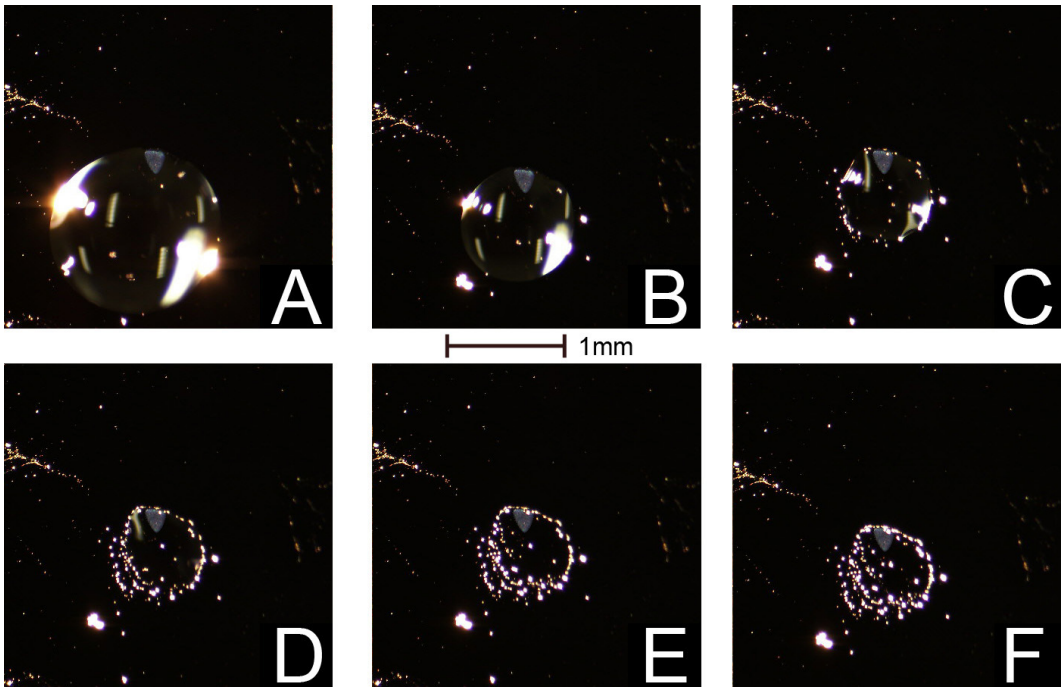

Figure 56. Time lapse images of 0.2 µL matrix solution deposited on a silicon wafer with a patterned area of nickel catalyst without carbon nanotube growth.

www.manaraa.com

The results of these experiments indicate that for αCHCA, the enhanced nucleation behavior was due to matrix interaction with the carbon nanotubes and not attributed to the presence of nickel or the surrounding silicon substrate.

The next experiment to further investigate CNT/matrix interaction was designed to test the crystallization behavior of aromatic molecules with attached hydroxyl and carboxyl groups (Figure 57) to determine if these groups interacted with the carbon nanotubes. Samples were prepared using molecules that had only hydroxyl components (Catechol), only carboxyl components (Benzoic acid), and both components (Salicylic acid). Phenol, a molecule consisting of an aromatic ring with a single hydroxyl group, would have been preferred in place of Catechol, but was not used due to its toxic nature. To test the interaction of hydroxyl terminated, non-aromatic molecules with carbon nanotubes, samples were also prepared using 1,10-Decanediol (Figure 58).

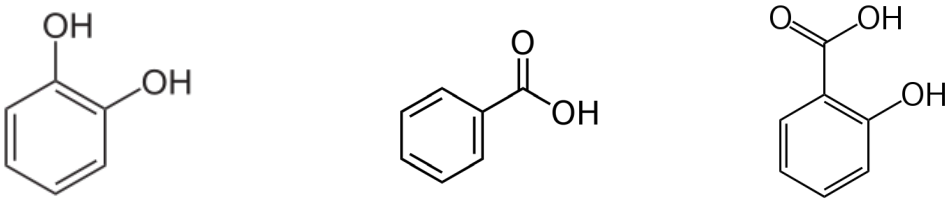

Figure 57. Schematic diagrams of Catechol (left), Benzoic acid (center), and Salicylic acid (right).

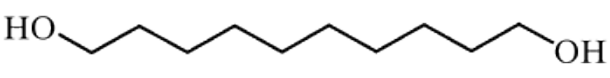

Figure 58. Schematic diagram of 1,10-Decanediol.

www.manaraa.com

Individual solutions were made from each of the components with a solvent of 1:1 volumetric ratio acetonitrile to de-ionized water. The solute concentrations were adjusted using the values in Table 2 to keep the molarity of each solution consistent with that of the initial αCHCA solution. Deposition was performed on both the standard MALDI plate (Figure 59) and CNT-enhanced substrates using the technique from section 3.3.

Table 2. Calculations for concentrations used to prepare solutions with equivalent molarity.

Solute	Moles	Molecular Mass	Concentration	pH
αCHCA	1.32x10-6 mol	189.17 g/mol	0.25 mg/mL	2.75
Catechol	1.32x10-6 mol	110.1 g/mol	0.146 mg/mL	4.5
Benzoic acid	1.32x10-6 mol	122.12 g/mol	0.161 mg/mL	3.6
Salicylic acid	1.32x10-6 mol	138.12 g/mol	0.183 mg/mL	2.8
Decanediol	1.32x10-6 mol	174.28 g/mol	0.23 mg/mL	7.6

www.manaraa.com

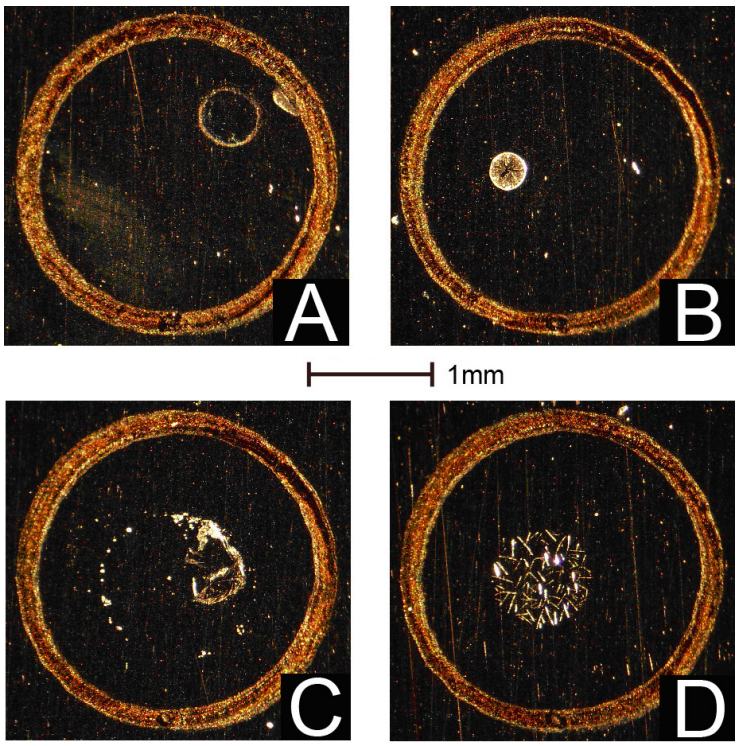

Figure 59. Dried droplet samples deposited on a standard MALDI plate from 0.2 µL of solution. The images are labeled Catechol (A), Benzoic acid (B), Salicylic acid (C), and Decanediol (D).

The depositions on the MALDI plate resulted in ring structures for all aromatic solutions. The catechol sample had a thin solid ring with very few crystals in the interior. The sample made with benzoic acid resulted in a smaller, dense ring with a large number of central crystals. The salicylic acid resulted in a deposit with similar morphology to an αCHCA deposit, as crystallites formed at the edge of the contact line as the solvent evaporated. The decanediol sample produced thin, straight crystals that did not form a ring structure at the contact edge of the droplet.

www.manaraa.com

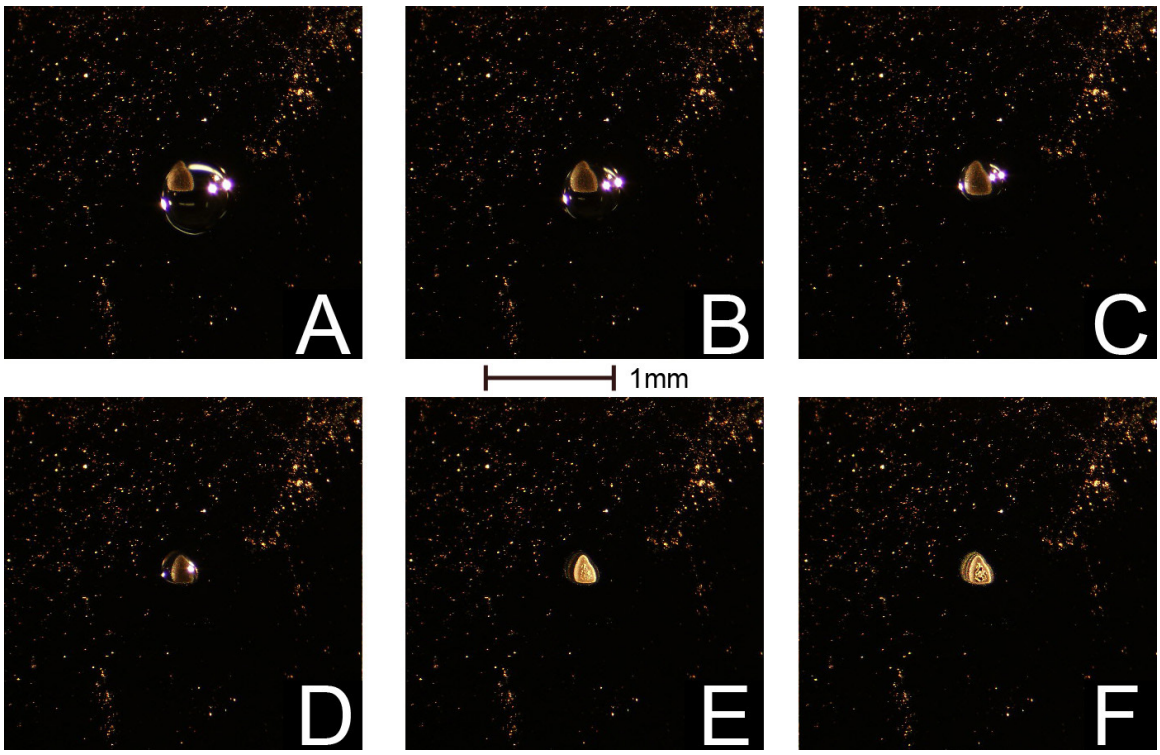

Figure 60. Time lapse images of 0.2 µL Catechol solution deposited on a silicon wafer with a patterned area of carbon nanotubes grown by PECVD.

The drying behavior of the catechol solution (Figure 60, video link: Catechol.wmv) was similar to αCHCA. As evaporation progressed, crystallization did not occur on any surrounding area (A-D). At the final stages, the carbon nanotubes became coated with catechol crystals (E) and a few excess crystals formed on the silicon surface (F).

The benzoic acid droplet dried differently than both αCHCA and catechol (video link: Benzoic Acid.wmv). The solution deformed during drying and became elliptical, concentrating directly onto the CNT area (Figure 61 C & D). The final crystallization occurred in a ring around the perimeter of the nanotubes (E), then spread inwards forming long, thin crystals that encrusted the deposition area (F). This behavior is similar

www.manaraa.com

to the drying pattern observed when matrix 3-hydroxy picolinic acid (HPA) was deposited on the carbon nanotube-enhanced substrate (Figure 62).

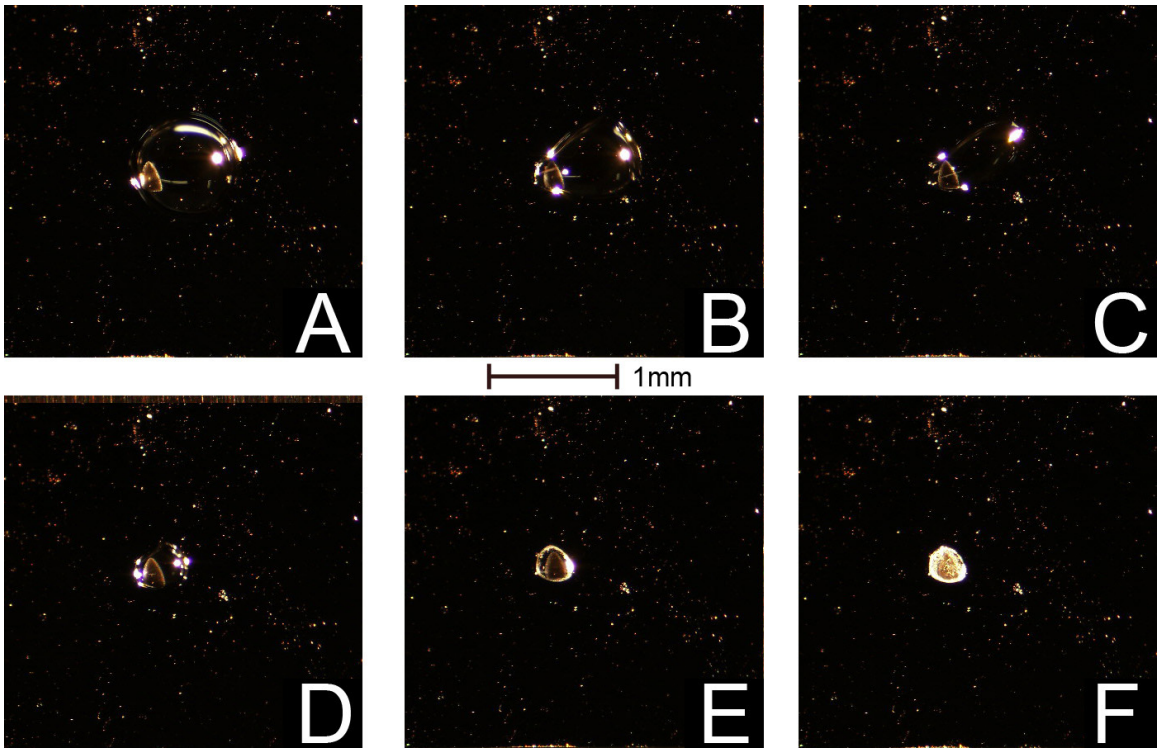

Figure 61. Time lapse images of 0.2 µL Benzoic acid solution deposited on a silicon wafer with a patterned area of carbon nanotubes grown by PECVD.

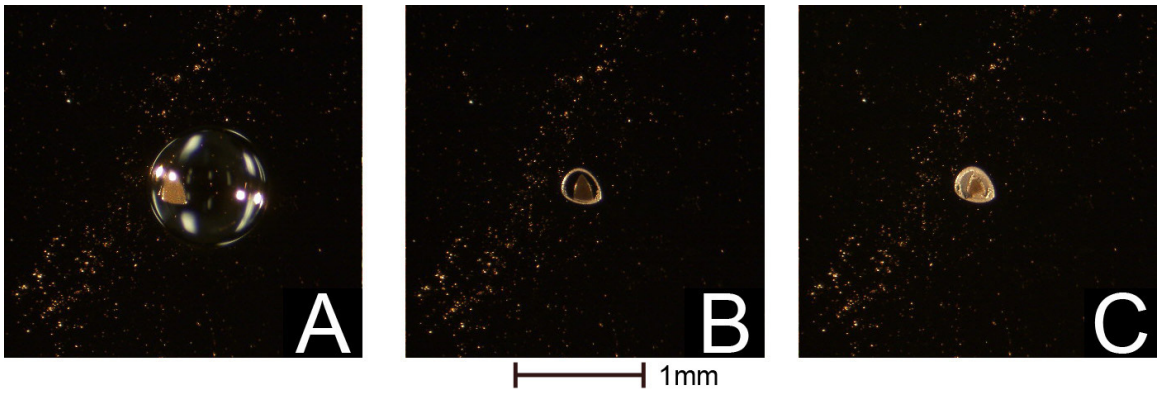

Figure 62. Time lapse drying images of 3-HPA solution deposited on carbon nanotubes. The sample is for reference only and not included in this experiment.

www.manaraa.com

The evaporation of the salicylic acid solution progressed in a similar fashion to the catechol (video link: Salicylic Acid.wmv). The droplet maintained a round shape and symmetrically reduced in diameter (Figure 63 A-D). Crystals formed in the center of the CNT area and progressed outward, slightly exceeding the diameter of the patterned region.

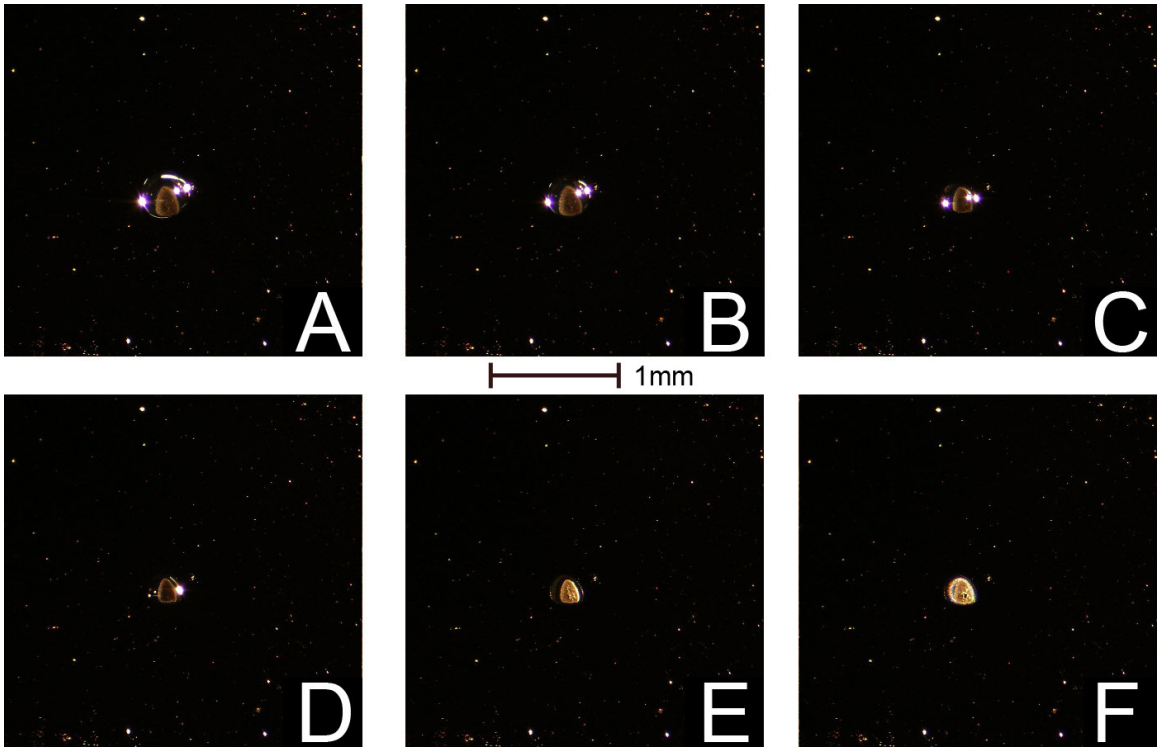

Figure 63. Time lapse images of 0.2 µL Salicylic acid solution deposited on a silicon wafer with a patterned area of carbon nanotubes grown by PECVD.

The sample prepared using decanediol crystallized during solvent evaporation, starting with the contact edge of the droplet and formed straight, thin crystals that developed equally across the sample surface, with no apparent interaction with the carbon nanotubes (Figure 64). These crystals appeared to match the description given by Nakamura et al.

www.manaraa.com

[101] in which the molecules form a “herring-bone” type structure perpendicular to the longest axis of the molecule due to hydrogen bonding of the terminal hydroxyl groups.

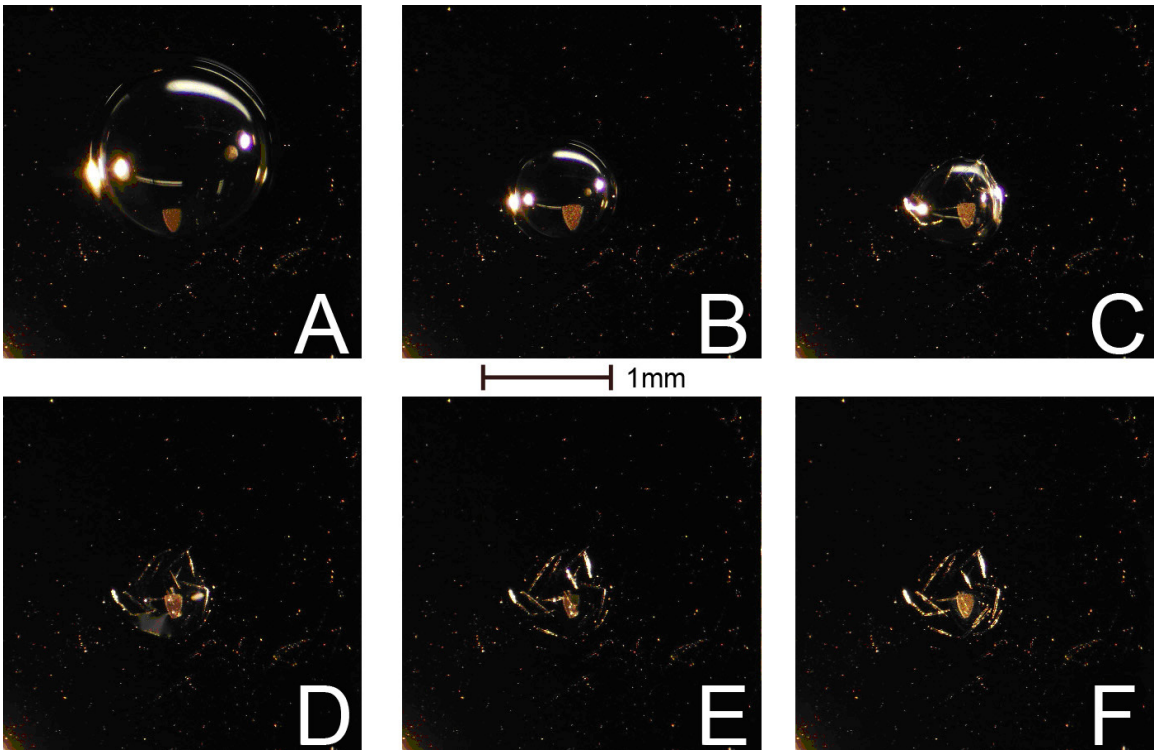

Figure 64. Time lapse images of 0.2 µL Decanediol solution deposited on a silicon wafer with a patterned area of carbon nanotubes grown by PECVD.

Image J software was used to measure the area and diameter of each of the deposited spots. For direct comparison, the data (averaged with standard deviation values) is presented in Table 3 and grouped by solute molecule and substrate type. As a reference, the typical carbon nanotube pattern has an area of approximately 0.02 mm^2 and a maximum diameter of 0.2 mm.

www.manaraa.com

Of the molecules used in the experiment, salicylic acid was the best analog to αCHCA. The dried droplet areas on both the MALDI plate and the patterned carbon nanotubes were comparable. Additionally, the molecular structures are similar with an aromatic carbon ring with attached hydroxyl and carboxyl groups, and equivalent pH values in solution (2.75 average for αCHCA to 2.8 average for salicylic acid).

Table 3. Metrics of dried droplet samples organized by substrate.

Solute	Substrate	Average Area (mm^2) with std. dev. (σ)	Average Diameter (mm) with std. dev. (σ)
αCHCA	MALDI plate	0.591 (0.084 σ)	1.007 (0.137 σ)
αCHCA	Bare Silicon	0.669 (0.126 σ)	0.991 (0.093 σ)
αCHCA	Patterned Ni	0.960 (0.473 σ)	1.105 (0.354 σ)
Catechol	MALDI plate	0.278 (0.123 σ)	0.630 (0.105 σ)
Benzoic acid	MALDI plate	0.154 (0.042 σ)	0.459 (0.060 σ)
Salicylic acid	MALDI plate	0.577 (0.161 σ)	0.948 (0.179 σ)
Decanediol	MALDI plate	0.592 (0.138 σ)	0.918 (0.129 σ)
αCHCA	Patterned CNT	0.034 (0.018 σ)	0.263 (0.080 σ)
Catechol	Patterned CNT	0.064 (0.013 σ)	0.328 (0.041 σ)
Benzoic acid	Patterned CNT	0.066 (0.008 σ)	0.331 (0.020 σ)
Salicylic acid	Patterned CNT	0.046 (0.007 σ)	0.267 (0.002 σ)
Decanediol	Patterned CNT	0.287 (0.128 σ)	0.690 (0.153 σ)

Table 4. Reduction in sample area as a result of deposition on CNT substrate compared to standard MALDI plate.

Solute	Average Area Reduction for Deposition on CNT Substrate
αCHCA	94.25%
Catechol	76.98%
Benzoic acid	57.14%
Salicylic acid	92.03%
Decanediol	51.52%

www.manaraa.com

The mechanism that contributes to the enhanced nucleation on the CNTs was thought to be π-bond stacking between aromatic compounds and the outer surface of carbon nanotubes. The results show that the presence of hydroxyl or carboxyl groups on the solute molecule can affect the crystallization behavior resulting in a marked difference in crystal morphology, an indication that the mechanism can be more complex than previously proposed. Additionally, π-bonds are relatively short range resulting in a low probability for primary molecular attraction.

As indicated previously in section 2.1.1, the carbon nanotubes grown using the PE-CVD technique possess multiple shells, with at least one shell displaying metallic properties, thereby dominating the conductive properties of the nanotube. Granger et al. [102] predicted that metallic carbon nanotubes can form extended image states due to external electron polarization of the CNT via image charge interaction with the electrons in the nanotube. The combined effect of these states forms a cylinder-shaped region surrounding the metallic carbon nanotube and is referred to as "tubular image states" (Figure 65). The calculation of effective potential as a function of distance (Figure 66), indicates a possibility for attraction of charges and charged molecules at a longer range than that of π-bonds.

www.manaraa.com

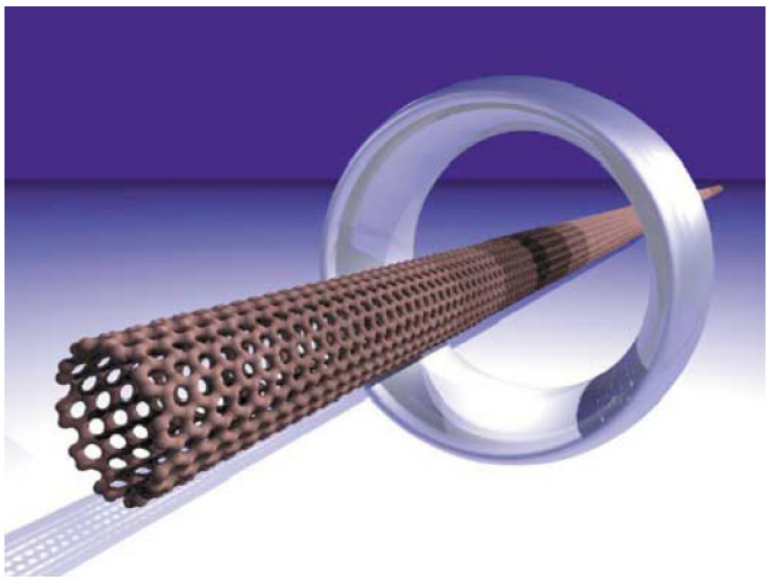

Figure 65. Tubular image state around a metallic CNT [102]. Copyright 2002 with permission from American Physical Society.

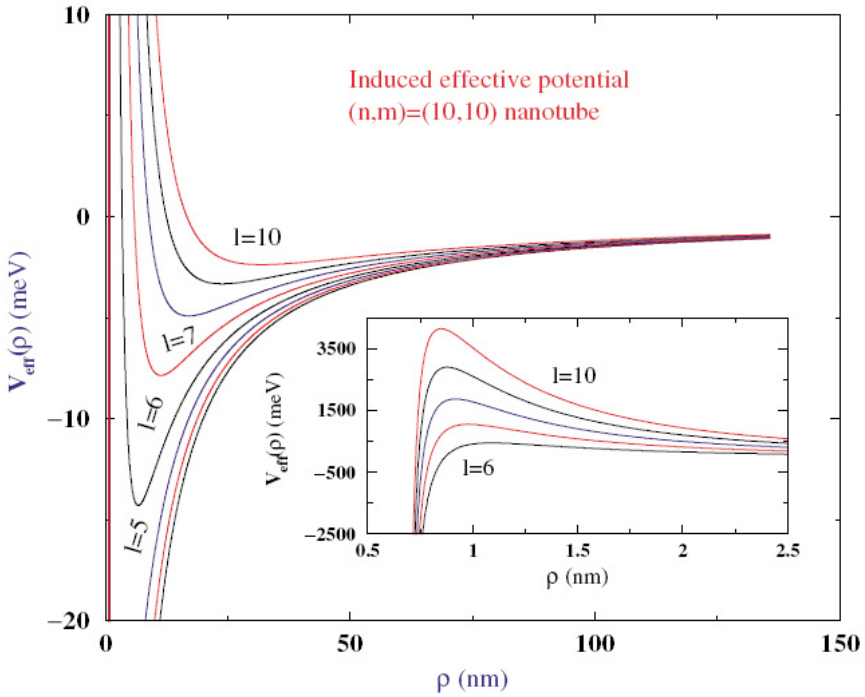

Figure 66. Effective potential (V_{eff}) for tubular image states around metallic CNTs as a function of distance (ρ) and angular momenta (*l*). The inset shows short range potentials near the carbon nanotube surface [102]. Copyright 2002 with permission from American Physical Society.

www.manaraa.com

When dissolved in a solution of acetonitrile and de-ionized water to matching concentrations, the molecules αCHCA and Salicylic acid indicated similar, highly acidic pH values, which suggested a high probability that the dissolved molecules carry a charge. The quantity of charged molecules in combination with the tubular image states surrounding the carbon nanotubes could provide a mechanism for long range attraction, resulting in the enhanced preferential crystallization that was displayed during sample preparation (Figure 67).

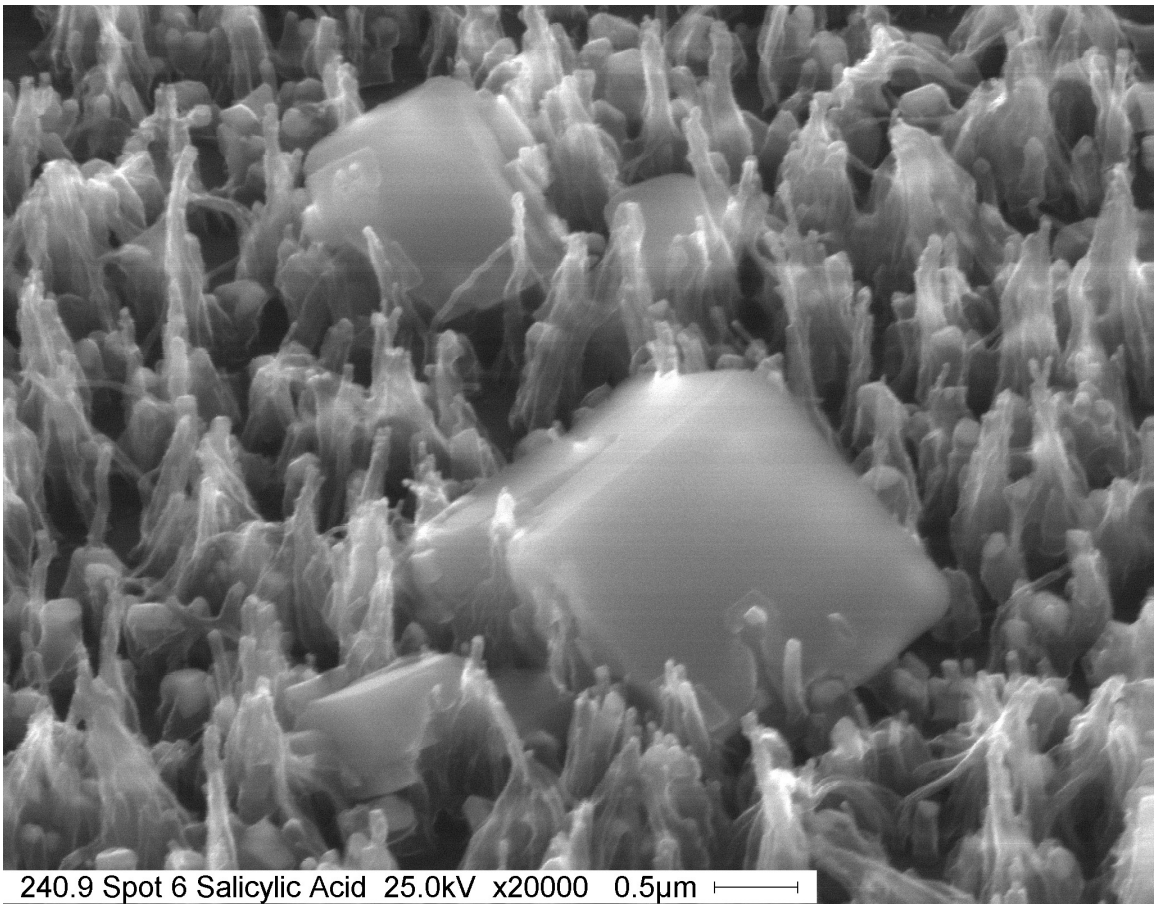

Figure 67. SEM image of Salicylic acid deposited on CNT's demonstrating crystallization around the carbon nanotubes. The nickel catalyst-containing nanotube tips are seen protruding from the crystal, indicating preferential interection with the CNT sidewall.

www.manaraa.com

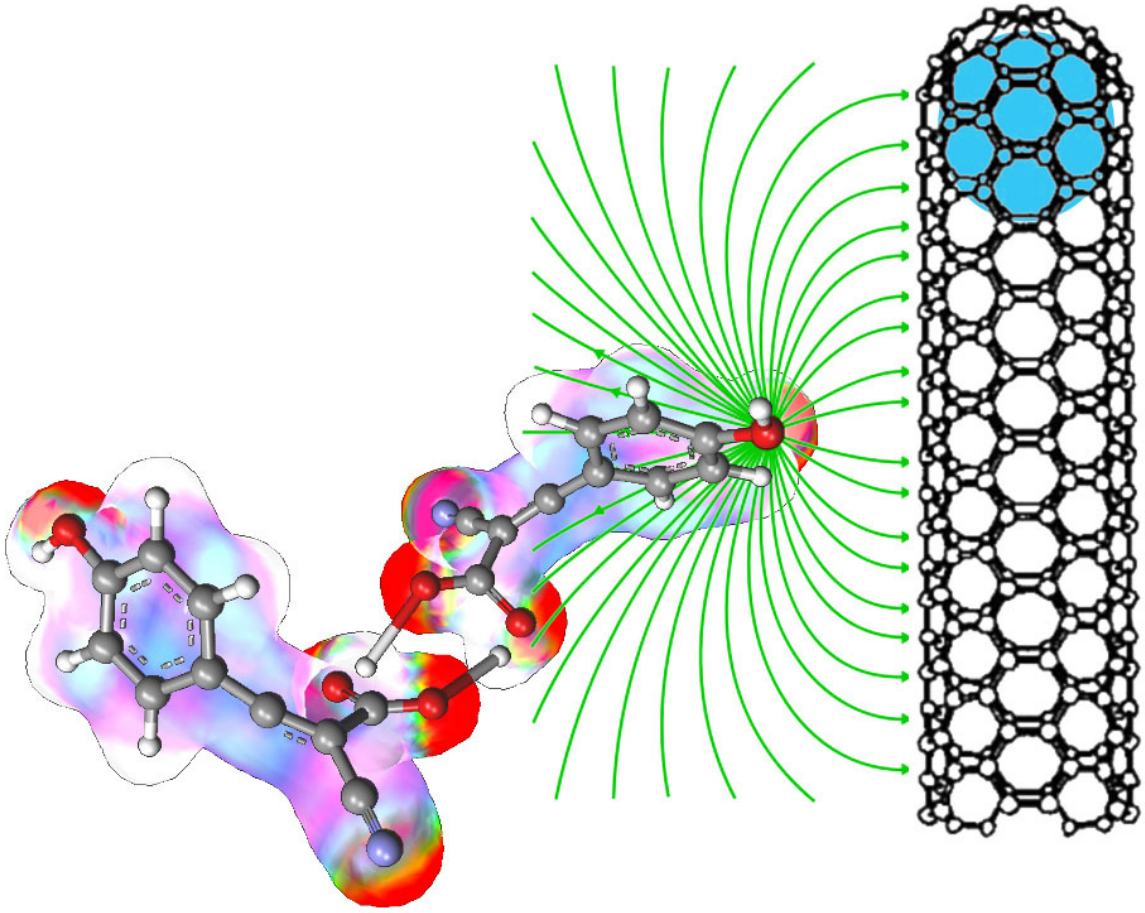

Figure 68. Illustration of possible dipole attraction/interaction with a carbon nanotube. Two αCHCA molecules (left) are shown with dimerization of the carboxyl groups. Polar charge may produce an image charge in the CNT (right), either along the sidewall or the Nickel catalyst particle at the tip (light blue). The multicolor region surrounding matrix molecules represents electrostatic potential, the red is negative and the white is positive, which was simulated using ArgusLab 4.0.1 Molecular Modeling and Drug Docking software [105]. The electric field lines (green) are an approximation based on those of a charge near a flat conducting surface.

www.manaraa.com

Future experiments should be performed to verify the conditions for the dominant attraction mechanism to account for matrix dimerization [103, 104], molecular dipoles, and induced image charges (Figure 68). See Section 5.2 for more details concerning future work.

Earlier work by Schuerenberg et al. [72], (discussed in section 2.3.4.1.), involved a technology for lateral sample concentration that consisted of a thin film of gold as the patterned hydrophilic anchor with a surrounding hydrophobic field of Teflon®. The solutions of matrix αCHCA crystallized onto the spots with a few interesting effects reported. Some droplets left the gold spot and crystallized on the surrounding Teflon®, which could suggest forces that could overcome potential hydrophilic attraction. Additionally, droplets that were intentionally deposited on the Teflon® field, not in contact with any gold anchors, also displayed lateral concentration, which could indicate that the final dried droplet diameter may be dependent on the initial solution concentration and solvent composition rather than the diameter of the anchor spot. As shown in Figure 55 and Figure 56 of this work, deposition of matrix solution on the silicon surface surrounding patterned CNT's does not display any form of lateral concentration, which confirms the effect of the CNT's on the drying process.

www.manaraa.com

4.1.2 Concentration Dependent Drying Behavior for Matrix αCHCA

To further investigate the sample concentrating properties of CNT anchor spots, experiments were conducted where the concentration was varied. Solutions were prepared according to the procedure outlined in section 3.3, with matrix concentration varied over three orders of magnitude from 0.006 mg/mL to 6 mg/mL. Matrix concentrations above 6 mg/mL displayed insolubility and were not used for this experiment. All matrix solutions were prepared freshly and independently of each other in order to reduce possibility of concentration error.

The samples were prepared by manually depositing 0.2 µL of solution from pipette to new carbon nanotube enhanced substrates (same parameters as previous experiment). The droplets were allowed to dry in ambient conditions (room temperature 23ºC), and time-lapse images were captured using the optical microscope described previously. Images of the samples after completed crystallization are shown in Figure 69. Using ImageJ software, crystal size analysis was performed on each of the images and the results for each concentration range are listed in Table 5. Histograms of crystal sizes for each deposition can be found in Appendix D.

www.manaraa.com

Table 5. Average crystal size of dried droplet samples grouped by concentration.

Matrix Concentration	Average Crystal Size
0.006 - 0.03 mg/mL	40 μm^2
0.1 - 0.25 mg/mL	50-100 μm^2
3 - 6 mg/mL	500-1000 μm^2

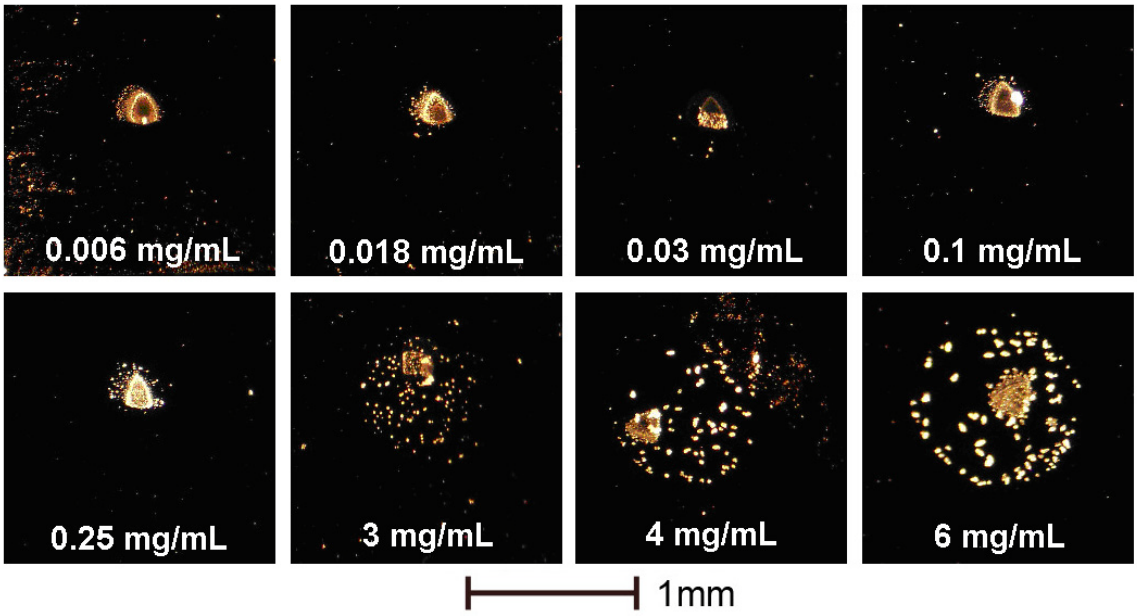

Figure 69. A series of optical microscope images that show the crystallization behavior of the matrix solution on the CNT enhanced substrate. The concentration of the solution was varied over three orders of magnitude.

Further image analysis using the ImageJ software provided crystal count data for the entire image and for a select area defined by the location of the CNT field. The data provided a means for calculation of the crystal percentage formed on the carbon

www.manaraa.com

nanotubes relative to the surrounding area. An analysis of the concentration series images resulted in a range of data that was plotted using Wavemetrics Igor Pro software (Figure 70). The percentage of matrix crystals that formed on the carbon nanotubes was very high for low matrix concentrations (94.6% for 0.006 mg/mL) as a result of droplet diameter reduction during evaporation on a hydrophobic surface, as outlined in section 4.1.1.

The midrange concentrations still performed well on the CNT enhanced substrate averaging 83.5% of all crystals on CNT's. Crystallization occurred on the carbon nanotubes first (less than 30 seconds after deposition) and droplet diameter reduction continued until the matrix concentration reached supersaturation and crystals precipitated on the surrounding silicon substrate. The crystals effectively pinned the contact line and prevented diameter reduction until increasing surface tension from continued evaporation was sufficient to overcome capillary force.

At very high matrix concentrations, matrix crystals covered the CNT field first (approximately 30 seconds), then precipitated onto the surrounding silicon wafer due to supersaturation of matrix in solution. The result was a low percentage (35%) of the total crystals deposited on the carbon nanotube area.

www.manaraa.com

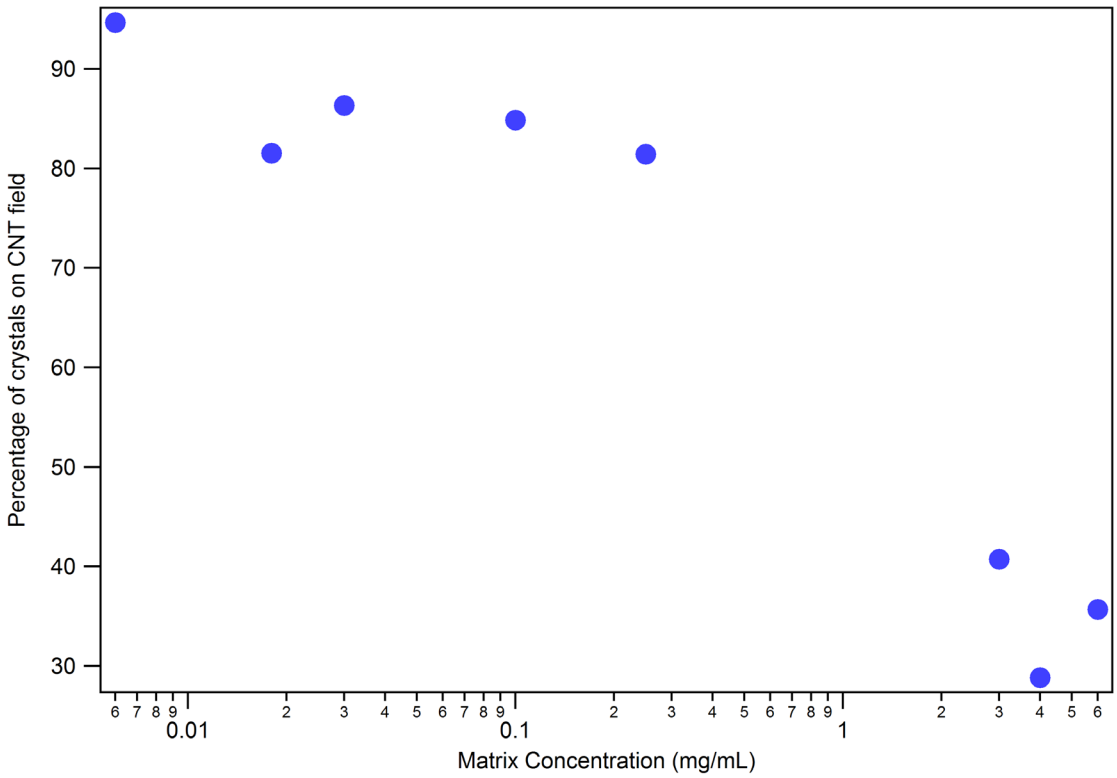

Figure 70. Graph of crystallization percentage on CNT field for varying matrix solution concentrations.

4.2 MALDI Measurements

4.2.1 Deposition Volume Optimization

An initial experiment was conducted to optimize the deposition volume for best MALDI signal, to be used as the standard volume for future experiments. The deposition volume was varied while the solution concentration and ratio was held constant. A solution was prepared from 5 mg/mL matrix (αCHCA) mixed 1:1 with 250 fmol/µL of analyte solution peptide mixture 1 detailed previously (section 3.3). The values used were

www.manaraa.com

recommended by the operating instructions (Applied Biosystems) included with the calibration mixture. When mixed in a 1:1 ratio, the concentrations correspond to 13.2 nmol/μL of matrix to 125 fmol/μL of analyte ($1.32x10^{-8}$ mol/μL and $1.25x10^{-13}$ mol/μL, respectively) or a matrix to analyte molar ratio of approximately 106,000:1. Spotting volumes recommended by Applied Biosystems were 0.5 and 1 μL. Aliquots of solution with volumes from 1 μL to 0.1 μL were deposited on a standard MALDI plate via pipette and allowed to dry at room temperature. Two spots were prepared for each volume and each spot was interrogated numerous times with the MALDI laser. Analysis was performed immediately after deposition.

The graph in Figure 71 displays the average signal-to-noise ratio (SNR) for the peptide des-Arginine-Bradykinin (m/z 904) over deposition volume. The signal-to-noise ratio increased steadily from 200 to well over 5500 (arbitrary units) as the deposition volume decreased from 1 μL to 0.1 μL (0.1 μL is the lower physical limit for the manual pipette used in these experiments). Similar trends can be seen for the other peptides in the mixture. The error bars surrounding each data point represent the standard error of the mean [106, 107], defined as the standard deviation of the error in the sample mean, and is calculated as the standard deviation divided by the square root of the sample size.

Measurement noise was calculated with Data Explorer V.4 software from Applied Biosystems and given in root mean square (RMS) form. As shown in Figure 72, RMS noise increased as deposition volume decreased with a maximum at 0.25 μL. From the data shown in Figure 71 & Figure 72, the optimal deposition volume should be 0.1 μL,

www.manaraa.com

which gives a combination of the best SNR and local minimum of RMS noise. However aliquots with this volume are difficult to deposit reproducibly using a manual pipette due to mechanical fluctuation and droplet adhesion to the pipette tip. Therefore, based on SNR performance and ease of deposition, 0.2 µL was the deposition volume selected as the standard for use in future experiments.

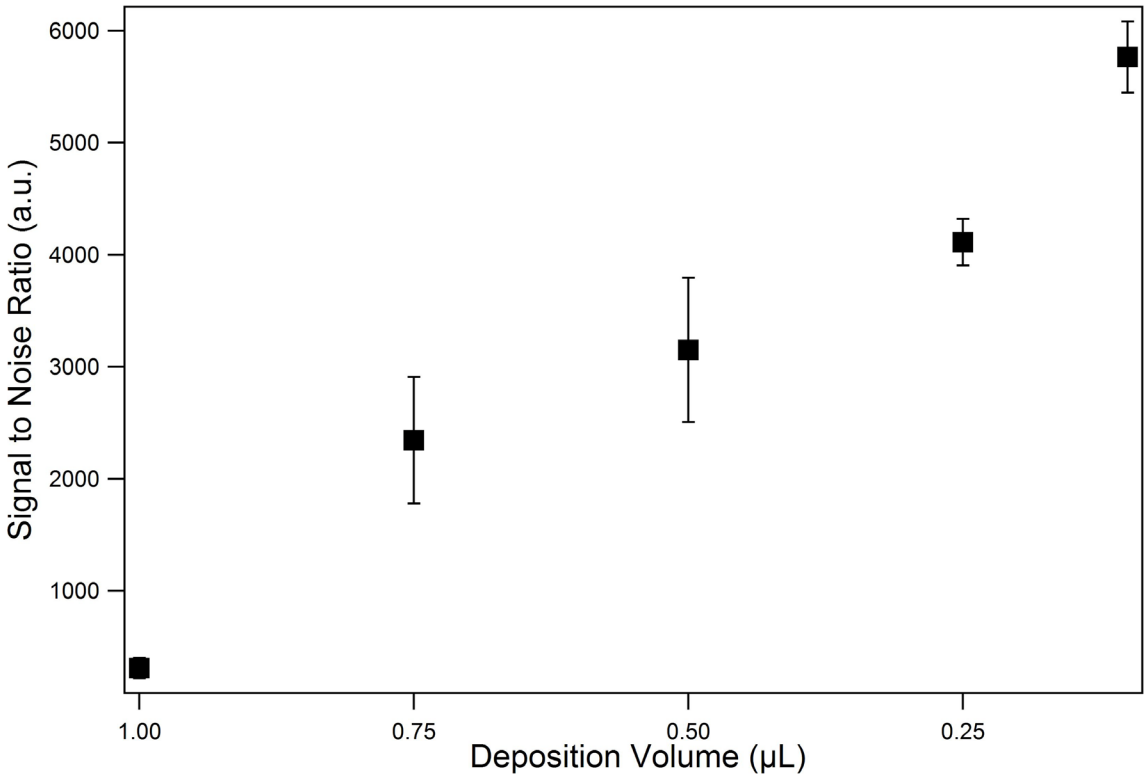

Figure 71. Averaged signal to noise ratio values (in generic units) for the different deposition volumes. The error bars represent the standard error of the mean for the data points.

www.manaraa.com

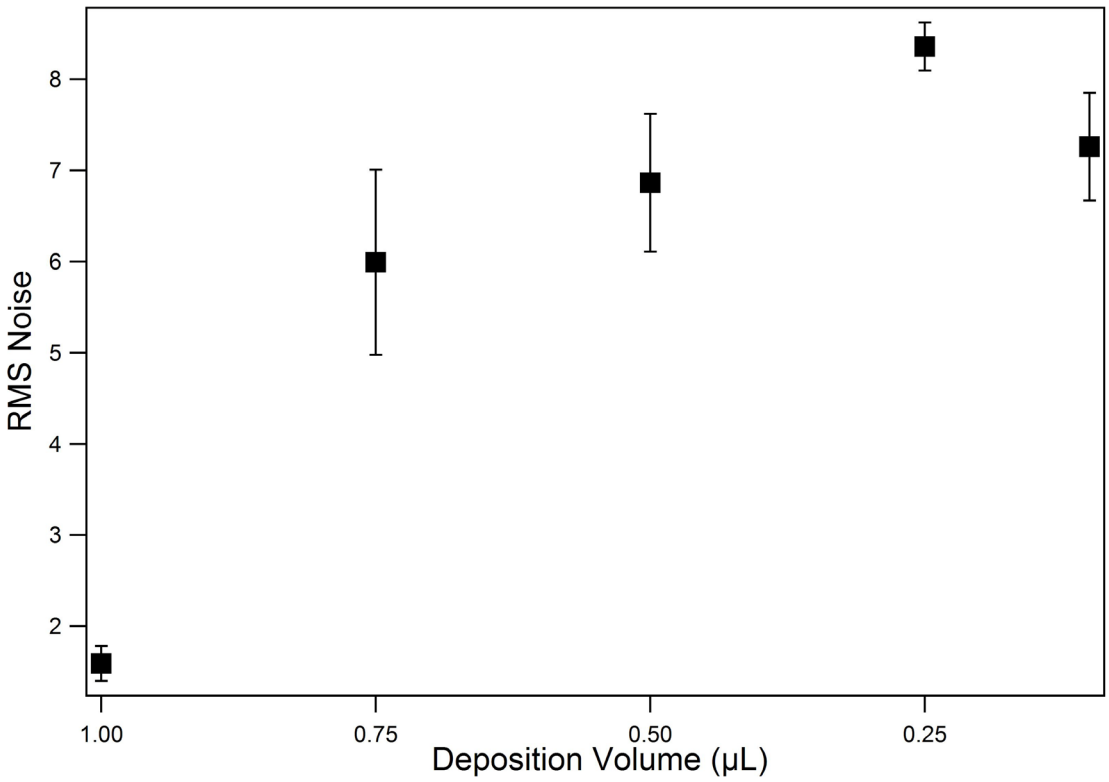

Figure 72. Averaged RMS noise for measurements at different deposition volumes.

4.2.2 Matrix to Analyte Ratio Optimization

In an effort to determine the optimal matrix to analyte ratio, an experiment was conducted to vary both the matrix concentration (αCHCA) and the analyte concentration (peptide mixture 1). The results were analyzed to determine which combination produced the best signal-to-noise ratio (SNR) when investigated with the MALDI instrument. Three matrix concentrations (5 mg/mL, 3 mg/mL, 1 mg/mL), and six analyte concentrations (ranging from 250 fmol/µL to 25 fmol/µL) were investigated. The solutions were combined in equal parts by volume in individual 0.5 mL Eppendorf vials

www.manaraa.com

to represent each combination of matrix and analyte concentration (18 total). The combined solutions were spotted on the standard MALDI plate three times per solution with 0.2 µL deposition volume for a total of 54 spots. Each spot was interrogated five times with the MALDI instrument for a total of 270 spectra, and each spectrum was broken into four peaks of interest for a total of 1080 peaks.

The data from the experiment is plotted in graphs of signal-to-noise ratio versus analyte concentration and grouped according to matrix concentration. The graph for peptide Angiotensin I (m/z 1297), is shown in Figure 73 and is representative of the results from the other peptides. The data in the graph indicates that change in analyte concentration has a stronger influence on MALDI performance than matrix concentration for the tested ranges. The decrease in SNR is significant for the reduction in analyte concentration from 250 to 150 fmol/µL.

www.manaraa.com

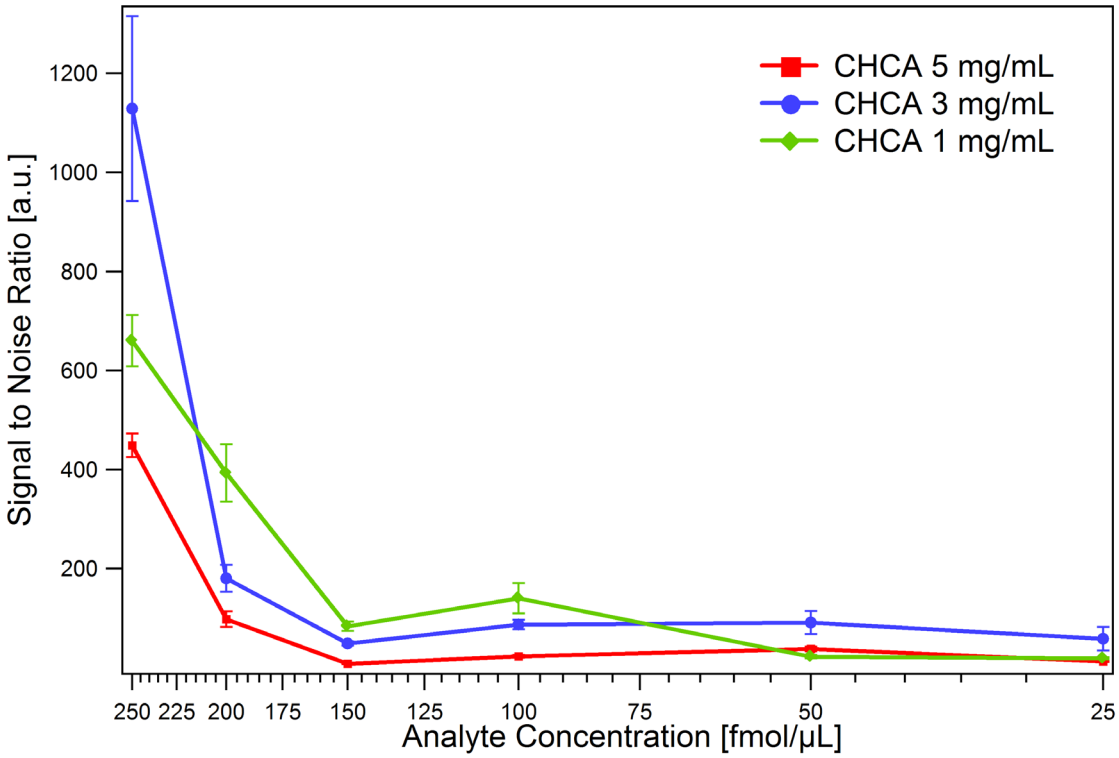

Figure 73. Averaged SNR data (in generic units) versus analyte concentration grouped according to matrix concentration for peptide Angiotensin I (m/z 1297).

To better illustrate the effect of change in matrix and analyte concentration in the MALDI process, signal-to-noise ratio data collected from the same experiment was graphed against the matrix-to-analyte molar ratio in Figure 74. The data is for peptide des-Arginine-Bradykinin (m/z 904) and represents all 18 combinations of solutions. The samples that produce the best signal-to-noise values were prepared from solutions that had matrix-to-analyte molar ratios between 35,000 and 100,000 to 1. This range verifies the value (approx 100,000:1) given in the operating instructions for CALMIX 4700. The samples that produced a small SNR value contained the most matrix (5 mg/mL) coupled with the least analyte (25 fmol/µL) for a molar ratio over a million to one. The combination that produced the lowest SNR on the graph was difficult to interrogate with

www.manaraa.com

the MALDI instrument and only one of the three samples produced a significant signal. The combination of 3 mg/mL of matrix with 250 fmol/µL of analyte (which corresponds to a matrix-to-analyte molar ratio of 63,400:1) performed consistently for both peptides (des-Arginine-Bradykinin and Angiotensin I) and was used as the standard for the subsequently discussed experiments.

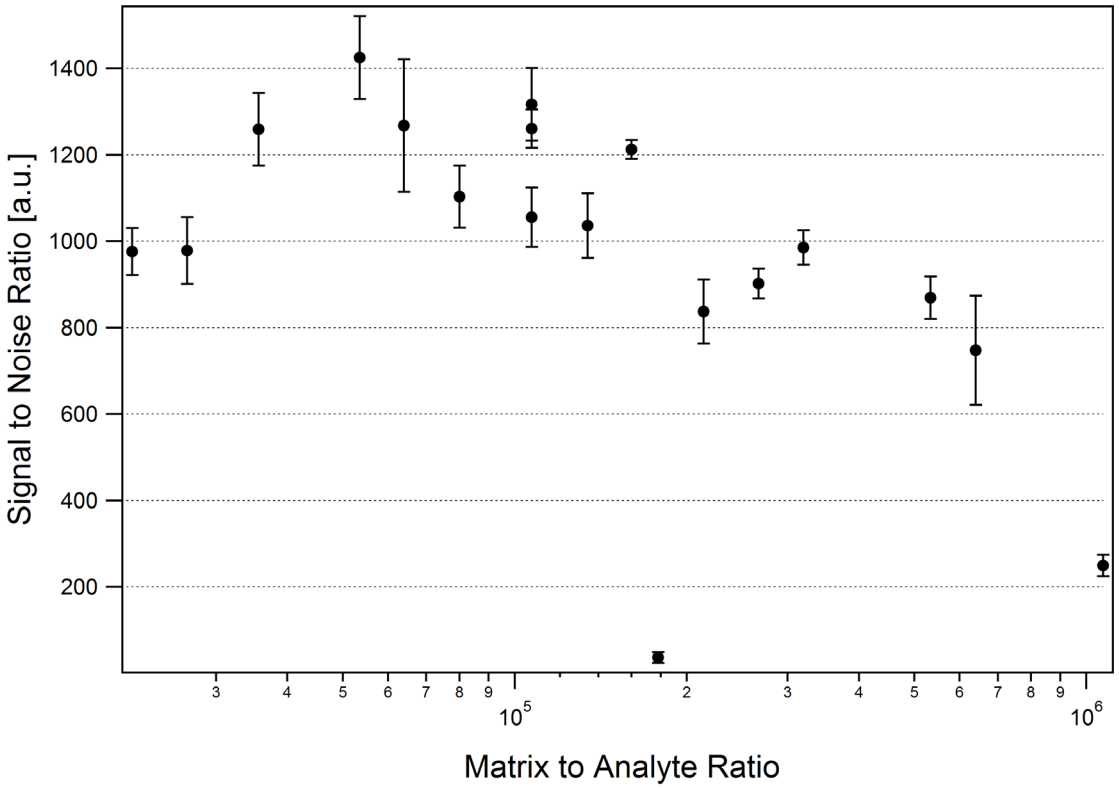

Figure 74. Averaged SNR data (in generic units) for des-Arginine-Bradykinin (m/z 904) plotted versus the matrix to analyte molar ratio of the solution used for deposition.

www.manaraa.com

4.2.3 Performance Comparison of Standard and CNT-enhanced MALDI Substrates

In the previous experiments, the optimal deposition volume and matrix-to-analyte molar ratio was determined. These experiments were designed to investigate the effect of deposition on a carbon nanotube-enhanced substrate on the MALDI process.

Two samples of each type (standard MALDI plate and CNT enhanced substrate) were prepared according to the procedure described in section 3.3. The solution used for deposition contained 3 mg/mL of αCHCA matrix and 250 fmol/μL of peptide mixture 1. The samples were investigated with the Voyager MALDI Mass Spectrometer with settings detailed in section 3.4. Five spectra were collected from different locations on each sample with 250 laser shots collected per spectrum. The signal-to-noise values were averaged for each sample and the data separated into four peak groups with each peak corresponding to a different peptide in the calibration mixture. The results are shown in Figure 75. The error bars surrounding the data points represent the standard error of the mean [106].

www.manaraa.com

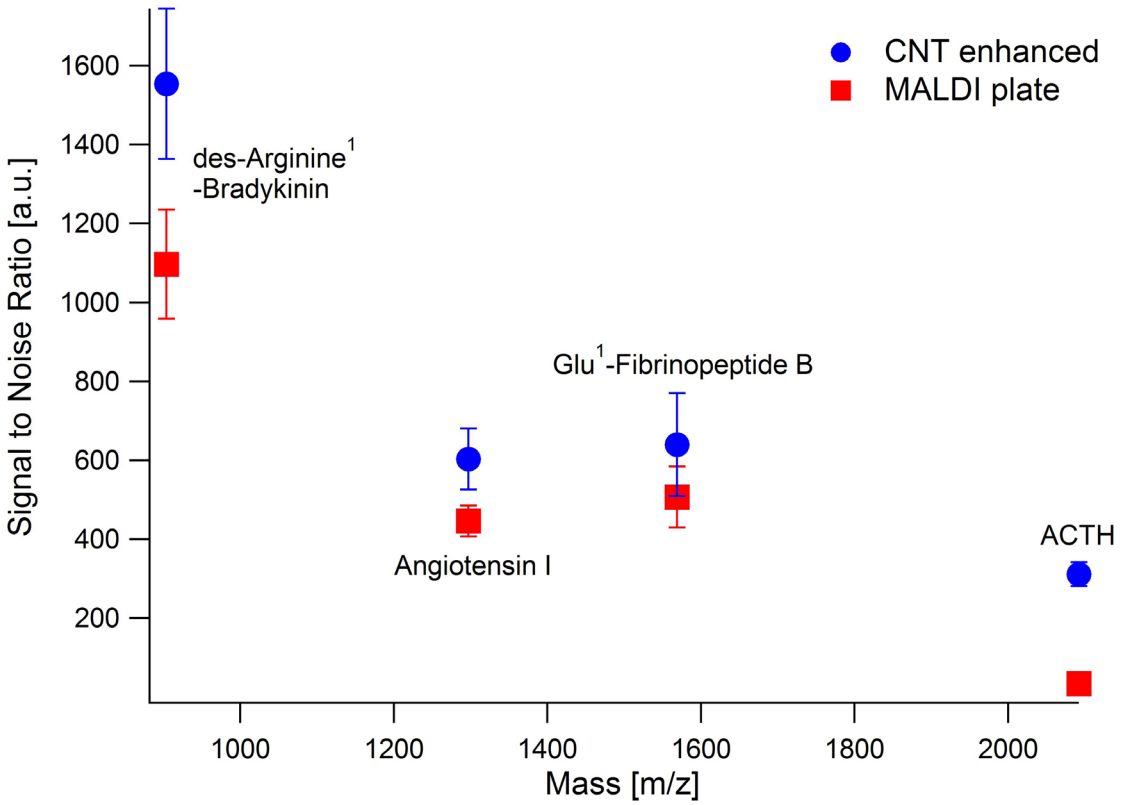

Figure 75. Graph of Signal to Noise Ratio (SNR) (in generic units) for the four peptides in mixture 1 on the standard MALDI plate and the CNT-enhanced substrates.

Data from the samples deposited on the carbon nanotube-enhanced substrate indicates an increased signal to noise ratio compared to that of the standard MALDI sample plate. The raw signal strength from the CNT-enhanced samples was slightly higher than that of the standard samples, however the RMS noise was significantly lower (22.11 for the CNT-enhanced and 32.09 for the standard substrate), which is the main factor in the SNR increase. Des-Arginine[1]-Bradykinin (m/z 904) shows a greater SNR increase than the other peptides, possibly due to differences in molecular weight as Puretzky et al. [37]

www.manaraa.com

demonstrated that lighter molecules travel faster through the desorption plume from the sample to the instrument, which can effect ionization via collisions in the matrix plume.

The analyte ACTH (m/z 2093) deposited on the CNT enhanced substrate also demonstrates an increase in signal strength over the sample on the MALDI plate. This could be misleading, as the MALDI plate SNR values for the ACTH peptide appear to be below the expected performance referenced in the CALMIX 4700 data sheet.

Recently published research has shown that the aromatic carbon rings in the structure of amino acids phenylalanine [96, 108], tryptophan [109, 110], and tyrosine [97] (Figure 76) interact with the surface of carbon nanotubes. The interaction has the potential to enhance the affinity of the peptide for the carbon nanotube surface. Additionally, the aromatic rings in the matrix αCHCA may interact through π-bonds with these aromatic amino acids (Figure 77), resulting in a localization of the peptide in the vicinity of a matrix molecule or crystal. This localization of the peptides can enhance charge transfer via the hopping mechanism detailed in section 2.3.1.1 that was calculated by Setz et al. [48] to be an average of seventeen molecular diameters. A greater number of peptides in contact with charge donating matrix molecules have the potential to increase the charge transfer efficiency per laser shot, which may result in a larger MALDI signal as seen in Figure 75.

www.manaraa.com

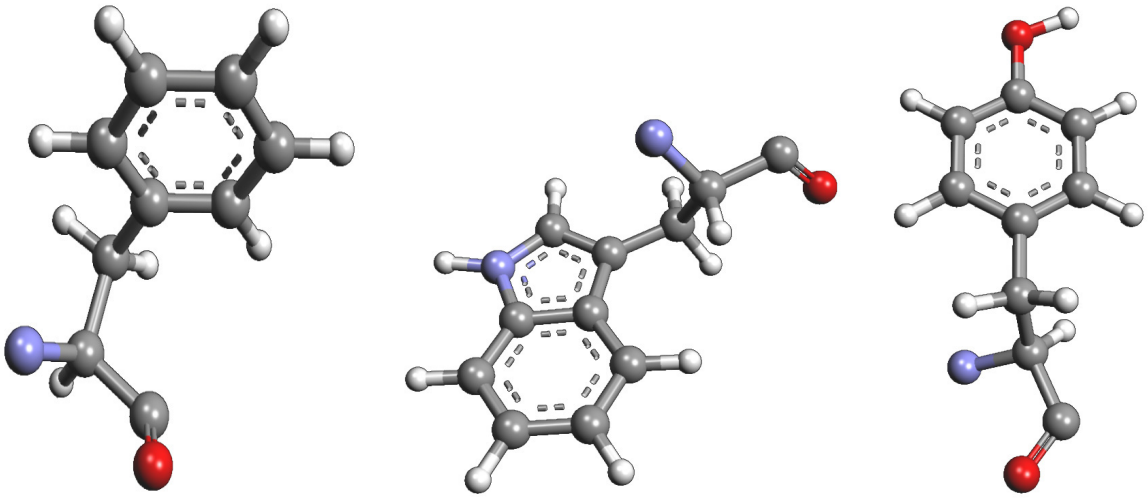

Figure 76. Molecular models of phenylalanine (left), tryptophan (center), and tyrosine (right), illustrate carbon ring structure.

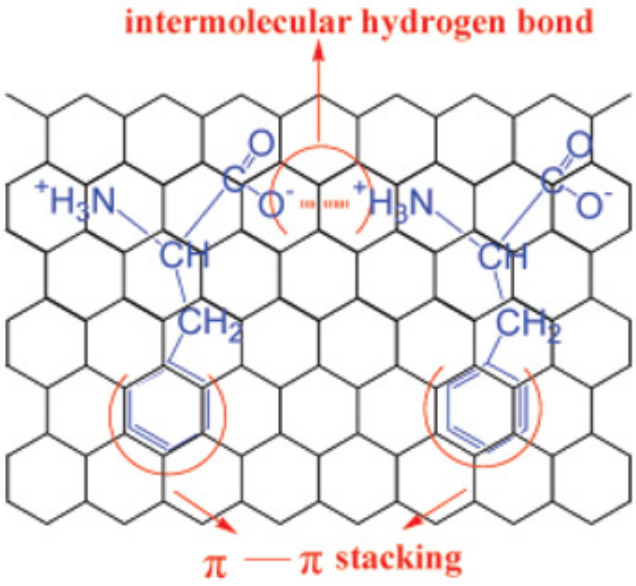

Figure 77. Illustration of π-π bond stacking for phenylalanine adsorption on a carbon nanotube surface [96]. Copyright 2008 with permission from American Chemical Society.

www.manaraa.com

4.2.4 Low Concentration Analyte Sample Analysis

In the previous experiment, the use of a carbon nanotube-enhanced substrate was shown to increase average SNR values for peptide signals collected via the MALDI process. The experiment was performed for a single solution concentration. In order to investigate substrate performance over a range of solution concentrations, and to find the detection limit, an experiment was conducted that focused on substrate performance at low analyte concentrations. This is important for applications involving small quantities of analyte or highly diluted solutions.

Multiple samples were prepared according to the procedure given in section 3.3. The concentrations of analyte peptide mixture 1 ranged from 25 fmol/μL to 0.5 fmol/μL. Two samples were prepared on each type of substrate for each concentration of solution for a total of 24 samples. The matrix concentration was reduced appropriately to keep the matrix to analyte molar ratio constant at 63,400:1, which corresponded to the ratio of 3 mg/mL matrix with 250 fmol/μL analyte that was selected as the standardized ratio in section 4.2.2. The deposition volume was the same as in the earlier experiments, 0.2 μL. The final amount of analyte deposited onto the substrates ranged from 3.25 femtomoles to 65 attomoles, as calculated for analyte component Glu^{1}-Fibrinopeptide B and the SNR data plotted in Figure 78.

www.manaraa.com

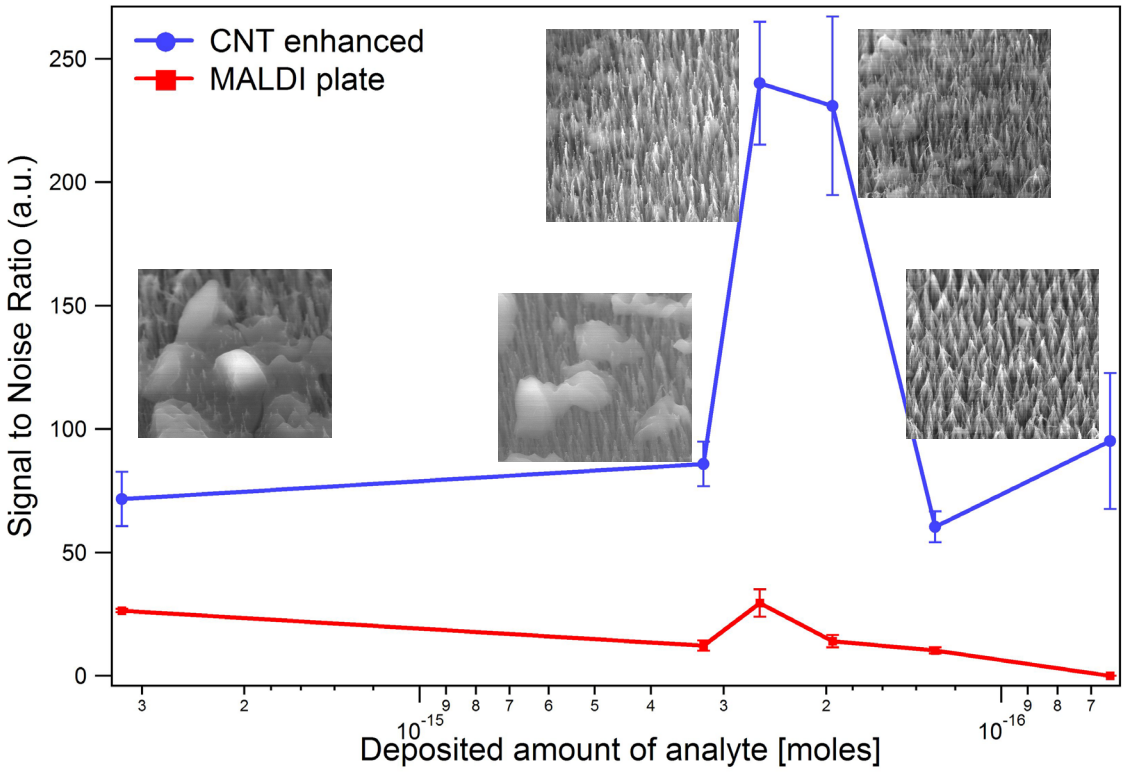

Figure 78. Graph comparing substrate performance over a wide range of analyte concentration. The inset images are SEM images of the crystal deposits on the CNT enhanced substrate that correspond to the data points. Signal to Noise Ratio in generic units.

The average signal from the samples on the standard MALDI plate declined with decreasing analyte concentration and no signal was detected below 130 attomols. The samples deposited on carbon nanotube-enhanced substrates showed an overall increase in intensity with a significant gain in the 250 attomol range. In addition, the CNT enhanced sample produced a signal at the minimum analyte concentration used for this experiment. The error bars surrounding the data points represent the standard error of the mean.

www.manaraa.com

The series of images inset in Figure 78 are scanning electron microscope images of the samples that correspond to the data points on the graph. The morphology of the crystals changed over the range of concentrations, partially due to the different amounts of αCHCA matrix that was deposited with the analyte. At higher concentrations, the matrix produced large crystals with a defined, cubic structure. Below the 300 attomol level, the crystals are significantly smaller and more numerous, which should provide an increase in the overall crystalline surface area. The change in the morphology of the crystals could account for the signal intensity increase in the center of the graph. As discussed in section 2.3.3.1, Vorm et al. [57] reported a two order of magnitude increase in sensitivity due to a reduction in matrix crystal size using αCHCA. The increased surface area could allow a greater flux of matrix and ionized analyte molecules to desorb from the sample surface when excited by the laser in the MALDI instrument.

The performance of commercially available AnchorChip™ plates has been verified in literature. Zhang et al. [111] compared the sensitivity of the dried droplet and sample matrix wash (SMW) techniques, and published the detection limit for peptides deposited on the AnchorChip™ plate using αCHCA as the matrix. Analyte signal was detectable at 0.4 femtomoles for the dried droplet technique and 0.1 femtomoles for the SMW technique, with a signal to noise ratio between 5.5 and 39.5. The dried droplet deposition on patterned carbon nanotubes presented in this work was able to produce a quality signal (SNR of approximately 100) at 65 attomoles.

www.manaraa.com

4.2.5 Analysis of Substrate Influence on the Matrix Desorption Threshold

Determination of threshold irradiance is important in MALDI sample processing. Setting the laser intensity too high can cause increased measurement noise and loss of mass resolution due to increased peak width. Laser intensity below the desorption threshold can lead to decline of analyte signal below a detectable level. This experiment analyzed the threshold irradiance for samples prepared on the standard MALDI plate and carbon nanotube-enhanced substrates

During the MALDI process, laser energy is absorbed by the matrix crystals and generates various levels of excited states. As discussed in section 2.3.1.1, these states are responsible for ionization and desorption. The excitations not used for ionization are converted to heat. Desorption is primarily dependent on the S_1 (first excited state above ground level) population and occurs within the S_1 time scale. Through the process of energy pooling, S_1 states are able to collect in localized areas and contribute to crystal heating and desorption. Increasing the laser fluence considerably above the plume generation threshold can lead to large amounts of S_1 states and excessive matrix desorption with increased noise in a sample spectra

The relationship of threshold irradiance to laser focal diameter was investigated by Ingendoh et al. [51] and is discussed in section 2.3.1. The samples investigated in that experiment were prepared at a constant concentration and deposited onto a metal MALDI plate with a deposition volume of 1 µL. Images of the samples were not published,

www.manaraa.com

however the sample deposition process is well documented, and it can be assumed that aliquots of identical volume and concentration would produce samples with consistent crystal density (number of crystals per unit area). The samples were investigated with the laser diameter varied from 280 µm to 10 µm. A reduction in the laser diameter equates to less matrix crystals interrogated simultaneously, and fewer S_1 states produced. The result was an ionic flux reduction into the MALDI instrument and a decline of signal intensity below detection. To compensate for the signal loss, the irradiance was increased, and the additional energy was converted to additional S_1 states, increasing desorption from the surface.

For a MALDI instrument with a fixed diameter laser, the effect of increasing the crystallite density should increase the generation of S_1 states and decrease the threshold irradiance required to produce a signal. A secondary benefit could be enhanced signal intensity as a result of increased crystal contact and energy pooling of excitation states for improved ionization.

An experiment was performed to test the performance of carbon nanotube-enhanced substrates over a range of laser intensities. The matrix and analyte concentrations used were 0.25 mg/mL (αCHCA) and 2.5 fmol/µL (peptide mixture 1) respectively. Two samples were prepared, one on a carbon nanotube spot (sample #1) and one on the standard MALDI plate (#43) using a deposition volume of 0.2 µL. Two other samples (#2 and #44) were prepared using a deposition volume of 0.5 µL in order to document any change in performance between the two sets of substrates with respect to deposition

www.manaraa.com

volume. Table 6 contains a summary of the sample configuration and dried droplet measurements.

Table 6. Deposition conditions and resulting dried droplet sizes.

Sample	Substrate	Volume (μL)	Area (mm^2)	Diameter (mm)
1	CNT	0.2	0.021	0.206
2	CNT	0.5	0.207	0.496
43	MALDI plate	0.2	0.651	1.104
44	MALDI plate	0.5	1.285	1.306

For this experiment, the laser intensity of the MALDI instrument was increased incrementally from 2000 to 2400 (arbitrary units given in the instrument control software). The neutral density filter that attenuates laser energy is linear within this range. Spectra were collected from 250 interrogations at constant laser power for each step. Data Explorer software was used to analyze the spectra and produce SNR data. IGOR Pro was used to plot the data for the analyte signal from the des-Arginine^1-Bradykinin (904m/z) peptide.

The data for spots 1 and 43 (0.2 μL deposition volume) is plotted in Figure 79. The CNT-enhanced sample produced a slightly higher SNR (338.7 a.u.) than that of the standard sample (329.8 a.u.). However, the peak occurred at a lower laser intensity (2150 vs. 2300 a.u.), indicating increased efficiency of laser absorption and signal generation.

www.manaraa.com

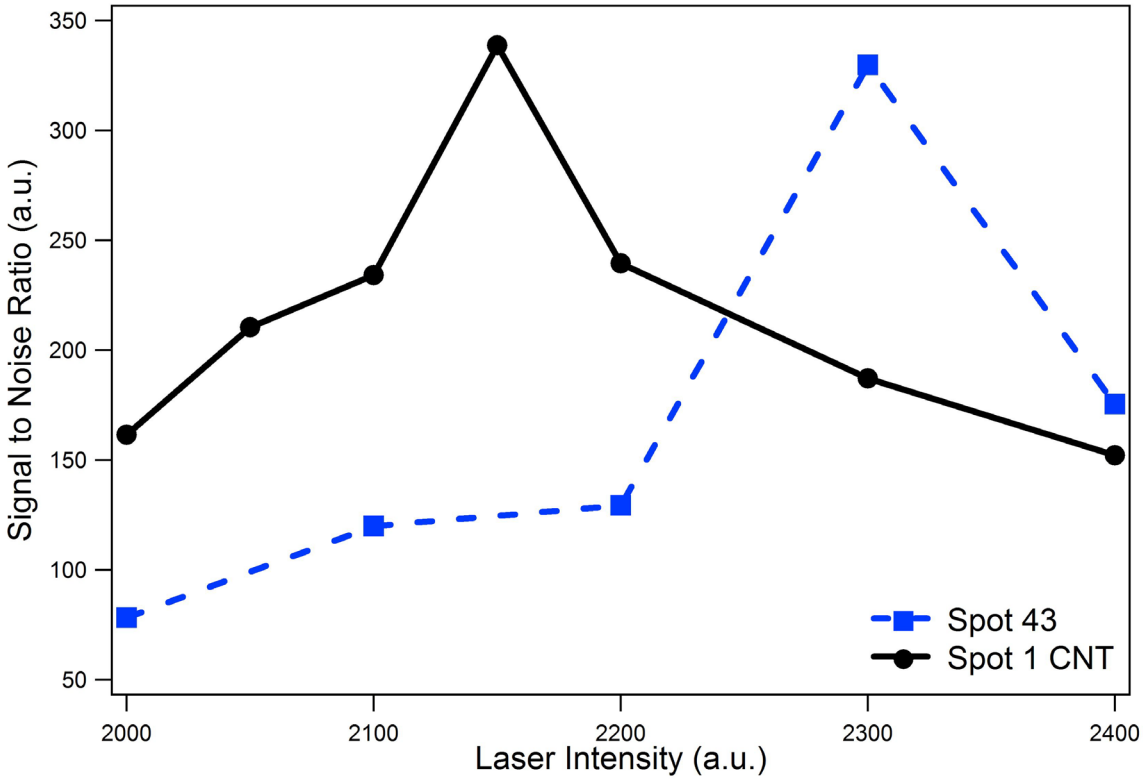

Figure 79. SNR data (in generic units) versus laser intensity (in arbitrary units) for samples prepared with 0.2µL of solution.

Figure 80 graphs the data for spots 2 and 44 (0.5 µL deposition volume). The performance difference between the two samples is more pronounced (628.2 vs 329.7 a.u.). The SNR values for these samples are higher than those deposited with 0.2 µL possibly due to a larger quantity of matrix/analyte deposited on the sample. The fluctuations shown in the graph could be the result of variations in crystal formations over the larger dried droplet diameter.

www.manaraa.com

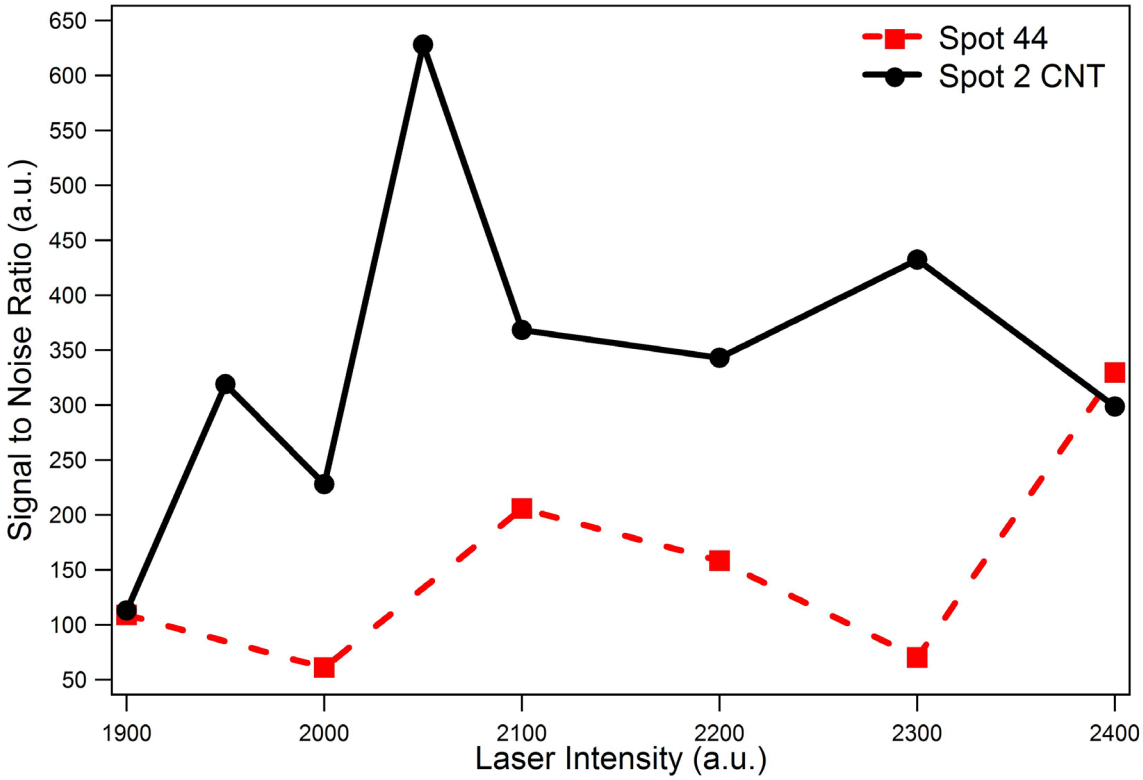

Figure 80. SNR data (in generic units) versus laser intensity (in arbitrary units) for samples prepared with 0.5µL of solution.

The performance of the carbon nanotube-enhanced substrates is thought to be a result of lateral concentration of the matrix crystals into an area approximately the size of the laser beam at the point of investigation. This localization can increase inter-crystalline contact and maximize simultaneous interrogation, resulting in an enhancement of the ionization process through increased interaction of excitations, both on the sample surface and in the plume.

In addition to the standard optical microscopy, scanning electron microscopy was performed on spots 1 and 2 after the initial deposition and again after the series of

www.manaraa.com

MALDI interrogations. The difference in matrix crystal morphology illustrates the effect of the desorption process in removing material from the sample. The carbon nanotubes appear unchanged after the MALDI process.

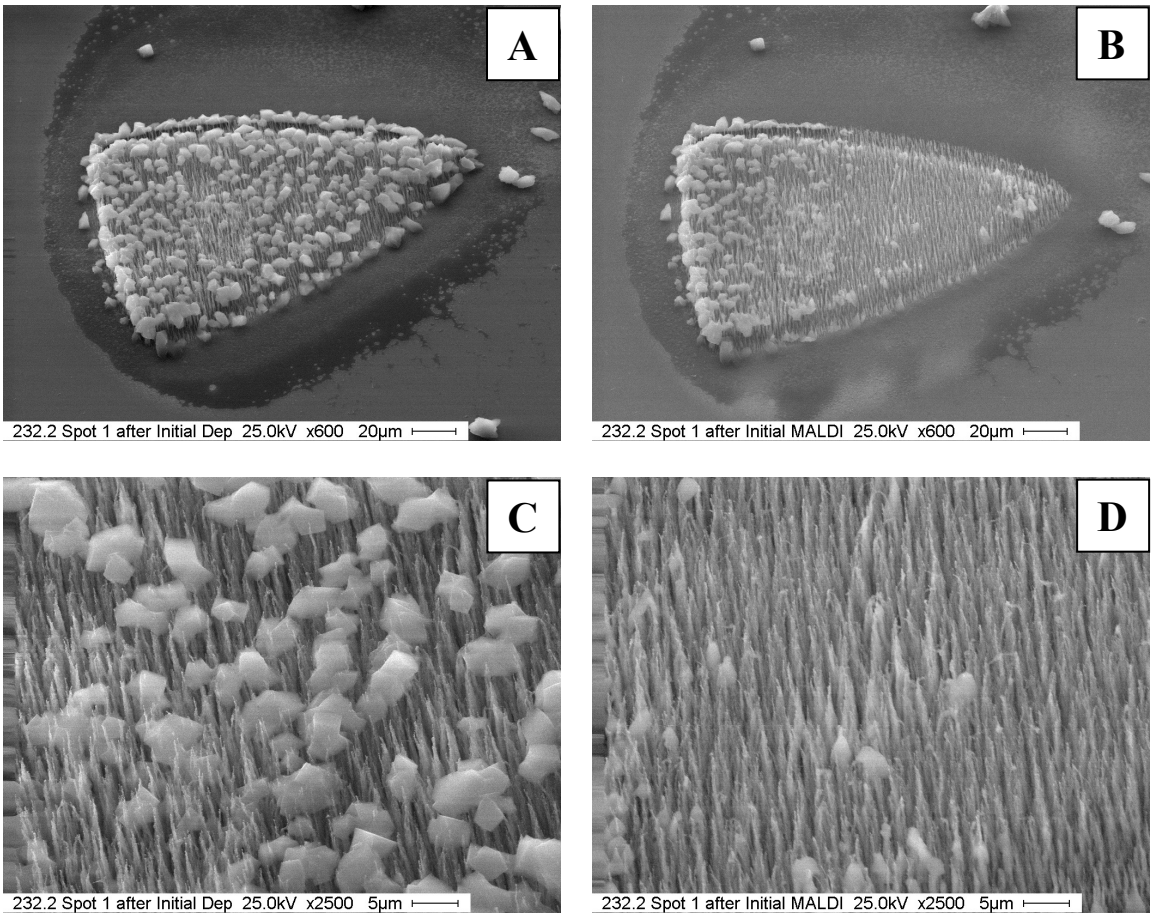

Figure 81. Scanning electron microscope images of spot 1 after initial deposition (A) and MALDI investigation (B). Images C and D are higher magnification images of A and B respectively, illustrating change in crystal morphology.

In the magnified images (Figure 82 C and D), the tips of the carbon nanotubes can clearly be seen protruding from the matrix crystals, which is an indication of matrix interaction with the nanotube surface.

www.manaraa.com

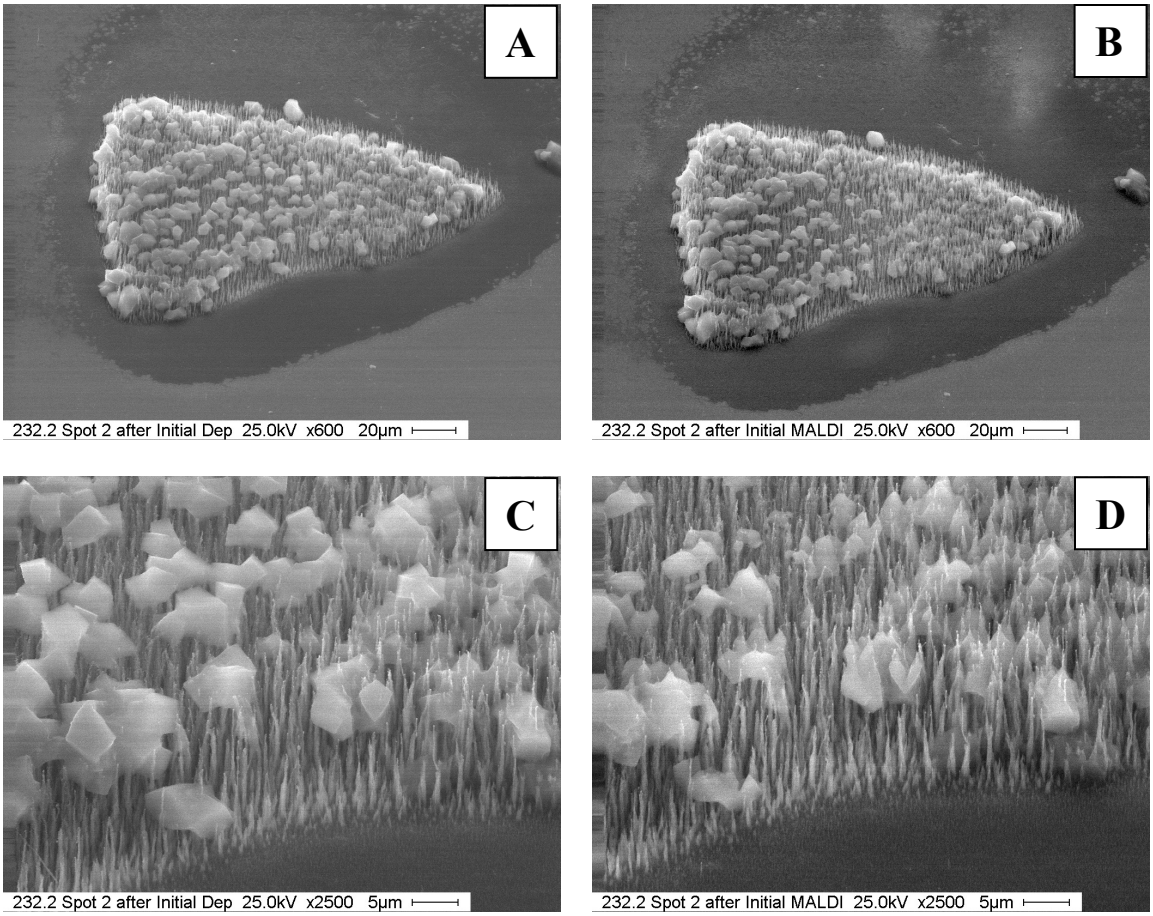

Figure 82. SEM images of spot 2 after initial deposition (A) and MALDI investigation (B). The difference between images C and D are clearly evident.

The results of this experiment demonstrate the importance of laser intensity optimization for each sample to maximize SNR values. Excessive laser power can decrease mass resolution (known from literature) and can cause a change in crystal morphology as a result of the desorption process.

www.manaraa.com

4.2.6 Interrogation of Re-crystallized MALDI Samples

MALDI investigation of a single matrix crystal at constant laser intensity yields an analyte signal for a number of interrogations until the signal weakens and dissipates. Occasionally, increasing the laser intensity will temporarily restore the analyte signal; however the signal eventually becomes diminished below the detection level.

The purpose of the re-crystallization experiment was to determine if the MALDI process extracted analyte from the entire volume of a matrix crystal. Experiments were performed that showed the ability to dissolve and re-crystallize previously deposited matrix crystals, similar to a two-step deposition process (section 2.3.3.1), by applying a similar volume of organic solvent that was used in the initial deposition. Through experimentation, the ratio of acetonitrile to de-ionized water in solution was optimized to ensure dissolving of the matrix crystals while maintaining a similar dried-droplet size and a reasonable drying time at room temperature.

Matrix crystals were investigated to the point of signal exhaustion, then re-dissolved with solvent to allow any analyte that remained in the volume of the crystals to disperse throughout the matrix/solvent solution and redistribute in the new crystals that formed as a result of the solvent evaporation. Performing a MALDI analysis of the new re-formed crystals would reveal the presence of analyte by a recovery of the analyte signal. The process of interrogation and re-crystallization is referred to as a "MALDI Cycle" and was repeated until further cycles failed to produce any signal from the analyte.

www.manaraa.com

The solutions used in this experiment were prepared as per section 3.3 with 3 mg/mL concentration of matrix αCHCA to 250 fmol/μL of analyte peptide mixture 1. Two spots on the standard MALDI plate (spots 45 & 46) and three carbon nanotube spots (numbered 3, 5, & 6) were selected for deposition. Table 7 lists the volumes of solution for the initial deposition and for the re-crystallization. The solution used for re-crystallization consisted of 50% acetonitrile in de-ionized water (no matrix or analyte).

Deposition was performed under an Olympus Digital Stereoscope with time-lapse images captured to document change in crystallization area and distribution. MALDI instrument settings were unchanged during the experiment. Each collected spectra contains data from 250 laser pulses. A minimum of five spectra were collected at each spot for each re-crystallization step. For this experiment, des-Arginine[1]-Bradykinin (m/z 904) was used as representative mass signal.

Table 7. Solution volumes used for initial deposition and re-crystallization cycles.

Initial Deposition Volume (Matrix & Analyte)		Re-crystallization Solution Volume (Solvents Only)	
Spot 3 (CNT)	0.2μL	Spot 3 (CNT)	0.3μL
Spots 5 (CNT) & 45 (Std.)	0.2μL	Spots 5 (CNT) & 45 (Std.)	0.4μL
Spots 6 (CNT) & 46 (Std.)	0.5μL	Spots 6 (CNT) & 46 (Std.)	0.6μL

www.manaraa.com

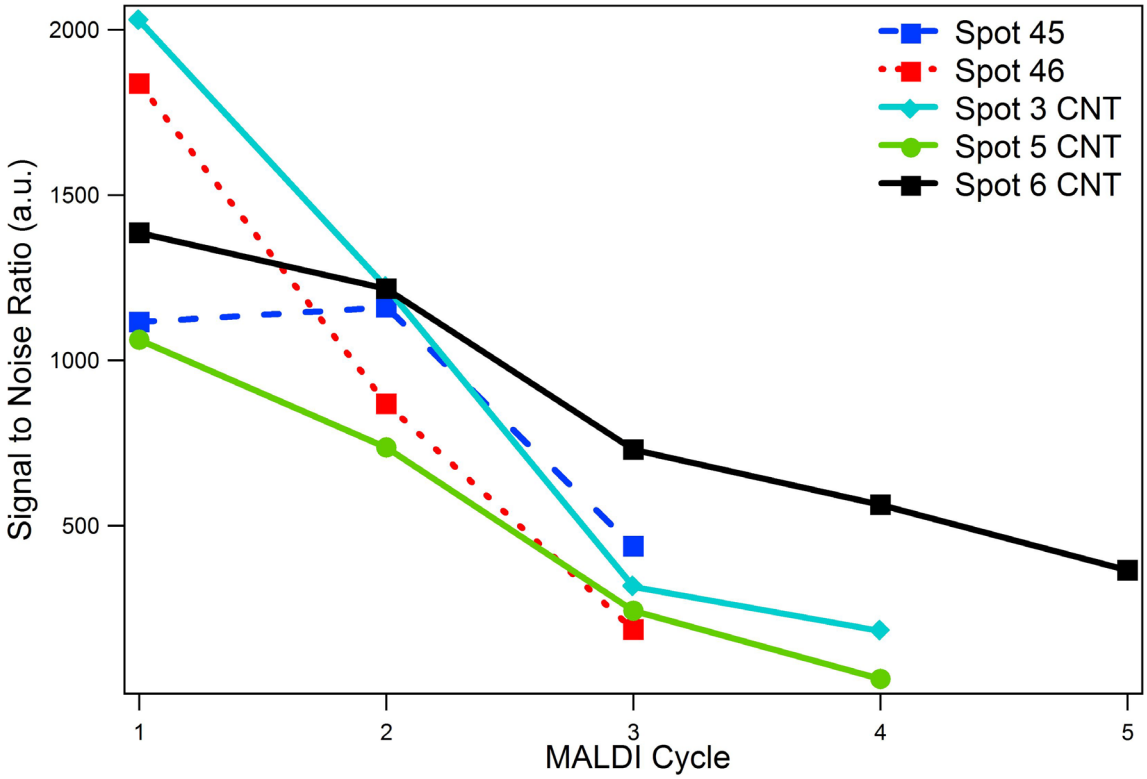

Figure 83. Average SNR values (in generic units) for the different samples versus the number of MALDI cycles.

The SNR values for the experiment were grouped by MALDI cycle and are plotted in Figure 83. The results indicate that the samples deposited on the standard MALDI plate (45 & 46) produced a signal for three cycles of interrogation and re-crystallization. Samples 3 & 5 (0.2 µL deposition volume) deposited on carbon nanotubes produced a measurable signal after four cycles and sample 6 (0.5 µL deposition volume) after the fifth cycle. The fact that any of the samples produced a signal after the initial interrogation and re-crystallization indicated that the MALDI process did not remove analyte from the entire crystal, but only from the outer layers.

www.manaraa.com

Complete signal attenuation was ensured after every MALDI/re-crystallization cycle by systematically sweeping the laser beam (at constant power) over the entire sample surface until no additional analyte signal was produced. This ensured that any signal produced after re-crystallization was the result of analyte that had migrated from the interior of the sample, and not from the re-arrangement of crystals that were outside of the scope of initial laser interrogation. Figure 84 shows the required number of laser blasts for complete signal attenuation for each sample for each step in the experiment.

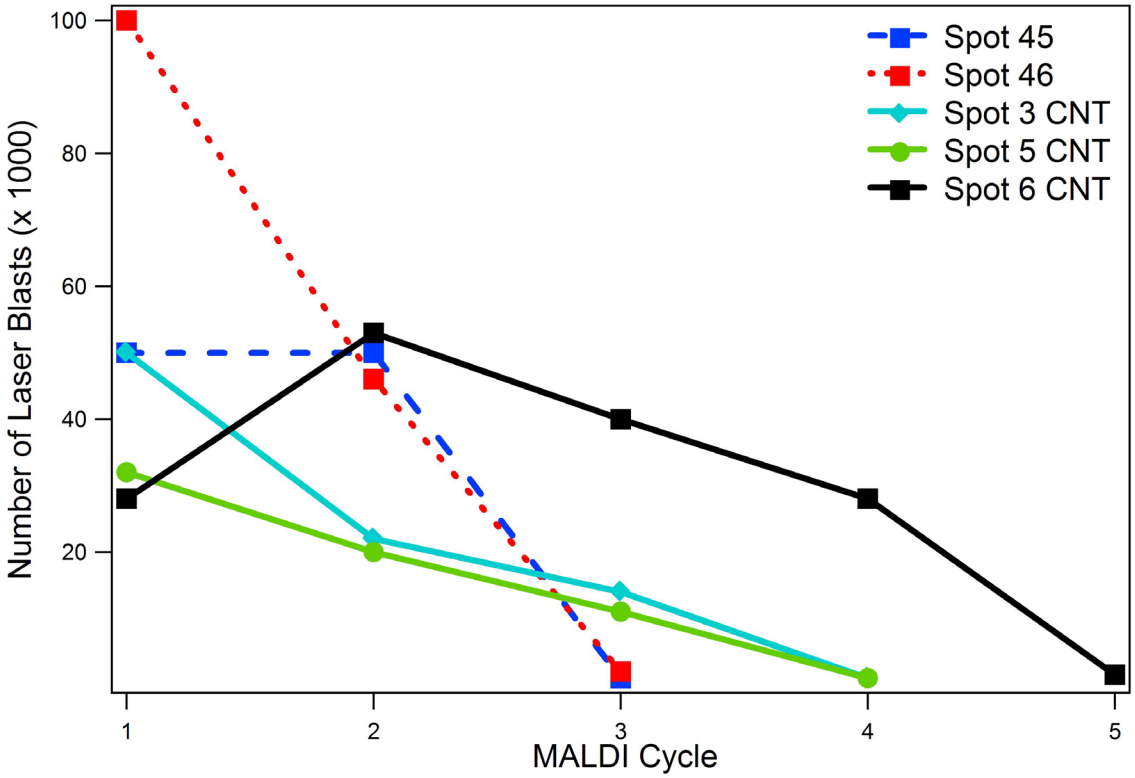

Figure 84. Required number of laser blasts (in thousands) required for signal attenuation for each sample over the course of five MALDI cycles.

www.manaraa.com

Samples 3 and 5 deposited on the CNT-enhanced substrate are similar and show an almost linear decrease in the number of laser blasts with each MALDI cycle. The increase in the 2nd MALDI cycle for sample 6 was due to an increase in sample area after re-crystallization, requiring more interrogations for signal depletion. The number of laser blasts is totaled for the entire area of each sample and due to inhomogeneity in crystal composition and distribution, any attempt to quantify the amount of analyte that is removed for each MALDI investigation cycle would be inaccurate. A similar investigation of a single matrix crystal may provide accurate data for quantification.

After every re-deposition step, the diameter of the sample was measured via optical microscope and the area calculated. The data in Figure 85 shows a general increase in sample area with each re-deposition cycle with the exception of the second cycle for spot 6, which decreased sample area from 1.267 to 0.93 mm^2. Combining the data from Figure 84 and Figure 85 illustrate the trends in the physical sample parameters. With each successive re-crystallization step, the samples became larger and required fewer laser blasts to achieve attenuation as a result of reduced analyte molecules present in the matrix crystals from material ablation.

www.manaraa.com

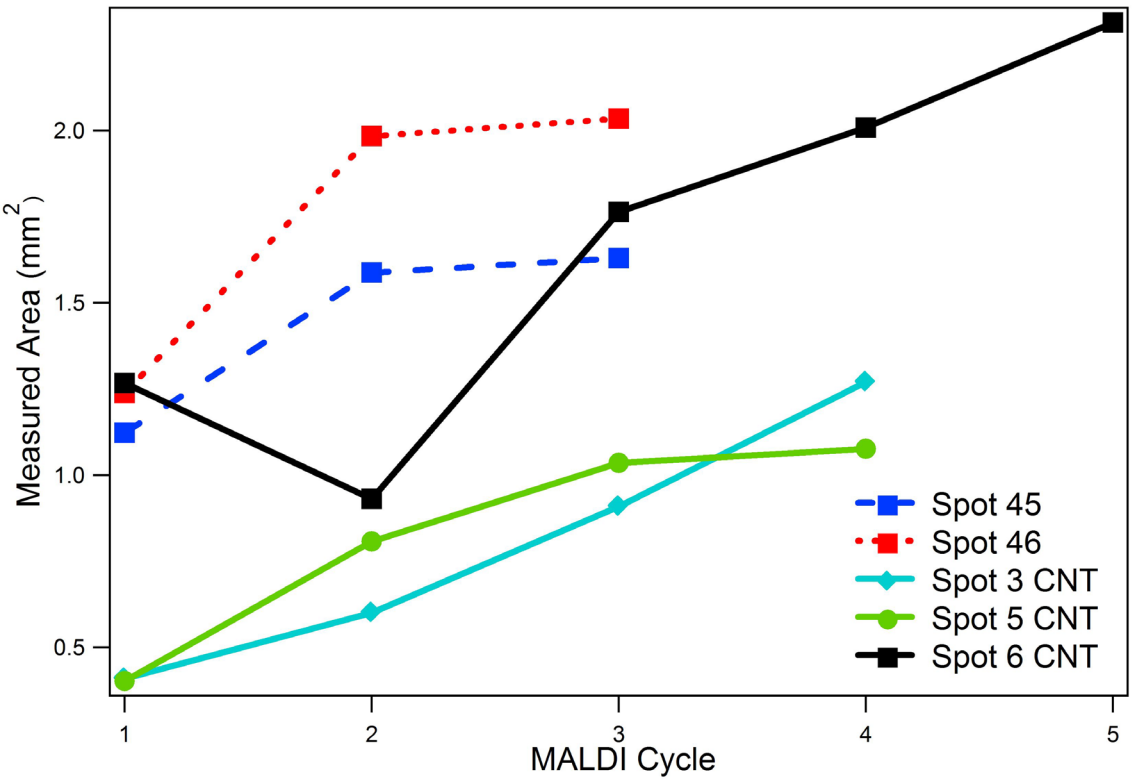

Figure 85. Dried droplet sample area (in square millimeters) measured using optical microscopy after every MALDI cycle.

The graph of threshold laser fluence (Figure 86) shows the minimum instrument setting for laser intensity necessary to produce a signal greater than the measurement noise. As detailed in section 4.2.5, the threshold fluence can be used as a measure of comparative efficiency for the MALDI process after each cycle. The lower the laser intensity required to produce a quality signal, the more efficient the crystal formation is at laser energy absorption and ionization. The trend displayed by the graph suggests that the crystals become less efficient after every re-crystallization, possibly due to a decrease in crystal density as the deposit size increases, which can decrease the generation of S_1 states, effecting desorption from the surface and negating energy pooling. Additionally,

www.manaraa.com

the crystals contain sequentially fewer analyte molecules after every MALDI interrogation due to the ablation process.

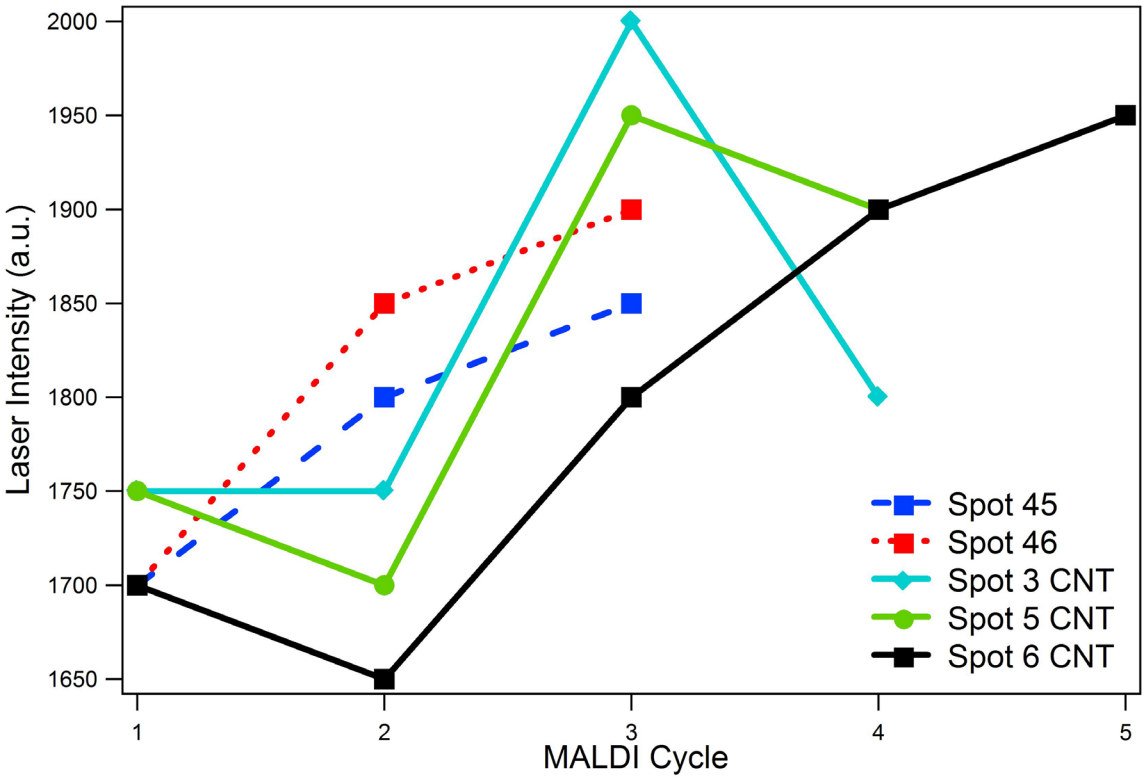

Figure 86. The threshold irradiance (in generic units) required to produce a quality signal versus the number of MALDI cycles.

The apparent congruence of the plots for samples 6, 45, & 46 in Figure 85 and Figure 86 demonstrated the relationship between sample area and threshold irradiance, which was discussed in sections 2.3.1 and 4.2.5. This data was plotted relative to each other, and can be seen in Figure 87, along with the corresponding linear trend lines. The data for samples 3 and 5 did not display a linear relationship for area and intensity. The differentiation appears to be size related, possibly with respect to the area of the MALDI

www.manaraa.com

laser at the point of interrogation, since the samples that are considerably larger than the laser have a good fit to the linear approximation.

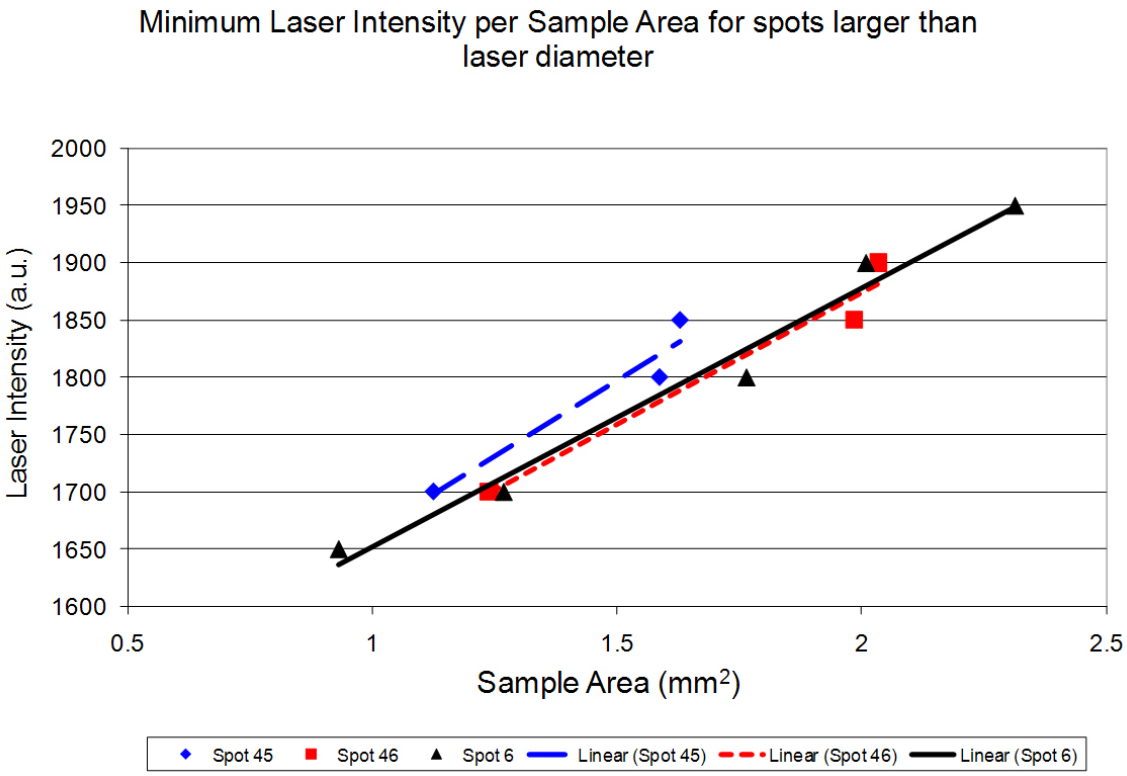

Figure 87. Graph of minimum laser intensity (in generic units) versus measured sample area.

The demonstrated relationship provides considerable information about the effect that increased sample diameter has on the MALDI process. The samples increase in diameter with each cycle, thereby reducing the crystal density in the interrogated area. The increased distance between matrix crystals can reduce the ability for excitation energy transfer, which is theoretically limited to seventeen molecular diameters [48]. As a result of a fixed laser diameter, the laser intensity must be increased to compensate for the loss of energy transfer. For samples that have an area similar to that of the laser (samples 3

www.manaraa.com

and 5), the required intensity fluctuated as the sample area increased, possibly due to inhomogeneity of the crystal field as a result of the re-crystallization process.

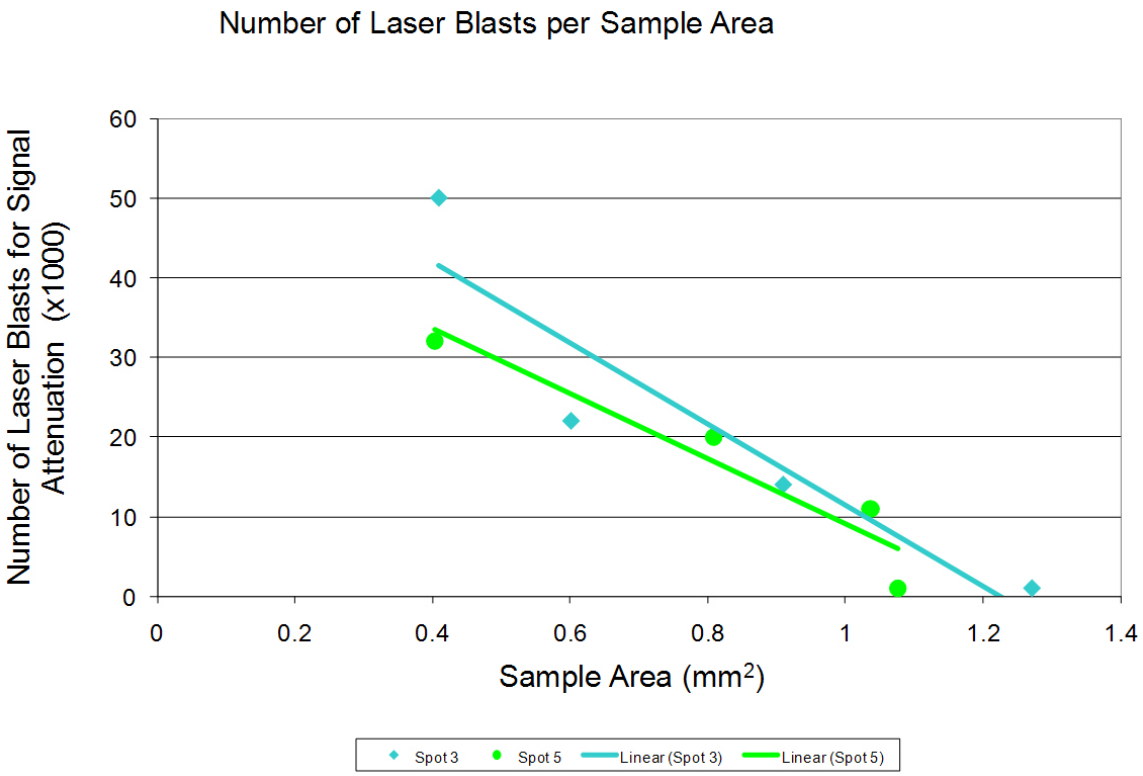

Figure 88. Required number of laser blasts (in thousands) required for signal attenuation versus measured sample area.

Another parameter that appears to be dependent on sample size is the sample area to number of laser blasts required for signal attenuation (Figure 88). Samples 3 and 5 were the only ones to display a linear relationship. The other samples (6, 45, & 46), which were considerably larger in diameter than the MALDI laser, did not have a good fit to any linear trend lines. While this data may not be immediately useful, significance may be discovered for possible modeling applications of sample deposit/beam interactions.

www.manaraa.com

Recently published work by Jaskolla et al. [112] has produced data concerning depth profile information for the MALDI process. The penetration depth of the laser (355nm wavelength, 3.47 electron volts) was calculated by atomic force microscopy of a matrix (αCHCA) crystal surface after exposure to a given number of laser shots. The average height difference between the center of the crater formed by the laser and the surrounding crystalline area was divided by the number of laser shots and was found to be 6.4 ± 1.5 nm per laser shot. The description of this data as "laser penetration depth" could be more accurately termed "laser ablation rate", as the value measured was material ablation rather than the penetration of the laser into the matrix crystal. It should be noted that this data was collected with the laser power adjusted to provide optimum signal to noise values from the sample being investigated, and that the ablation rate could vary based on a number of parameters including laser intensity, crystal density at the point of investigation, substrate material and matrix composition.

The laser ablation rate for matrix αCHCA with the instrument configuration used in this research (337nm wavelength, 3.69 eV) can be calculated using images from the scanning electron microscope. The SEM images from Figure 82 (C and D) were compared and the ablation of the matrix crystals was measured using ImageJ software. The average ablation rate was 1.32 nm per laser shot. It must be remembered, however, that this rate was derived from crystals with exposure that was varied in intensity from 2000 to 2400 (arbitrary units), so the photon flux was not held constant. This measured rate is only 20% of the published ablation rate. Factors such as a possible Gaussian beam

www.manaraa.com

profile for the laser, potential differences in matrix absorption of photons (355nm versus 337nm), target substrate material, and crystal spacing must be taken into account.

The work by Jaskolla et al. also provided data that displayed the change in signal to noise ratio of analyte with regards to matrix crystal penetration (Figure 89). This indicates possible inhomogeneity of analyte dispersion in matrix crystals, which may be a contributing factor to the retention of analyte in the crystals beyond the point of signal depletion (Figure 83).

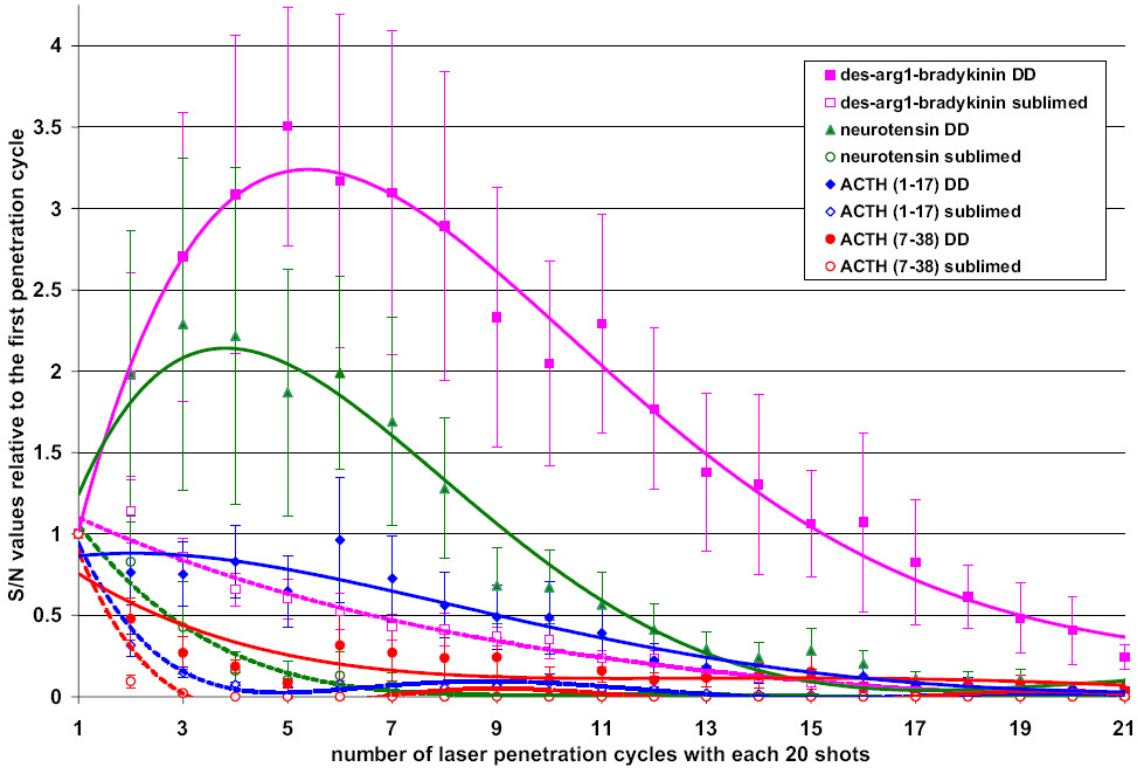

Figure 89. Graph of relative S/N values (in generic units) over a number of investigation cycles [112]. The data of interest is for the peptide samples created via droplet deposition (labeled DD). Copyright 2009 with permission from Elsevier.

www.manaraa.com

Interestingly, for samples that were created via standard drop deposition techniques (labeled DD in the figure), each of the analytes displayed different behavior with regards to whether the s/n value increased or decreased with increasing matrix ablation. A possible explanation for this phenomenon could be the differences in mass of the analytes. Des-Arginine^{1}-Bradykinin (904 Da) shows a 3x increase in s/n ratio with increasing penetration, while heavier peptides such as ACTH (3657 Da), display either a smaller increase or a decrease in s/n ratio with increasing crystal penetration.

Imaging techniques such as Confocal Laser Scanning Microscopy [113] could be useful in mapping analyte locations inside a matrix crystal, and observing the change in analyte concentration during re-crystallization to quantify the amount of analyte that is removed during each MALDI investigation cycle. This data could be used to verify depth profile information for various analytes and construct location gradients that could be used to further understand the mechanisms for analyte dispersion during the crystallization process.

www.manaraa.com

Chapter 5: Summary and Future Work

5.1 Summary

Utilizing patterned carbon nanotubes in the MALDI sample preparation process has been shown to anchor the deposited liquid matrix/analyte solution and provide a seeding area for the growth of matrix crystals during the evaporation process. The ring-shaped crystallization pattern of matrix αCHCA deposited on a standard MALDI plate during the dried droplet process appeared to be influenced by Marangoni convection and droplet edge pinning as described by Bhardwaj [87] and was documented via optical microscopy during the sample preparation process. Deposition of an identical solution on a carbon nanotube-enhanced substrate displayed preferential nucleation on the CNTs, which enables droplet diameter reduction without significant deposition on the surrounding substrate. Deposition was also performed on a clean silicon wafer and a substrate with patterned areas of nickel in order to test for possible interaction. In both cases, no preferential nucleation was observed, and the results were similar to a standard MALDI plate deposition, which indicates that the carbon nanotubes are responsible for the change in drying behavior.

The initial explanation for the preferential nucleation was thought to be the result of π-π bonding of the carbon nanotube outer shell with the aromatic ring structure of the matrix molecule. Experiments were performed to verify this interaction based on the presence of an aromatic ring, with additional consideration for attached hydroxyl and carboxyl groups. Results demonstrated that the carboxyl group did not interact with the

www.manaraa.com

carbon nanotubes in the same way as the hydroxyl group, possibly the result of fewer available bonding sites due to dimerization of carboxyl groups between the molecules in solution, Additionally, molecules without aromatic rings did not appear to interact with the nanotubes. Of the molecules tested, salicylic acid behaved in a similar manner as αCHCA, with preferential nucleation on the CNTs, and a similar reduction in the resulting dried droplet spot size.

Additional research suggested that tubular image charge states [102] could be surrounding the nanotubes as a result of the metallic-dominated conduction behavior typically associated with multi-wall carbon nanotubes. The calculated potential for the image states indicated a possibility for the attraction of charged molecules at ranges greater than those typically associated with π bonds. This could be a dominant mechanism for the observed preferential nucleation.

The effectiveness of the carbon nanotube-enhanced substrate can be dependent on matrix concentration. For concentrations in the low and medium range, crystallization occurred primarily on the nanotubes. However, for concentrations approaching saturation of solution, the overabundance of material lead to deposition on the CNT's and the surrounding areas, and the average crystal size increased significantly.

The improved sample concentrating ability of the carbon nanotube-enhanced substrate over the standard MALDI plate was demonstrated by increased signal to noise ratios for all four peptides contained in the analyte mixture. The performance increase was thought

www.manaraa.com

to be the result of lateral matrix and analyte concentration on the sample surface due to preferential nucleation. Increased contact between the crystals could provide a path for pooling of excited states, thereby increasing efficiency of desorption and localized ionization.

For samples prepared with low concentrations of analyte, the carbon nanotube-enhanced substrate demonstrated better performance over the tested range than the standard MALDI plate, with signal to noise ratio increases from 2x to 5x. The detection limit for the MALDI plate in this configuration was also found. By comparison, the CNT-enhanced substrate produced a quality signal at the lowest concentration tested in this work (65 attomoles).

In this work, the crystal morphology was investigated using scanning electron microscopy. Optimal substrate performance corresponded to crystal morphology that was small and numerous instead of large and connected. This was believed to be the result of increased crystal surface area contributing to enhanced laser absorption and increased molecular desorption. Since the smaller crystals were not connected, direct exciton pooling could not contribute to the desorption process. The increase in analyte signal at this concentration could indicate that crystal surface area is a more dominant mechanism for desorption than exciton pooling. Additionally, since the average distance for probable exciton hopping was calculated to be seventeen molecular diameters (40), the optimal crystal size for maximum desorption should be thirty-four molecular diameters to ensure minimum surface area, maximum laser absorption, and the greatest probability for

www.manaraa.com

exciton pooling in the center of the matrix crystal from energy absorbed from all sides of the crystal.

The importance of optimized laser intensity for maximum signal to noise data was demonstrated by variation of the laser intensity with subsequent MALDI interrogations. This process also verified that the concentrating effect of the CNT-enhanced substrate reduced the required intensity for maximum SNR. This is thought to be the result of molecular localization, increased energy pooling, and the increased number of crystals interrogated simultaneously, compared to the samples deposited on the standard MALDI plate. Scanning electron microscopy was used to study crystal morphology, as images that were taken of the matrix crystals before and after the experiment displayed the effect of desorption at high laser intensities as the crystals appeared reduced in size and less numerous.

After extensive interrogation with a MALDI instrument, a sample can appear "depleted" when it no longer produces a detectable signal. It was shown experimentally that a depleted sample can still contain analyte in the crystal. Matrix crystals were deposited on both a CNT-enhanced substrate and a standard MALDI plate, and then interrogated to the point of apparent depletion. The crystals were fully dissolved in the same location by applying a droplet of solvent, then allowed to re-crystallize. This action released any analyte that was still contained in the crystal to be redistributed in the new crystal. The analyte signal returned after this cycle, but at a reduced level. This process

www.manaraa.com

was repeated many times for both types of substrates in order to compare performance for lateral concentration and signal regeneration.

It was demonstrated that samples deposited on the standard MALDI plate produced a signal for only two re-deposition cycles, while the samples on the CNT-enhanced substrates produced signal after three and four re-deposition cycles. Other parameters such as sample area of the dried droplet and threshold irradiance were recorded during the experiment. These two parameters indicated an almost linear relationship, as increased laser irradiance was required to achieve a detectable signal from samples with increased area, with each consecutive re-deposition cycle. Additionally, research published by Jaskolla (105) provided information regarding the rate of ablation for matrix crystals during the MALDI process, however the published rate was higher than the rate observed in this work for the given instrument conditions.

The development and commercialization of patterned carbon nanotube-enhanced substrates for MALDI could advance the detection of biomolecules at low concentrations, as was demonstrated in this work. An additional benefit would be an increase in throughput by reducing the amount of time necessary for sample interrogation at a single point due to lateral concentration and improved sample homogeneity. This technology has demonstrated capabilities in both of these areas that surpass the current method of single-step droplet deposition on a traditional, metal-based MALDI plate. Sample preparation time is reduced compared to that of the AnchorChip™ plate using sample-matrix wash, and under the right conditions, sample diameter is on the order of the laser

www.manaraa.com

diameter for total sample investigation. Typically, carbon nanotubes are very sensitive to abuse from mechanical sources, so delicate handling may be a concern. By contrast, traditional metal-based MALDI plates may be washed and polished. Additionally, the CNT enhanced substrate should be tested for re-use, as that may have an effect on widespread adoption of the technology. Even if only developed for use in specialized roles, carbon nanotubes have the potential to make a big impact in MALDI.

5.2 Future Work

Further investigation into matrix/analyte molecule interaction with carbon nanotubes (discussed in Section 4.1.1), should be performed to solidify a dominant mechanism. A number of techniques could be used for that purpose. Sample preparation via dried droplet deposition on Highly Oriented Pyrolytic Graphite (HOPG) could be used to study interactions with a highly ordered, pure carbon surface to simulate the sidewall of a carbon nanotube. A change in solvent composition (such as the ratio of Acetonitrile to water, or use of a different solvent from the same class) could be used to test the effect on matrix crystallization. Addition of OH group blockers, such as hexamethyldisilazane (HMDS), could prevent matrix dimerization, which may contribute to preferential nucleation on carbon nanotubes.

Raman spectroscopy could be used to verify chemical bonds between matrix/analyte molecules and carbon nanotubes dispersed in solution. The carbon nanotubes could be grown using the PE-CVD technique outlined in section 3.1.2, then removed from the

www.manaraa.com

surface and dispersed in a solution using ultrasonic and other techniques. Measurement of each individual solution under various conditions before combination should give further insight into the role that chemical factors (net charge, pH, concentration, etc.) have on the interaction process. Capturing real-time data during crystallization would also be of great interest.

Interactions due to hydrophobic/hydrophilic conditions could also be tested. The use of a contact angle goniometer could assist in further characterization of solution surface tension and can be used to correlate droplet behavior during the drying process with regard to changes in solution composition including Acetonitrile evaporation, increasing matrix concentration, and other factors.

Another interesting avenue of study would be to quantify the amount of analyte that is removed during a MALDI interrogation. Data from a layer-by-layer ablation of a single matrix crystal could be used to calculate a signal to noise ratio profile for the internal crystal structure and verify the ablation rate at constant laser intensity. When combined with a technique such as confocal microscopy, the location of different analytes could be mapped using photoluminescent tags specific to each analyte. Additional insight into the ablation process could be found by mapping analyte concentration and location after repeated cycles of analyte signal exhaustion followed by re-crystallization. Determining crystal size at the point of signal exhaustion could indicate the effective depth at which analytes can escape out of the crystal, leading to studies of analyte mobility while

www.manaraa.com

embedded in a matrix with regards to parameters such as composition, functionalization, and mass.

Recently published work has shown the capability of using vertically aligned arrays of carbon nanotubes for matrix-free laser desorption/ionization of small molecules (below 1000 Daltons) whose signal would be masked by signal from a traditional matrix molecule [114]. A similar experiment could be performed with the carbon nanotubes grown using the method shown in section 3.1.2. A direct comparison of analyte signal generated with matrix and without matrix would be possible. Additionally, the minimum-concentration detection limit for analyte deposited on CNT's without a matrix would be of interest.

Testing of additional analytes such as other peptide mixtures, proteins, and biological samples should also be performed to investigate the applicability of this technology for real-world applications.

www.manaraa.com

References

1. Kolch, W., H. Mischak, and A.R. Pitt, *The molecular make-up of a tumour: proteomics in cancer research.* Clinical Science, 2005. 108(5): p. 369-383.

2. Emmert-Buck, M.R., et al., *An approach to proteomic analysis of human tumors.* Molecular Carcinogenesis, 2000. 27(3): p. 158-165.

3. Srinivas, P.R., et al., *Proteomics for cancer biomarker discovery.* Clinical Chemistry, 2002. 48(8): p. 1160-1169.

4. Lage, H., *Proteomic approaches for investigation of therapy resistance in cancer.* Proteomics - Clinical Applications, 2009. 3(8): p. 883-911.

5. Voss, T., et al., *Correlation of clinical data with proteomics profiles in 24 patients with B-cell chronic lymphocytic leukemia.* International Journal of Cancer, 2001. 91(2): p. 180-186.

6. Zhang, B., et al., *Proteomics and Biomarkers for Ovarian Cancer Diagnosis.* Annals of Clinical & Laboratory Science, 2010. 40(3): p. 218-225.

7. Yim, E.K. and J.S. Park, *Role of proteomics in translational research in cervical cancer.* Expert Review of Proteomics, 2006. 3(1): p. 21-36.

8. Ahram, M., et al., *Proteomic analysis of human prostate cancer.* Molecular Carcinogenesis, 2002. 33(1): p. 9-15.

9. Dresselhaus, M.S., G. Dresselhaus, and R. Saito, *Carbon-Fibers Based on C-60 and Their Symmetry.* Physical Review B, 1992. 45(11): p. 6234-6242.

10. Dresselhaus, M.S., G. Dresselhaus, and R. Saito, *Physics of Carbon Nanotubes.* Carbon, 1995. 33(7): p. 883-891.

www.manaraa.com

11. Saito, R., et al., *Electronic-Structure of Chiral Graphene Tubules.* Applied Physics Letters, 1992. 60(18): p. 2204-2206.

12. Charlier, J.C. and J.P. Issi, *Electronic structure and quantum transport in carbon nanotubes.* Applied Physics a-Materials Science & Processing, 1998. 67(1): p. 79-87.

13. Journet, C., et al., *Large-scale production of single-walled carbon nanotubes by the electric-arc technique.* Nature, 1997. 388(6644): p. 756-758.

14. Bolshakov, A.P., et al., *A novel CW laser-powder method of carbon single-wall nanotubes production.* Diamond and Related Materials, 2002. 11(3-6): p. 927-930.

15. Li, W.Z., et al., *Large-scale synthesis of aligned carbon nanotubes.* Science, 1996. 274(5293): p. 1701-1703.

16. Bower, C., et al., *Plasma-induced alignment of carbon nanotubes.* Applied Physics Letters, 2000. 77(6): p. 830-832.

17. Han, J.H., et al., *Effects of growth parameters on the selective area growth of carbon nanotubes.* Thin Solid Films, 2002. 409(1): p. PII S0040-6090(02)00115-3.

18. Ren, Z.F., et al., *Synthesis of large arrays of well-aligned carbon nanotubes on glass.* Science, 1998. 282(5391): p. 1105-1107.

19. Derbyshire, F.J., A.E.B. Presland, and D.L. Trimm, *Graphite Formation by Dissolution-Precipitation of Carbon in Cobalt, Nickel and Iron.* Carbon, 1975. 13(2): p. 111-113.

20. Hooker, P., et al., *Preparation of Nickel Carbide Ultrafine Particles by Metal Vapor Methods.* Chemistry of Materials, 1991. 3(5): p. 947-952.

21. Baker, R.T.K., *Catalytic Growth of Carbon Filaments.* Carbon, 1989. 27(3): p. 315-323.

www.manaraa.com

22. Ducati, C., et al., *The role of the catalytic particle in the growth of carbon nanotubes by plasma enhanced chemical vapor deposition.* Journal of Applied Physics, 2004. 95(11): p. 6387-6391.

23. Sinnott, S.B., et al., *Model of carbon nanotube growth through chemical vapor deposition.* Chemical Physics Letters, 1999. 315(1-2): p. 25-30.

24. Ducati, C., et al., *Temperature selective growth of carbon nanotubes by chemical vapor deposition.* Journal of Applied Physics, 2002. 92(6): p. 3299-3303.

25. Chhowalla, M., et al., *Growth process conditions of vertically aligned carbon nanotubes using plasma enhanced chemical vapor deposition.* Journal of Applied Physics, 2001. 90(10): p. 5308-5317.

26. Qin, L.C., et al., *Growing carbon nanotubes by microwave plasma-enhanced chemical vapor deposition.* Applied Physics Letters, 1998. 72(26): p. 3437-3439.

27. Delzeit, L., et al., *Growth of multiwall carbon nanotubes in an inductively coupled plasma reactor.* Journal of Applied Physics, 2002. 91(9): p. 6027-6033.

28. Schouten, F.C., O.L.J. Gijzeman, and G.A. Bootsma, *Interaction of Methane with Ni(111) and Ni(100) - Diffusion of Carbon into Nickel through the (100) Surface - Aes-Leed Study.* Surface Science, 1979. 87(1): p. 1-12.

29. Nishitani, S.R., et al., *Metastable Solid Solubility Limit of Carbon in the Ni-C System.* Journal of Materials Science Letters, 1985. 4(7): p. 872-875.

30. Holstein, W.L., *The Roles of Ordinary and Soret Diffusion in the Metal-Catalyzed Formation of Filamentous Carbon.* Journal of Catalysis, 1995. 152(1): p. 42-51.

31. Merkulov, V.I., et al., *Alignment mechanism of carbon nanofibers produced by plasma-enhanced chemical-vapor deposition.* Applied Physics Letters, 2001. 79(18): p. 2970-2972.

32. Kovacs, G., *Micromachined Transducers Sourcebook*. 1998: McGraw-Hill. 911.

33. Chapman, B., *Glow Discharge Processes*. 1980: John Wiley & Sons. 406.

www.manaraa.com

34. Karas, M., D. Bachmann, and F. Hillenkamp, *Influence of the Wavelength in High-Irradiance Ultraviolet-Laser Desorption Mass-Spectrometry of Organic-Molecules.* Analytical Chemistry, 1985. 57(14): p. 2935-2939.

35. Koichi Tanaka, H.W., Yutaka Ido, Satoshi Akita, Yoshikazu Yoshida, Tamio Yoshida, T. Matsuo,, *Protein and polymer analyses up to m/z 100,000 by laser ionization time-of-flight mass spectrometry.* Rapid Communications in Mass Spectrometry, 1988. 2(8): p. 151-153.

36. *massspec_schem_maldi.gif*, Klaas Jan van Wijk [online] Available at: <http://cbsu.tc.cornell.edu/vanwijk/images/massspec/massspec_schem_maldi.gif> [Accessed 01 March 2010]

37. Puretzky, A.A., et al., *Imaging of vapor plumes produced by matrix assisted laser desorption: A plume sharpening effect.* Physical Review Letters, 1999. 83(2): p. 444-447.

38. Knochenmuss, R., *A quantitative model of ultraviolet matrix-assisted laser desorption/ionization.* Journal of Mass Spectrometry, 2002. 37(8): p. 867-877.

39. Ehring, H., M. Karas, and F. Hillenkamp, *Role of Photoionization and Photochemistry in Ionization Processes of Organic-Molecules and Relevance for Matrix-Assisted Laser Desorption Ionization Mass-Spectrometry.* Organic Mass Spectrometry, 1992. 27(4): p. 472-480.

40. Knochenmuss, R., et al., *The matrix suppression effect and ionization mechanisms in matrix-assisted laser desorption/ionization.* Rapid Communications in Mass Spectrometry, 1996. 10(8): p. 871-877.

41. Zenobi, R. and R. Knochenmuss, *Ion formation in MALDI mass spectrometry.* Mass Spectrometry Reviews, 1998. 17(5): p. 337-366.

42. Karbach, V. and R. Knochenmuss, *Do single matrix molecules generate primary ions in ultraviolet matrix-assisted laser desorption/ionization.* Rapid Communications in Mass Spectrometry, 1998. 12(14): p. 968-974.

43. Lin, Q. and R. Knochenmuss, *Two-photon ionization thresholds of matrix-assisted laser desorption/ionization matrix clusters.* Rapid Communications in Mass Spectrometry, 2001. 15(16): p. 1422-1426.

www.manaraa.com

44. Dreisewerd, K., et al., *Influence of the Laser Intensity and Spot Size on the Desorption of Molecules and Ions in Matrix-Assisted Laser-Desorption Ionization with a Uniform Beam Profile.* International Journal of Mass Spectrometry, 1995. 141(2): p. 127-148.

45. Mowry, C.D. and M.V. Johnston, *Internal Energy of Neutral Molecules Ejected by Matrix-Assisted Laser-Desorption.* Journal of Physical Chemistry, 1994. 98(7): p. 1904-1909.

46. Gluckmann, M. and M. Karas, *Special feature: Perspective - The initial ion velocity and its dependence on matrix, analyte and preparation method in ultraviolet matrix-assisted laser desorption ionization.* Journal of Mass Spectrometry, 1999. 34(5): p. 467-477.

47. Bokelmann, V., B. Spengler, and R. Kaufmann, *Dynamical Parameters of Ion Ejection and Ion Formation in Matrix-Assisted Laser Desorption/Ionization.* European Mass Spectrometry, 1995. 1(1): p. 81-93.

48. Setz, P.D. and R. Knochenmuss, *Exciton mobility and trapping in a MALDI matrix.* Journal of Physical Chemistry A, 2005. 109(18): p. 4030-4037.

49. Jaskolla, T.W. and M. Karas, *Using fluorescence dyes as a tool for analyzing the MALDI process.* Journal of the American Society for Mass Spectrometry, 2008. 19(8): p. 1054-1061.

50. Little, D.P., et al., *MALDI on a chip: Analysis of arrays of low femtomole to subfemtomole quantities of synthetic oligonucleotides and DNA diagnostic products dispensed by a piezoelectric pipet.* Analytical Chemistry, 1997. 69(22): p. 4540-4546.

51. Ingendoh, A., et al., *Factors Affecting the Resolution in Matrix-Assisted Laser-Desorption Ionization Mass-Spectrometry.* International Journal of Mass Spectrometry and Ion Processes, 1994. 131: p. 345-354.

52. Beavis, R.C. and J.N. Bridson, *Epitaxial Protein Inclusion in Sinapic Acid Crystals.* Journal of Physics D-Applied Physics, 1993. 26(3): p. 442-447.

53. Beavis, R.C., T. Chaudhary, and B.T. Chait, *Alpha-Cyano-4-Hydroxycinnamic Acid as a Matrix for Matrix-Assisted Laser Desorption Mass-Spectrometry.* Organic Mass Spectrometry, 1992. 27(2): p. 156-158.

www.manaraa.com

54. Strupat, K., M. Karas, and F. Hillenkamp, *2,5-Dihydroxybenzoic Acid - a New Matrix for Laser Desorption Ionization Mass-Spectrometry.* International Journal of Mass Spectrometry and Ion Processes, 1991. 111: p. 89-102.

55. Dai, Y.Q., R.M. Whittal, and L. Li, *Two-layer sample preparation: A method for MALDI-MS analysis of complex peptide and protein mixtures.* Analytical Chemistry, 1999. 71(5): p. 1087-1091.

56. Beeson, M.D., K.K. Murray, and D.H. Russell, *Aerosol Matrix-Assisted Laser-Desorption Ionization - Effects of Analyte Concentration and Matrix-to-Analyte Ratio.* Analytical Chemistry, 1995. 67(13): p. 1981-1986.

57. Vorm, O., P. Roepstorff, and M. Mann, *Improved Resolution and Very High-Sensitivity in Maldi Tof of Matrix Surfaces Made by Fast Evaporation.* Analytical Chemistry, 1994. 66(19): p. 3281-3287.

58. Taylor, G., *Disintegration of Water Drops in Electric Field.* Proceedings of the Royal Society of London Series a-Mathematical and Physical Sciences, 1964. 280(138): p. 383-&.

59. Rayleigh, L., *On the Equilibrium of Liquid Conducting Masses charged with Electricity.* Philosophical Magazine, 1882. 14: p. 184-186.

60. Zeleny, J., *The electrical discharge from liquid points, and a hydrostatic method of measuring the electric intensity at their surfaces.* Physical Review, 1914. 3(2): p. 69.

61. Zeleny, J., *Instability of electrified liquid surfaces.* Physical Review, 1917. 10(1): p. 1-6.

62. Cech, N.B. and C.G. Enke, *Practical implications of some recent studies in electrospray ionization fundamentals.* Mass Spectrometry Reviews, 2001. 20(6): p. 362-387.

63. Stark, A., *Advancement And Optimization Of An Electrospray Injection Based In-Vacuum Patterning System For Macro-Molecular Materials*, in *Electrical Engineering*. 2008, University of South Florida: Tampa.

www.manaraa.com

64. Cascio, A.J., et al., *Investigation of a polythiophene interface using photoemission spectroscopy in combination with electrospray thin-film deposition.* Applied Physics Letters, 2006. 88(6).

65. Magulick, J., M.M. Beerbom, and R. Schlaf, *Comparison of ribonucleic acid homopolymer ionization energies and charge injection barriers.* Journal of Physical Chemistry B, 2006. 110(32): p. 15973-15981.

66. Yi, Y., et al., *Orbital alignment at poly 2-methoxy-5-(2(')-ethylhexyloxy)-p-phenylene vinylene interfaces.* Journal of Applied Physics, 2007. 102(2).

67. Magulick, J., M.M. Beerbom, and R. Schlaf, *Investigation of adenine, uracil, and ribose phosphate thin films prepared by electrospray in vacuum deposition using photoemission spectroscopy.* Thin Solid Films, 2008. 516(9): p. 2396-2400.

68. Magulick, J., M.M. Beerbom, and R. Schlaf, *Polarization lowering of charge injection barriers at a ribonucleic acid/Au interface.* Journal of Applied Physics, 2008. 104(12).

69. Fenn, J.B., et al., *Electrospray Ionization for Mass-Spectrometry of Large Biomolecules.* Science, 1989. 246(4926): p. 64-71.

70. Axelsson, J., et al., *Improved reproducibility and increased signal intensity in matrix-assisted laser desorption/ionization as a result of electrospray sample preparation.* Rapid Communications in Mass Spectrometry, 1997. 11(2): p. 209-213.

71. Hanton, S.D., et al., *Investigations of electrospray sample deposition for polymer MALDI mass spectrometry.* Journal of the American Society for Mass Spectrometry, 2004. 15(2): p. 168-179.

72. Schuerenberg, M., et al., *Prestructured MALDI-MS sample supports.* Analytical Chemistry, 2000. 72(15): p. 3436-3442.

73. Shaler, T.A., et al., *Analysis of Enzymatic DNA-Sequencing Reactions by Matrix-Assisted Laser-Desorption Ionization Time-of-Flight Mass-Spectrometry.* Rapid Communications in Mass Spectrometry, 1995. 9(10): p. 942-947.

www.manaraa.com

74. Roskey, M.T., et al., *DNA sequencing by delayed extraction matrix-assisted laser desorption/ionization time of flight mass spectrometry.* Proceedings of the National Academy of Sciences of the United States of America, 1996. 93(10): p. 4724-4729.

75. Little, D.P., et al., *Sequence information from 42-108-mer DNAs (complete for a 50-mer) by tandem mass spectrometry.* Journal of the American Chemical Society, 1996. 118(39): p. 9352-9359.

76. Crewe, A., D. Eggenberger, and J. Wall, *Electron Gun using a Field Emission Source.* Review of Scientific Instruments, 1968. 39(4): p. 576.

77. *Hitachi Scanning Electron Microscope NREC User's Manual*, Bieber, J. [online] Available at: <http://nnrc.eng.usf.edu/manuals/users/Metrology%20Lab%20(NTA%20105)/S800%20SEM> [Accessed 28 September 2009]

78. Goldstein, J. and H. Yakowitz, *Practical scanning electron microscopy, electron and ion microprobe analysis*. 1975, New York: Plenum Press.

79. McNaught, A. and A. Wilkinson, *Compendium of Chemical Terminology*. 2nd edition ed. 1997, Oxford: Blackwell Scientific Publications.

80. Goldstein, G., et al., *Scanning electron microscopy and x-ray microanalysis*. 1981, Ney York: Plenum Press.

81. Wetzig, K. and D. Schulze, *In situ Scanning Electron Microscopy in Materials Research*. 1995, Berlin: Akademie Verlag.

82. Reimer, L., *Scanning Electron Microscopy: Physics of Image Formation and Microanalysis*. 2nd ed. 1998, Berlin: Springer-Verlag. 527.

83. Everhart, T. and R. Thornley, *Wide-band detector for micro-microampere low-energy electron currents.* Journal of Scientific Instruments, 1960. 37(7): p. 246-248.

84. Schumacher, J., *Design and Construction of Plasma Enhanced Chemical Vapor Deposition Reactor and Directed Assembly of Carbon Nanotubes*, in *Electrical Engineering*. 2003, University of South Florida: Tampa, FL. p. 73.

www.manaraa.com

85. O'Hanlon, J., *A User's Guide to Vacuum Technology*. 3rd ed. 2003, New York, NY: Wiley-Interscience. 536.

86. Smalyukh, II, et al., *Structure and dynamics of liquid crystalline pattern formation in drying droplets of DNA.* Physical Review Letters, 2006. 96(17).

87. Bhardwaj, R., X.H. Fang, and D. Attinger, *Pattern formation during the evaporation of a colloidal nanoliter drop: a numerical and experimental study.* New Journal of Physics, 2009. 11.

88. Dufresne, E.R., et al., *Flow and fracture in drying nanoparticle suspensions.* Physical Review Letters, 2003. 91(22).

89. Deegan, R.D., et al., *Capillary flow as the cause of ring stains from dried liquid drops.* Nature, 1997. 389(6653): p. 827-829.

90. Sedgewick, J., *Scientific Imaging with Photoshop: Methods, Measurement, and Output*. 2008, Berkeley, CA: New Riders Press. 312.

91. *AnchorChip Technology Revision 2.3*, Bruker Daltonics [online] Available at: <http://personal.rhul.ac.uk/upba/211/Anchorchip-manual_2_3.pdf> [Accessed August 2005]

92. Chen, R.J., et al., *Noncovalent sidewall functionalization of single-walled carbon nanotubes for protein immobilization.* Journal of the American Chemical Society, 2001. 123(16): p. 3838-3839.

93. Star, A., et al., *Preparation and properties of polymer-wrapped single-walled carbon nanotubes.* Angewandte Chemie-International Edition, 2001. 40(9): p. 1721-1725.

94. Zheng, M., et al., *DNA-assisted dispersion and separation of carbon nanotubes.* Nature Materials, 2003. 2(5): p. 338-342.

95. Zorbas, V., et al., *Importance of aromatic content for peptide/single-walled carbon nanotube interactions.* Journal of the American Chemical Society, 2005. 127(35): p. 12323-12328.

www.manaraa.com

96. Piao, L.Y., et al., *Adsorption of L-phenylalanine on single-walled carbon nanotubes.* Journal of Physical Chemistry C, 2008. 112(8): p. 2857-2863.

97. Salzmann, C.G., et al., *Interaction of tyrosine-, tryptophan-, and lysine-containing polypeptides with single-wall carbon nanotubes and its relevance for the rational design of dispersing agents.* Journal of Physical Chemistry C, 2007. 111(50): p. 18520-18524.

98. Tomasio, S.D. and T.R. Walsh, *Atomistic modelling of the interaction between peptides and carbon nanotubes.* Molecular Physics, 2007. 105(2-3): p. 221-229.

99. Zheng, L.F., D. Jain, and P. Burke, *Nanotube-Peptide Interactions on a Silicon Chip.* Journal of Physical Chemistry C, 2009. 113(10): p. 3978-3985.

100. Nepal, D. and K.E. Geckeler, *Proteins and carbon nanotubes: Close encounter in water.* Small, 2007. 3(7): p. 1259-1265.

101. Nakamura, N. and T. Sato, *1,10-Decanediol.* Acta Crystallographica Section C, 1999. 55: p. 1685-1687.

102. Granger, B.E., et al., *Highly extended image states around nanotubes.* Physical Review Letters, 2002. 89(13).

103. Hoyer, T., W. Tuszynski, and C. Lienau, *Ultrafast photodimerization dynamics in alpha-cyano-4-hydroxycinnamic and sinapinic acid crystals.* Chemical Physics Letters, 2007. 443(1-3): p. 107-112.

104. Hathout, Y., et al., *Cross-linking of human placenta pi class glutathione S-transferase dimer by chlorambucil.* Chemical Research in Toxicology, 1996. 9(6): p. 1044-1049.

105. *ArgusLab Molecular Modeling and Drug Docking Software*, Mark A. Thompson [online] Available at: <http://www.arguslab.com/> [Accessed 14 October 2009]

106. Zar, J.H., *Biostatistical analysis*. 4th ed. 1999, Upper Saddle River, NJ: Prentice Hall. 929.

www.manaraa.com

107. Sokal, R.R. and F.J. Rohlf, *Biometry: The principles and practice of statistics in biological research*. 3rd ed. 1995, New York: W.H. Freeman and Co. 887.

108. Piao, L.Y., et al., *The Adsorption of L-Phenylalanine on Oxidized Single-Walled Carbon Nanotubes.* Journal of Nanoscience and Nanotechnology, 2009. 9(2): p. 1394-1399.

109. Li, X.J., et al., *Direct measurements of interactions between polypeptides and carbon nanotubes.* Journal of Physical Chemistry B, 2006. 110(25): p. 12621-12625.

110. Wang, S.Q., et al., *Peptides with selective affinity for carbon nanotubes.* Nature Materials, 2003. 2(3): p. 196-200.

111. Zhang, X.M., et al., *An improved method of sample preparation on AnchorChip (TM) targets for MALDI-MS and MS/MS and its application in the liver proteome project.* Proteomics, 2007. 7(14): p. 2340-2349.

112. Jaskolla, T.W., et al., *Comparison Between Vacuum Sublimed Matrices and Conventional Dried Droplet Preparation in MALDI-TOF Mass Spectrometry.* Journal of the American Society for Mass Spectrometry, 2009. 20(6): p. 1104-1114.

113. Horneffer, V., et al., *Localization of analyte molecules in MALDI preparations by confocal laser scanning microscopy.* Analytical Chemistry, 2001. 73(5): p. 1016-1022.

114. Shin, S.J., et al., *Matrix-free laser desorption/ionization on vertically aligned carbon nanotube arrays.* Bull. Korean Chem. Soc., 2006. 27(4): p. 581-583.

115. *Peptides - Bradykinins*, AnaSpec, Inc. [online] Available at: <http://www.anaspec.com/products/productcategory.asp?id=156> [Accessed 04 February 2010]

116. *Peptides - Angiotensins and Related Peptides*, AnaSpec, Inc. [online] Available at: <http://www.anaspec.com/products/productcategory.asp?id=152> [Accessed 04 February 2010]

www.manaraa.com

117. *Peptides - Fibrinogen and Related Peptides*, AnaSpec, Inc. [online] Available at: <http://www.anaspec.com/products/productcategory.asp?id=444> [Accessed 04 February 2010]

118. *Peptides - ACTH and Related Peptides*, AnaSpec, Inc. [online] Available at: <http://www.anaspec.com/products/productcategory.asp?id=446> [Accessed 04 February 2010]

119. *EMBL WWW Gateway to Isoelectric Point Service*, EMBL Heidelberg - European Molecular Biology Laboratory [online] Available at: <http://www3.embl.de/cgi/pi-wrapper.pl> [Accessed 06 September 2010]

120. Lehninger, A.L., *Biochimie*. 1979, New York: Worth Publishers.

www.manaraa.com

Glossary

Mean free path – the average distance a particle can travel between subsequent collisions with other particles. The path length is dependent on pressure, temperature, and particle diameter [33].

Morphology – the form and structure of an object, typically a film or particle.

Profilometer – an instrument that uses a stylus to measure the profile of a surface. The vertical resolution of the instrument is typically in the nanometer range.

Supersaturation – a solution that contains a dissolved amount of material greater than the standard maximum under normal circumstances. Supersaturation can occur when an initial condition of a solution is changed such as a reduction in temperature or change in solvent composition due to evaporation.

Torr – a unit of pressure equal to $1/760^{th}$ of a standard atmosphere or approximately 1mm of mercury in a mercury barometer.

www.manaraa.com

Appendices

www.manaraa.com

Appendix A

Bradykinin – A family of peptides which can act to dilate blood vessels in the body, thereby lowering blood pressure. Bradykinin can also be released by the body in response to asthma attacks. Additionally, it can act as a neurotransmitter, nitric acid-forming stimulator, and thermo-regulator by dilating blood vessels near the surface of the skin to enhance heat dissipation [115].

Angiotensin – A peptide that acts to constrict blood vessels in the body, resulting in increased blood pressure. Angiotensin can also stimulate the release of aldosterone from the adrenal glands [116].

Fibrinogen – A protein made in the liver which can be converted into fibrin and plays an important role in blood coagulation. Fibrinogen can affect the viscosity of blood plasma and has been linked to various cardiovascular diseases including stroke and coronary artery disease [117].

Adrenocorticotropic hormone (ACTH) – A peptide hormone that is produced in response to stress, which can increase production of steroid hormones such as hydrocortisone from the adrenal cortex [118].

www.manaraa.com

Appendix B

Molecular models of the peptides in Mixture 1 used in this research illustrate the location of the amino acid groups containing carbon rings (indicated with arrows), for possible interactions with carbon nanotubes. The models were created using ArgusLab 4.0.1 Molecular Modeling and Drug Docking software [105].

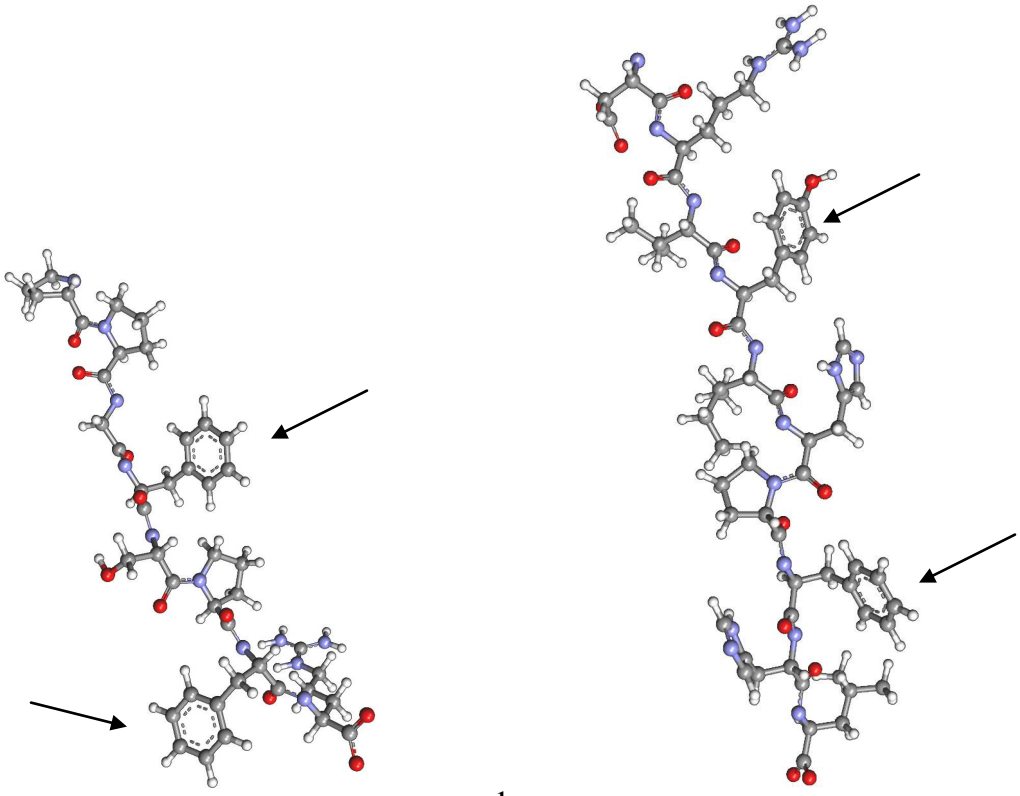

Figure 90. Molecular models of des-Arginine[1]-Bradykinin (left) and Angiotensin I (right).

www.manaraa.com

Appendix B: (continued)

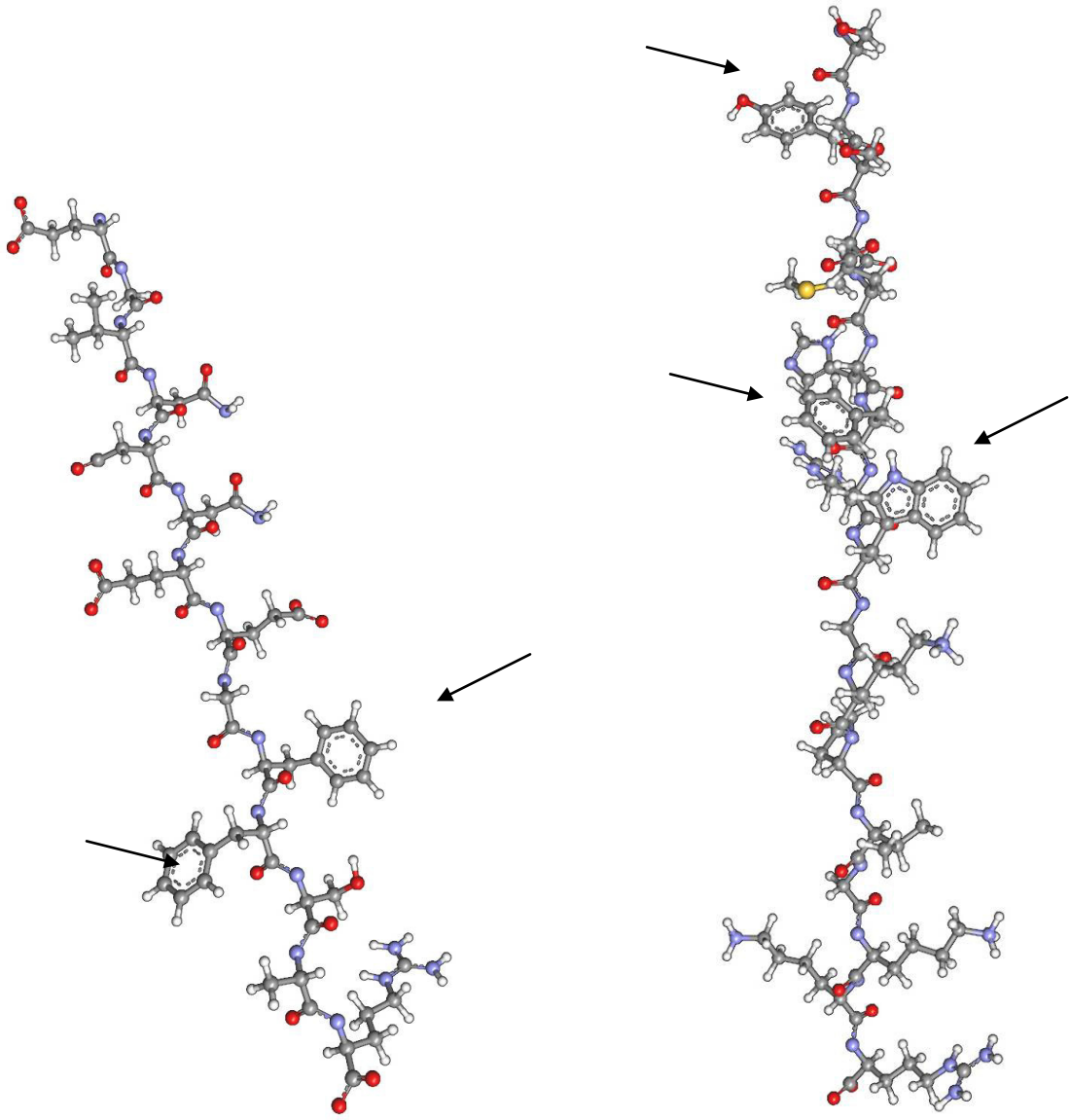

Figure 91. Molecular models of Glu[1]-Fibrinopeptide B (left) and ACTH (right).

www.manaraa.com

Appendix C

The Isoelectric Point (pI) is the pH value at which no net electrical charge exists on a molecule. Table 8 lists pI values for each of the peptides found in peptide Mixture I used in this research. The values were calculated via the Isoelectric Point Service online tool [119] using the technique published by Lehninger's 1979 work *Biochimie* [120]. The range of net charge is given for the pH value of 2.75, which corresponds to the measured value of the αCHCA matrix solution (section 4.1.1), also calculated using the same online tool.

Table 8. Isoelectric points for individual components of peptide Mixture 1.

Analyte Component	Isoelectric Point (pI)	Net Charge at pH 2.75
des-Arginine^{1}-Bradykinin	11.045	+1.18 to +1.41
Angiotensin I	7.909	+3.05 to +3.36
Glu^{1}-Fibrinopeptide B	3.685	+0.89 to +1.31
Adrenocorticotropic hormone (ACTH)	10.88	+6.12 to +6.39

Table 9. Acid dissociation constants for matrix and analog molecules.

Molecule	pKa Value
αCHCA	1.17
Catechol	9.173-9.48
Benzoic acid	4.20
Salicylic acid	2.97
Decanediol	Alcohol, pKa value unknown

www.manaraa.com

Appendix D

The following images are histograms of crystallite sizes for the wide range of matrix depositions (concentrations 0.006 mg/mL to 6 mg/mL) from section 4.1.2. The data was calculated using ImageJ software in particle analysis mode.

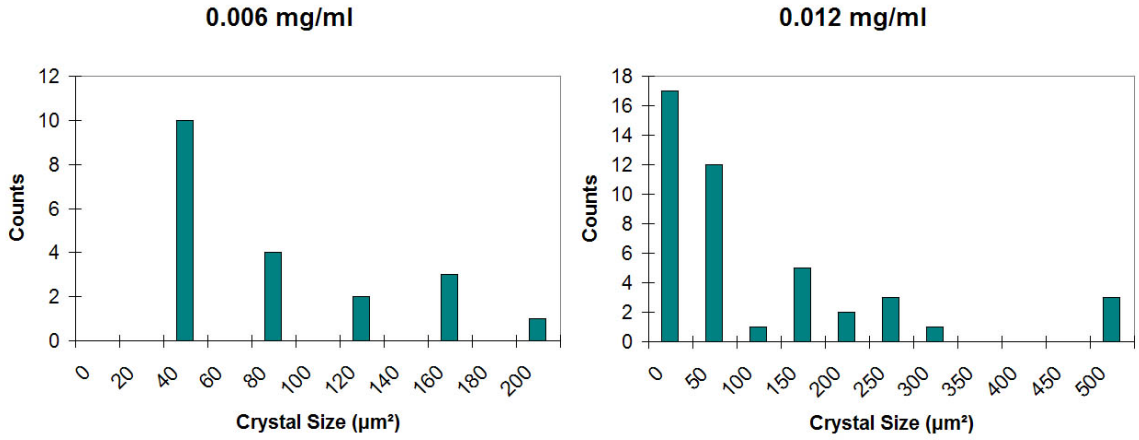

Figure 92. Distribution of crystal sizes for matrix concentration 0.006 mg/mL (left) and 0.012 mg/mL (right).

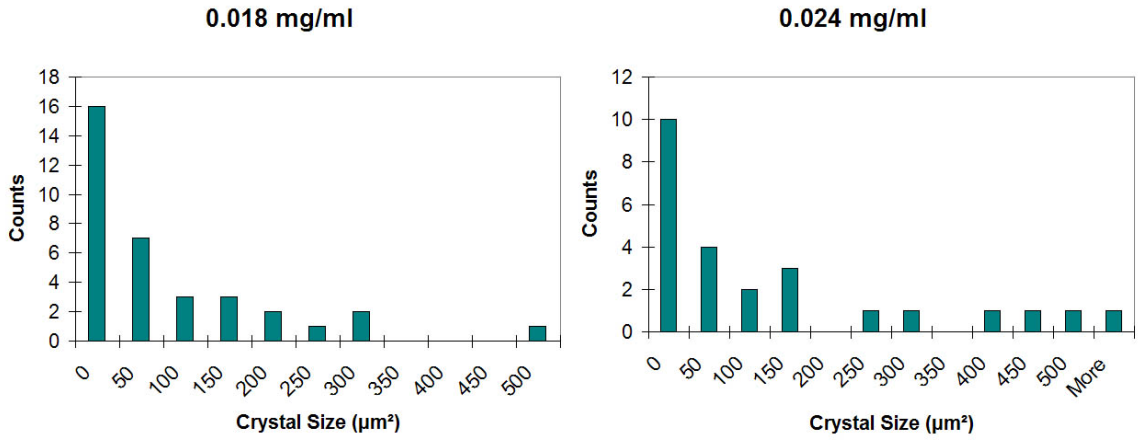

Figure 93. Distribution of crystal sizes for matrix concentration 0.018 mg/mL (left) and 0.024 mg/mL (right). The majority of crystals have an area of less than 200 µm^2.

www.manaraa.com

Appendix D: (continued)

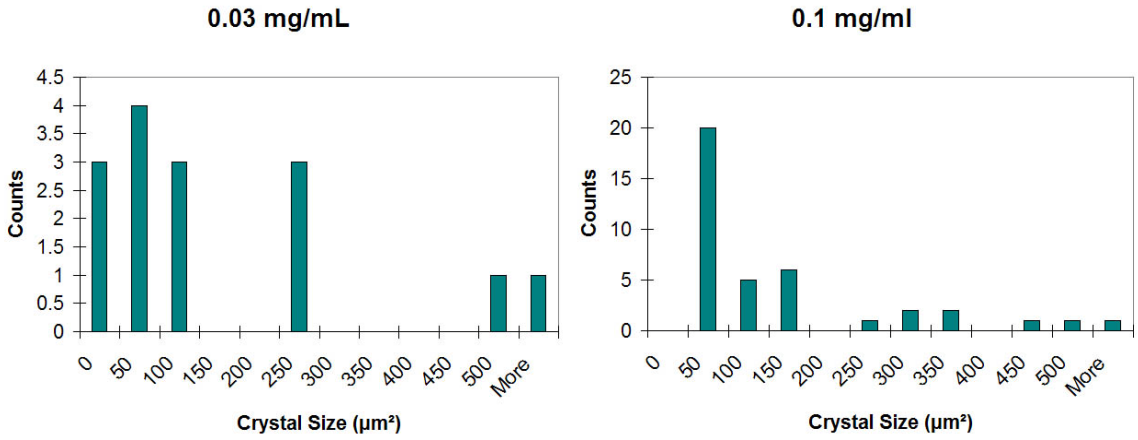

Figure 94. Distribution of crystal sizes for matrix concentration 0.03 mg/mL (left) and 0.1 mg/mL (right).

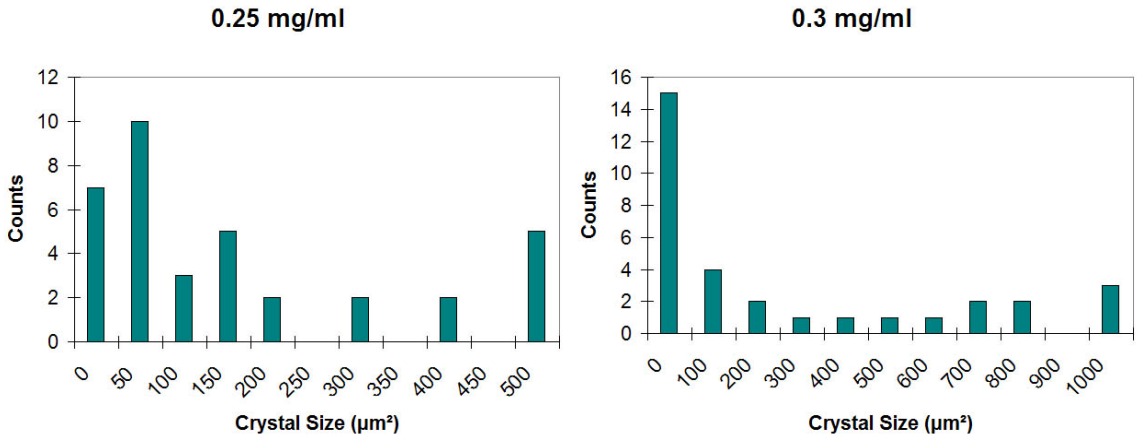

Figure 95. Distribution of crystal sizes for matrix concentration 0.25 mg/mL (left) and 0.3 mg/mL (right). The crystals larger than 500 µm^2 are possibly clusters of smaller crystals that could not be resolved due to overlap.

www.manaraa.com

Appendix D: (continued)

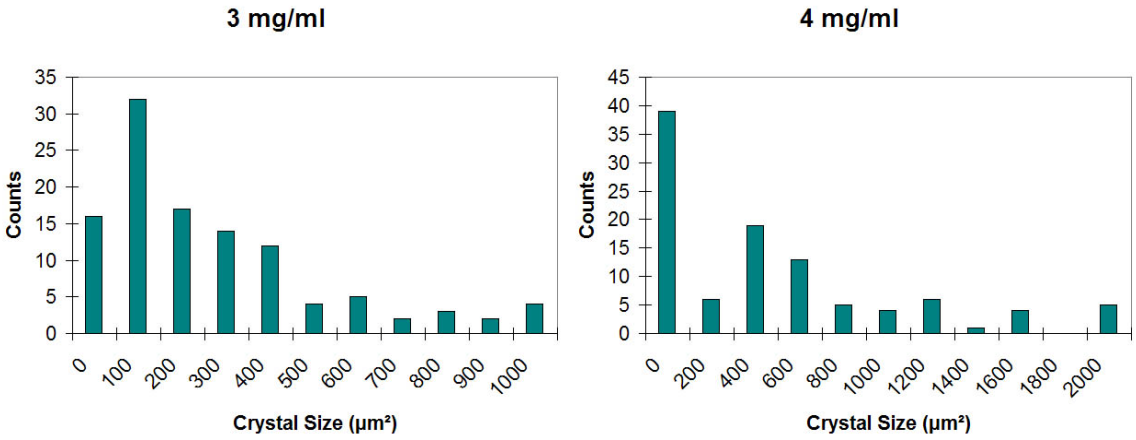

Figure 96. Distribution of crystal sizes for matrix concentration 3 mg/mL (left) and 4 mg/mL (right).

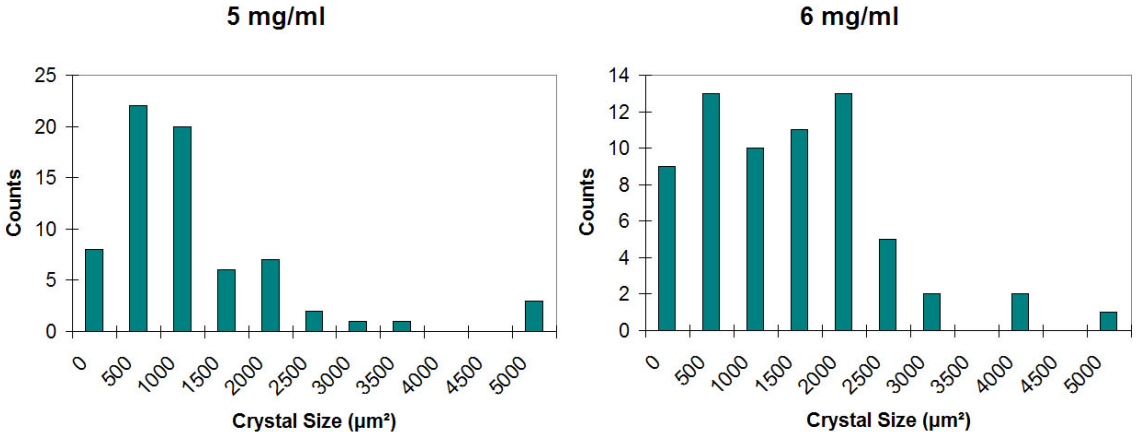

Figure 97. Distribution of crystal sizes for matrix concentration 5 mg/mL (left) and 6 mg/mL (right). A significant number of crystals have areas up to 2500 µm^2, which appear to be single crystals, rather than clusters of smaller ones.

www.manaraa.com

Appendix E

Images of αCHCA matrix crystals on carbon nanotubes taken using scanning electron microscopy (Section 2.4) before and after MALDI investigation indicate an interesting effect that could be studied further in the future. It appears that the MALDI process removes material from the sharp edges and corners of crystallites preferentially, possibly due to increased molecular flux from the desorption process as a result of fewer neighboring molecules, localized accumulation of ions or charged molecules during laser absorption, or perhaps the presence of an induced electric field with concentrated equipotentials at the crystal edges.

Additionally, the increased emission of secondary electrons due to edge effects illustrated in Figure 35 highlight the areas of the matrix crystals that are removed or rounded during the process of MALDI interrogation. This effect may prove useful for visual determination of crystal morphology and should be studied further to compare the energy absorbed by the matrix crystals from both electron beam and MALDI-based laser illumination sources to ascertain if any correlation can be determined with respect to localized emission.

www.manaraa.com

Appendix E: (continued)

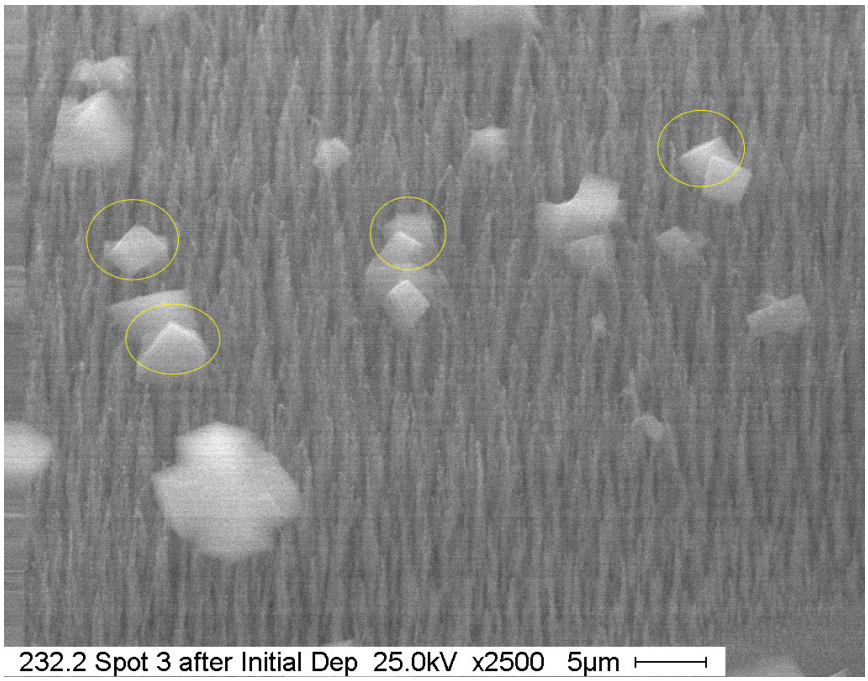

Figure 98. SEM image of matrix/analyte crystals on patterned area of CNT's directly after deposition. The sharp edges of the crystals are circled in green.

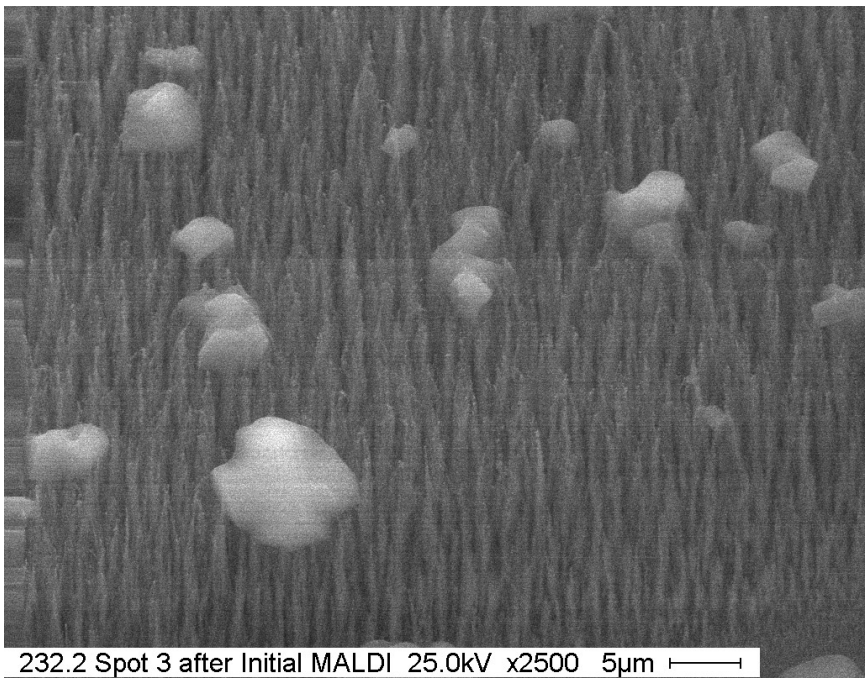

Figure 99. SEM image of same area after MALDI interrogation. The sharp edges that were visible in the previous figure are rounded and appear to be melted.

www.manaraa.com

Appendix E: (continued)

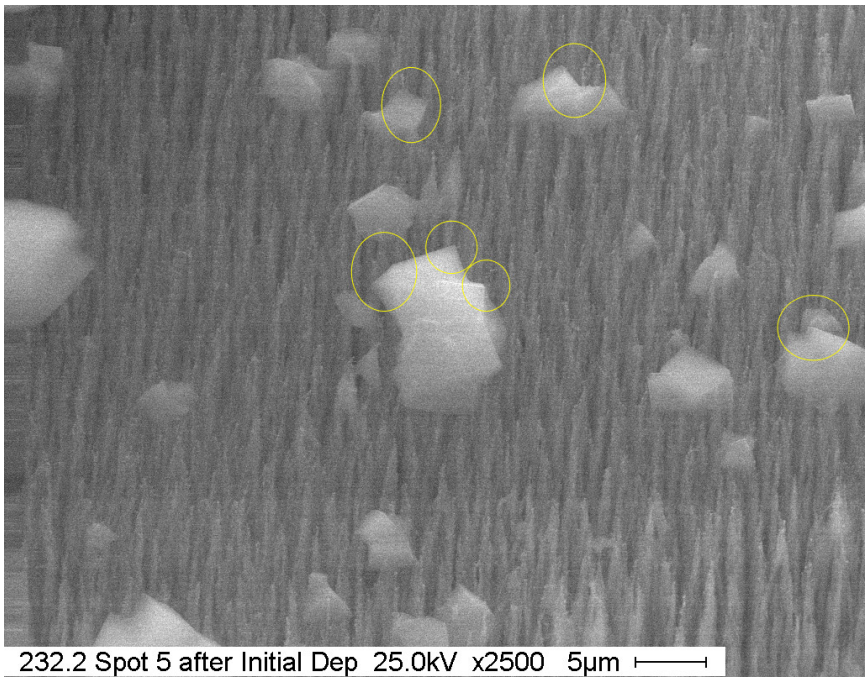

Figure 100. Additional sample imaged directly after matrix deposition.

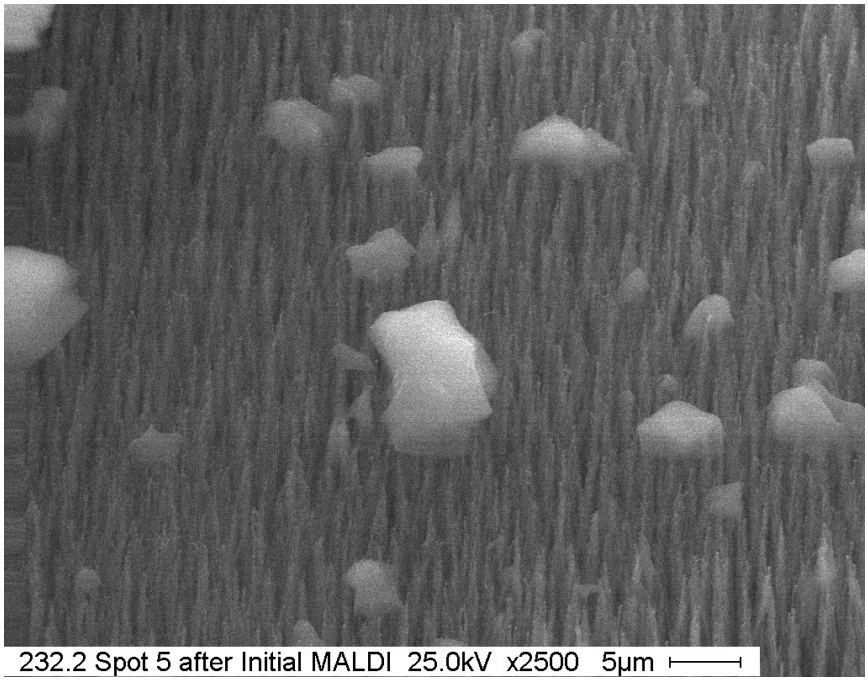

Figure 101. Same sample after removal from the MALDI instrument. All corners previously visible are no longer present.

www.manaraa.com

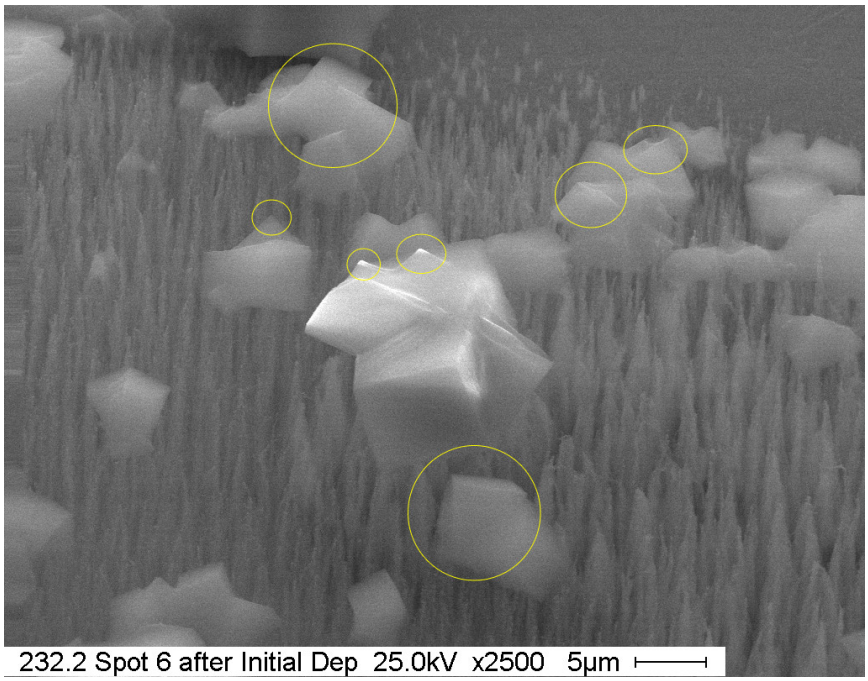

Figure 102. Sample illustrating increased secondary electron emission from corners of the crystallites (bright points).

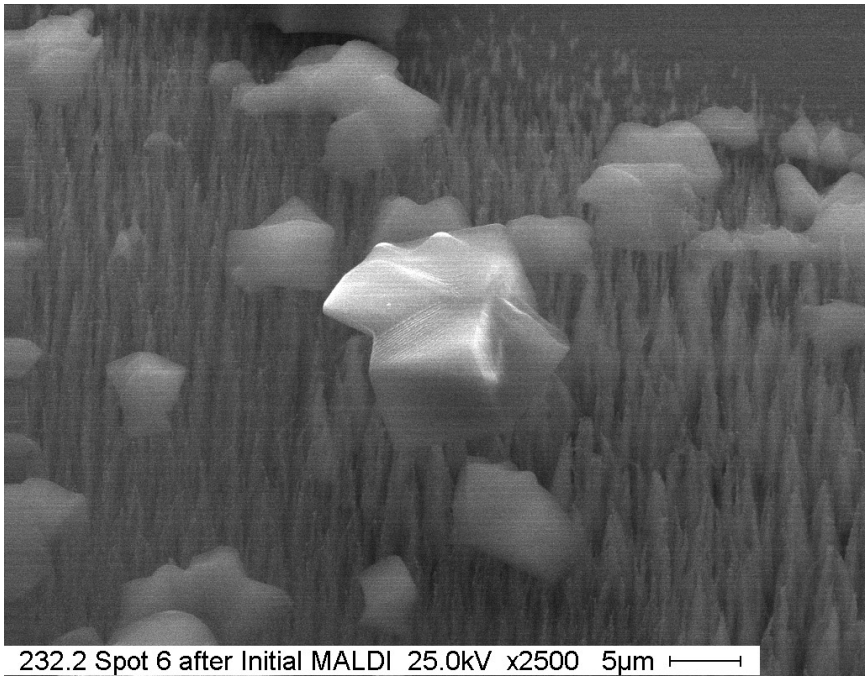

Figure 103. After MALDI, corners are rounded, but with less degradation. Bright areas still visible on large matrix crystal.

www.manaraa.com

About the Author

Joshua Schumacher received both Bachelor and Master of Science degrees in Electrical Engineering from the University of South Florida in 2003. He became a National Science Foundation Fellow through the Integrative Graduate Education and Research Traineeship (IGERT) program and entered the Ph.D. program at the University of South Florida in 2004.

While in the Ph.D. program, Mr. Schumacher completed an internship at the Moffitt Cancer Center in Tampa, Florida. He was awarded a USF Presidential Doctoral Fellowship in 2007. Mr. Schumacher has given presentations at numerous national and international conferences as well as middle and high schools and helped develop the Research Experience for High School students program at USF.

Mr. Schumacher is a member of the Institute of Electrical and Electronics Engineers, the National Society of Collegiate Scholars, and Eta Kappa Nu, the electrical engineering honor society.

www.manaraa.com